Mg2Si, Mg2(Si,Sn) and diffusion barriers deposited as thin films by microwave plasma-assisted co-sputtering for automotive thermoelectric applications

Codrin Prahoveanu

▶ **To cite this version:**

Codrin Prahoveanu. Mg2Si, Mg2(Si,Sn) and diffusion barriers deposited as thin films by microwave plasma-assisted co-sputtering for automotive thermoelectric applications. Materials. Université Grenoble Alpes, 2015. English. NNT : 2015GREAI091 . tel-02001974

HAL Id: tel-02001974
https://hal.science/tel-02001974v1

Submitted on 31 Jan 2019

HAL is a multi-disciplinary open access archive for the deposit and dissemination of scientific research documents, whether they are published or not. The documents may come from teaching and research institutions in France or abroad, or from public or private research centers.

L'archive ouverte pluridisciplinaire **HAL**, est destinée au dépôt et à la diffusion de documents scientifiques de niveau recherche, publiés ou non, émanant des établissements d'enseignement et de recherche français ou étrangers, des laboratoires publics ou privés.

UNIVERSITÉ GRENOBLE ALPES

THÈSE

Pour obtenir le grade de

DOCTEUR DE L'UNIVERSITÉ GRENOBLE ALPES

Spécialité : **Mécanique de fluides, Procédés, Energétique**

Arrêté ministériel : 7 août 2006

Présentée par

Codrin PRAHOVEANU

Thèse dirigée par **Stéphane BECHU**
codirigée par **Ana LACOSTE**
co-encadrée par **Laetitia LAVERSENNE**
et suivie par **Cédric de VAULX**, encadrant industriel

préparée au sein du **Laboratoire de Physique Subatomique et de Cosmologie de Grenoble et de l'Institut Néel**
dans **l'École Doctorale I-MEP2, Ingénierie – Matériaux, Mécanique, Energétique, Environnement, Procédé, Production**

Mg_2Si, $Mg_2(Si,Sn)$ et barrières de diffusion déposées en couches minces par co-pulvérisation assistée par plasma micro-onde pour des applications thermoélectriques pour l'automobile

Thèse soutenue publiquement le **3 novembre 2015**,
devant le jury composé de :

M. Bertrand LENOIR
Professeur, Ecole des Mines de Nancy, Président

Mme Marie-Christine RECORD
Professeure, Université Aix Marseille, Rapportrice

M. Guillaume BERNARD-GRANGER
Directeur de recherche, CEA Marcoule, Examinateur

M. Stéphane BECHU
Chargé de recherche CNRS, LPSC, Co-directeur

Mme Ana LACOSTE
Professeure, Université Joseph Fourier Grenoble, Co-directrice

Mme Laetitia LAVERSENNE
Chargée de recherche CNRS, Institut Néel, Co-encadrante

M. Franck GASCOIN
Maître de Conférences, Université de Caen Basse Normandie, Invité

M. Cédric de VAULX
Ingénieur R&D, Valéo Systèmes Thermiques, Invité

Contents

General introduction

The world is in dire need of alternative paths to pursue in terms of energy production in order to shape a moral future in which humanity minimizes the harmful impact it has on the environment and indirectly against itself. Therefore, the efforts to distance ourselves from the use of fossil fuels propel us on new planes of scientific ingenuity and research that encompass an entire spectrum of possibilities: solar energy, nuclear energy, fuel cells, hydroelectricity, wind energy and other old or emerging technologies. Among those not mentioned, a promising place is occupied by thermoelectricity. Although it is far from matching the energetic potential of other technologies, thermoelectricity stands its ground in many applications in which it can be used either as a complementary source of energy or even as the backbone behind energy production. Additionally, it can also be exploited in terms of refrigeration, paving the way to alternatives in situations where traditional refrigeration systems, such as vapor-compression-based, are not adequate or cumbersome (for example, liquid nitrogen dewars used for cooling in scientific applications). The range of applications in which thermoelectricity reveals its advantageous use is very wide, starting from powering a watch or an ebook reader to supplying the necessary power output for ensuring the functioning of space probes in their travels in the interplanetary space and beyond. The main reason why this technology flourishes is the ubiquity of heat sources that can be used in generating temperature gradients and therefore capitalizes on the analogous thermoelectric effect to produce power. Also, the temperature range for which this technology proves to be useful is very wide due to thermoelectric materials which have distinct performances at various temperatures.

One downside in using technologies based on the thermoelectricity is the low efficiency during the heat-electricity conversion, which does not exceed 10% in current commercial applications. As a result, a considerable effort is employed to improve this efficiency. This has led to the investigation of many materials and to the application of various strategies to enhance their thermoelectric properties. The main approaches which are undertaken in this context are based on separating two interconnected properties of these materials: the electrical conductivity and the thermal conductivity. In order to augment the efficiency of thermoelectric materials, the balance between the two needs to be overthrown in the favor of the electrical conductivity.

Two materials which are investigated in this work as thin films are disturbing this balance by using two separate strategies. The first strategy involves the synthesis of solid solutions based on

Mg_2Si and Mg_2Sn in order to decrease the thermal conductivity of the original thermoelectric compounds, but also to improve their electrical properties. The second strategy has a direct effect on the electrical properties by using a dopant (Sb in this case) for Mg_2Si in order to increase the carrier concentration of the material. Generally, the solid solutions are also doped to maximize the thermoelectric properties of the resulting material. The focus on the aforementioned materials is motivated, in the first part of the work shown here, by the development of a thin film-based thermoelectric module and it was initiated by their promising thermoelectric properties which were reported for bulk materials.

Furthermore, in the design of a thermoelectric module (bulk or miniaturized), it is necessary to consider the quality of the contacts between the thermoelectric materials and the electrodes to which they are connected for the delivery of power. This is significant to ensure that the performance of the thermoelectric materials is not overshadowed by the losses at the interfaces. Accordingly, it is generally required to use a functional layer between the two, whose significance is threefold: to minimize the electrical resistance of the contact, to have a good adherence to the neighboring surfaces and to act as a diffusion barrier between the two. To this end, in the second part of the work presented in this thesis, the potential as functional layers was investigated of certain materials after they were deposited as thin films on bulk thermoelectric legs.

The present thesis, with the main aims encapsulated in the previous paragraphs, is divided in four chapters as follows:

Chapter 1 offers an introduction in thermoelectricity, presenting the thermoelectric effects and their significance in refrigeration and power generation. The efficiency and the notion of the figure of merit are expanded in order to use them, especially the latter, as limits of demarcation between materials and their potential performance. The three most significant properties (electrical conductivity, Seebeck coefficient and thermal conductivity) of thermoelectric materials and their interconnection are discussed, presenting also avenues that are used for their fine tuning. Among the possible thermoelectric materials, the emphasis is placed on Mg_2Si-based materials which show promise for applications at intermediate temperatures (500-850 K). Furthermore, concerning the design and particularities of thermoelectric modules, diffusion barriers are discussed both in integrated circuits technology and the industry of thermoelectrics. Lastly, the objectives of this works are also presented, namely to investigate both the thermoelectric properties of Mg_2Si-based materials as thin films and the properties of various diffusion barriers which are meant to be implemented in the optimization of the interface between thermoelectric materials and electrodes in a thermoelectric module.

Chapter 2 presents the set of experimental methods that have been used during this work. The deposition method used for the synthesis of the thin films is described, namely microwave

plasma-assisted co-sputtering, and followed by the depiction of the characterization techniques that were employed in the investigation of the structural and thermoelectric properties of the resulting thin films: x-ray diffraction techniques (out-of-plane and grazing in-plane), SEM and EDX, four-point probes and van der Pauw methods, and the 3-ω method. Additionally, the Seebeck coefficient was also ascertained by measuring the resulting voltages from the application of a temperature gradient. Also, in the context of diffusion barrier characterization, the brazing process is described which is applied at an industrial scale by Valeo by using NOCOLOK® flux technology in a prototype furnace. The interfaces were subsequently investigated by SEM and EDX to determine their adherence to the TE legs and their chemical stability.

Chapter 3 is dedicated to the investigation of $Mg_2(Si,Sn)$ and Sb-doped Mg_2Si thin films. The description of the calibration for obtaining thin films with aimed stoichiometries is presented. First, the $Mg_2(Si,Sn)$ thin films are investigated after their deposition on multiples substrates: SiO_2/Si, borosilicate glass, MgO and Ni. The substrates were chosen to assess their compatibility with the thermoelectric materials in terms of adherence and reactivity and also based on their inherent properties suitable for thermoelectric applications either as insulators or electrodes. The structural properties and morphology of the thin films are characterized after their deposition at two distinct temperatures. The thin films are then subjected to thermal treatments in order to determine their thermal stability over prolonged periods of time, but also the degree of reactivity with the substrates. Furthermore, the transport properties (Seebeck coefficient and electrical conductivity) of the films were measured. Second, the effect of deposition temperature on the thermoelectric properties of Sb-doped Mg_2Si thin films was investigated. Accordingly, the structural and thermoelectric properties (Seebeck coefficient, electrical and thermal conductivities) of the doped thin films were explored, while also extracting the solubility limit for the Sb dopant from the transport properties.

Chapter 4 presents the two paths that have been pursued in the investigation of diffusion barriers appropriate to be used at the interface between Bi-doped $Mg_2(Si, Ge)$ thermoelectric legs and metallic electrodes. The first is based on the deposition of gradient layers that are meant to gradually inverse the composition from the Mg_2Si-based TE legs to a top layer of Ni that is used in the deposition of the potential diffusion barrier. The second path concerns the deposition of a M/Ni bi-layer on the TE legs, where M is a metallic layer (Ti, Ta, W or Cr). For testing their potential as diffusion barriers, the properties of the layers have been investigated after the brazing of the coated $Mg_2(Si,Ge)$ TE legs.

Finally, the General conclusions are presented at the end of the thesis, summarizing the results obtained in this work and presenting some perspectives. The results show how the use of $Mg_2(Si,Sn)$ in thermoelectric applications is limited in terms of thermal stability, while a potential solution lies in the variation of the composition in obtaining more stable solid solutions. Furthermore, a bi-layer of Ta

and Ni was found to be a successful candidate as a diffusion barrier in bulk thermoelectric modules based on $Mg_2(Si,Ge)$ solid solutions.

Chapter 1. Introduction

This chapter presents a basic introduction in thermoelectricity, starting with thermoelectric effects and their significance in refrigeration and power generation based on thermal gradients. The efficiency of devices that capitalize on these effects (thermoelectric modules) is approximated and the parameter (figure of merit) that characterizes all thermoelectric materials, by which their significance in applications is established, is defined.

The three most significant properties (electrical conductivity, Seebeck coefficient and thermal conductivity) of thermoelectric materials and their interconnection are discussed. The first two can be increased by the formation of solid solutions or by doping semiconductor materials. However, the decrease of the thermal conductivity poses more of a conundrum due to its direct dependence to the electrical conductivity. To this end, efforts have been focused on various paths to fine tune the lattice component of the thermal conductivity. For example, the increase of phonon scattering can be obtained by creating superlattices and nanostructures or by using materials with a high atomic mass or with complex crystalline structures (skutterudites and clathrates).

Results on the present efficiencies of thermoelectric materials are presented, emphasizing on Mg_2Si-based materials which show promise for applications at intermediate temperatures (500-850 K). Their performance is discussed based on the type of dopants used for synthesizing n-type and p-type materials and the optimum content for maximizing their transport properties.

Concerning the design and particularities of thermoelectric modules, it is shown that diffusion barriers are necessary between the thermoelectric materials and the metallic electrodes in order to preserve the overall efficiency. This is due to the failure of the contacts that occurs from poor adherence, high electrical resistance or interdiffusion which all lead otherwise to the decrease of the thermoelectric performance of the module.

At the end, the objectives of this works are also presented, namely to investigate both the thermoelectric properties of Mg_2Si-based materials as thin films and the properties of various diffusion barriers which are meant to be implemented in the optimization of the thermoelement/electrode interface in a thermoelectric module.

1.1 Basic concepts and applications in thermoelectricity

1.1.1 Thermoelectric effects

The discovery of thermoelectric (TE) effects (Seebeck, Peltier and Thomson) goes back to the beginning of the 19th century, when the link has been made between temperature gradients and electromotive forces induced or generated at the junctions of two dissimilar metals or inside semiconductors.

One way to describe the Seebeck effect is by considering a rod that is heated at one end and cooled at the other (Figure 1.1). The electrons in the heated region are more energetic and, accordingly, have higher velocities than those in the cooled region. This leads to a diffusion of the electrons from the hot side to the cold side until the electric field between the two ends stops further flow of electrons, reaching thus a stationary state. Therefore a potential difference is developed between two ends of the rod on account of the temperature difference.

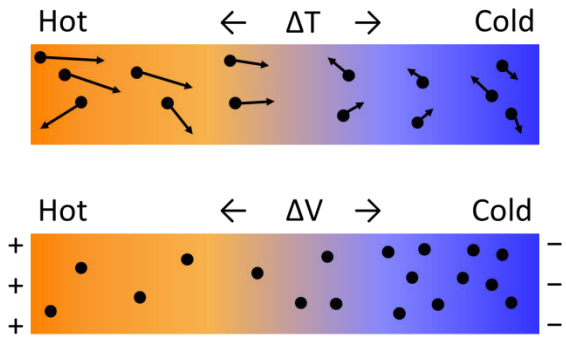

Figure 1.1. Representation of the Seebeck effect in a rod, where a temperature gradient generates a potential difference.

Another way to demonstrate the Seebeck effect is by describing the thermocouple, in which an electric potential difference (ΔV) is generated due to the diffusion of charge carriers between the junctions of two dissimilar conductors when they are subjected to different temperatures [1], as it is shown in Figure 1.2.a. The magnitude of the TE voltage, under thermodynamic equilibrium, is proportional to the difference between the temperatures of junction A and junction B (ΔT) [1]:

$$\Delta V = \alpha_{AB} \cdot \Delta T \qquad (1.1)$$

where α_{AB} is the differential Seebeck coefficient between the two materials. The Seebeck coefficient can also be defined as the entropy transported with a charge carrier divided by the carrier's charge [1]. By convention, the sign of the Seebeck coefficient is the potential of the cold side with respect to the hot side. In an n-type material the electrons diffuse from hot to cold end, making the cold side negative

with respect with the hot side ($\alpha < 0$). In a p-type material, the holes diffuse from the hot to cold end, making the cold side positive with respect with the hot side ($\alpha > 0$).

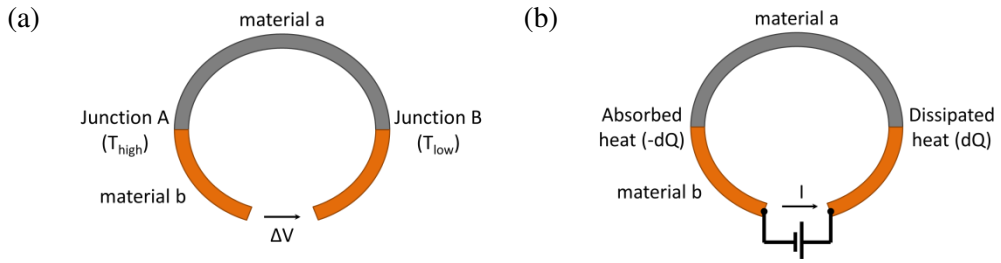

Figure 1.2. Schematic principle of (a) Seebeck effect and (b) Peltier effect.

If the two materials form a closed circuit and a current I is applied, flowing in a counterclockwise sense (Figure 1.2.b), then a rate of heating dQ/dt occurs at junction B and a rate of cooling −(dQ/dt) occurs at junction A. This forms the Peltier effect, when a heat flow is generated by the passing of the current through the circuit:

$$\frac{dQ}{dt} = \pi_{AB} \cdot I \qquad (1.2)$$

where π_{AB} is the relative Peltier coefficient of the two materials involved in the creation of the junctions. The sign of the Peltier coefficient is positive if junction A is cooled and junction B is heated and negative for the opposite.

In the case of Thomson effect, if we consider a rod of a homogeneous conductive material passed by a current (Figure 1.3), the charge carriers that travel through a region where there is a temperature gradient will absorb or dissipate energy (heat), according to their relative movement to the gradient:

$$\frac{dQ}{dt} = \beta \cdot I \cdot \Delta T \qquad (1.3)$$

where β is the Thomson coefficient, which is positive if the material absorbs heat when the sense of the current goes from the hot end to the cold end or negative if its reversed.

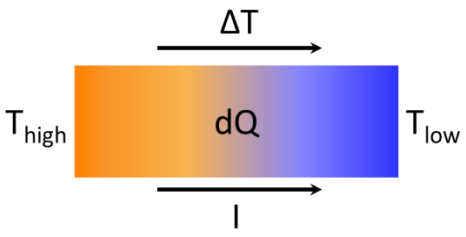

Figure 1.3. Schematic principle of Thomson effect.

Thomson also determined that all three TE effects are interconnected and discovered the so-called Kelvin relations:

$$\pi_{AB} = \alpha_{AB} \cdot T \qquad (1.4)$$

and

$$\beta_A - \beta_B = T \cdot \frac{d\alpha_{AB}}{dT} \qquad (1.5)$$

The first relation expresses the Peltier coefficient in terms of the Seebeck coefficient. This is significant due to the greater facility in measuring the Seebeck coefficient than the Peltier coefficient. The second relation connects the Seebeck coefficient with the Thomson coefficient (or rather the difference between the Thomson coefficients of the two conductors).

Further to the three TE effects mentioned above, two additional effects were observed if the materials are subjected to a magnetic field. Therefore, the Seebeck and Peltier effects have corresponding thermomagnetic coefficients, the Nernst |N| and Ettinghausen |P| effects, respectively [1]. In the case of Nernst effect, a longitudinal temperature gradient dT/dx is producing a transverse electric field E_y. The Ettinghausen effect mentions the production of a longitudinal electric current I_x by a transverse temperature gradient dT/dy. Their thermomagnetic coefficients are expressed as follows:

$$|N| = \frac{E_y/B_z}{dT/dx} \qquad (1.6)$$

and

$$|P| = \frac{dT/dy}{I_x \cdot B_z} \qquad (1.7)$$

where B_z is the z-component of the magnetic field.

However, for application purposes, the Seebeck and Peltier effects are most widely employed for energy conversion from heat to electric energy and vice-versa.

1.1.2 Thermoelectric modules (TEMs)

According to the particularities of the Seebeck and Peltier effects, they can be used for power generation (using a temperature gradient for generating an electric current) and refrigeration; respectively, by using TE converters or TE modules (TEMs). A TEM is a solid-state heat engine in which the electron gas serves as the working fluid and converts heat into electricity [1] or cools down

appropriate junctions. There are multiple advantages to using these TEMs over other systems (in Figure 1.4 are shown a few applications of these modules):

- Having no moving parts, they do not require maintenance and they have a low-noise operation.
- Based on their working principle, TEMs are smaller and lighter than conventional mechanical systems and they can also be better adapted into configurations that are required by various applications.
- They can be operated in any spatial position, being therefore desirable in various instances such as aerospace applications.
- Given their solid state construction, TEMs are highly reliable (Voyager 1 spacecraft, powered by three radioisotope TE generators, is still in operation after its launch in 1977 [2] and commercial TEMs provide long operation lifetime in the range of 100,000 to 200,000 hours [3]).
- TEMs do not generate toxic wastes, making them environmentally-friendly (if their composing materials are originally innocuous).

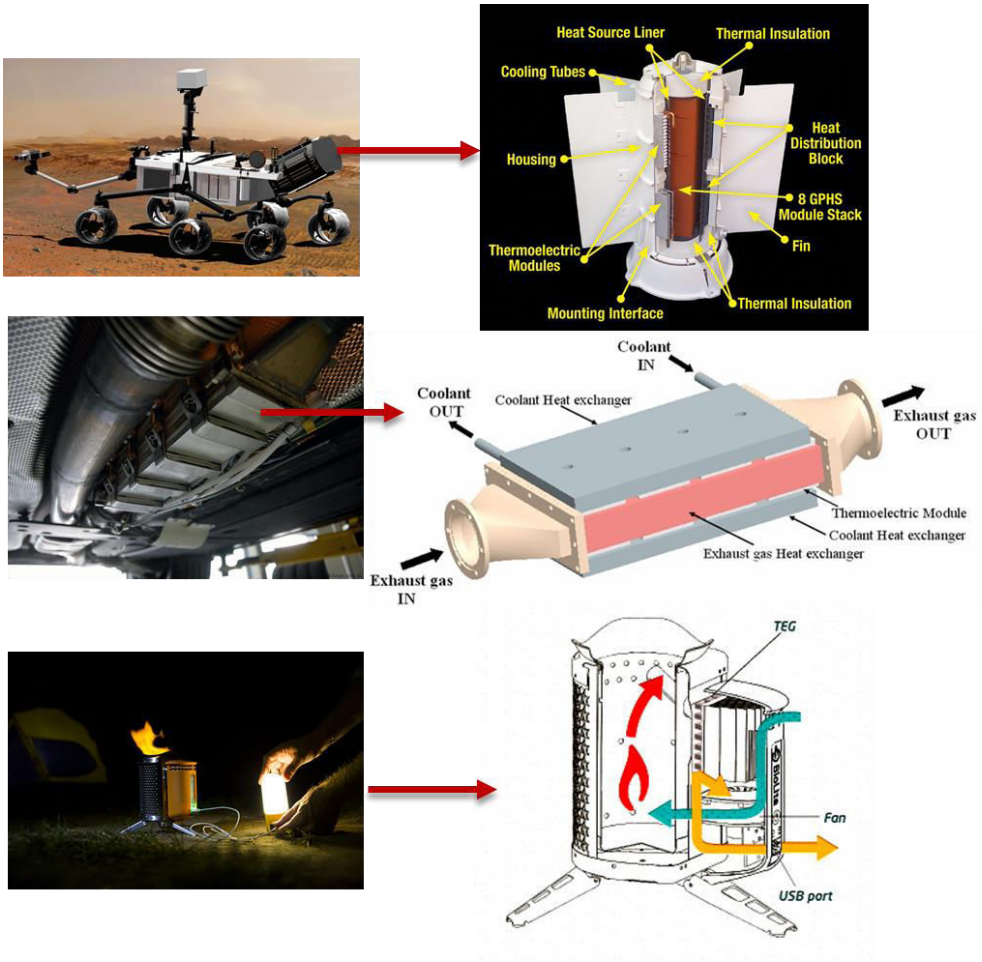

Figure 1.4. Examples of TE applications: radioisotope TEG used to power Mars rover Curiosity [4], TEG placed next to the exhaust of an automobile [5] and TEG attached to a camp stove [6].

Furthermore, energy in the form of waste heat that would be normally lost may be converted into useful electrical energy using a TE device. However, the main drawback of these devices is their low efficiency, as will be shown.

In the case of power generation, more than one material is used in the formation of a TE couple, allowing the increase of the electric potential in the presence of a temperature gradient. Therefore, two materials, n-type and p-type, are connected electrically through metallic electrical contact pads, while an external resistance (load) is connected to the circuit across the cold ends of the two thermoelements, according to Figure 1.5.a, forming the basic unit for TE applications. TE modules are made up from many thermoelectric couples (Figure 1.5.b) connected electrically in series and thermally in parallel. The number of such connections is determined by the necessary power output for specific applications or, more often, by the available thermal power that can be recovered from the system. Usually, a TE module consists of the following [3]:

- Matrix of TE elements (pellets), mainly semiconductors due to their optimal TE performance and technological properties.
- Cold and warm ceramic plates, which offer mechanical integrity, electrical insulation and good thermal conductance in order to provide heat transfer with minimal resistance.
- Electrical pads, which provide serial electrical contacting between the pellets and also contacts to leading wires.
- Leading wires, which are connected to the ending conductors and through which power is delivered.
- Solders, which ensure the assembling of the TE module.

(a) (b)

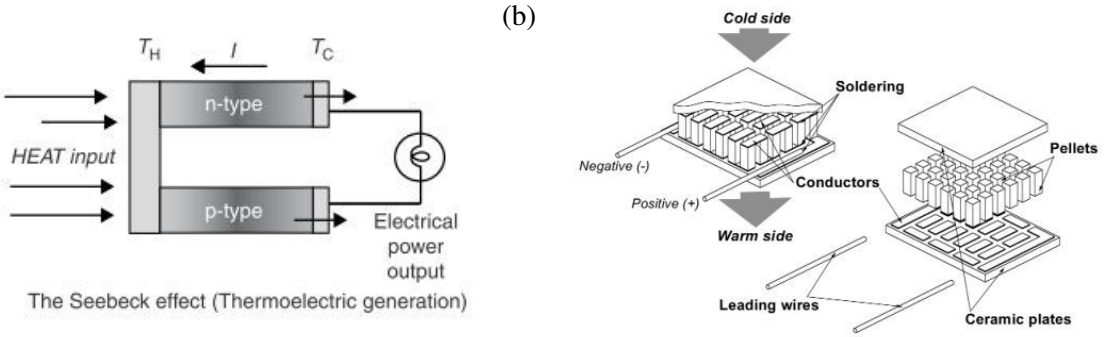

Figure 1.5. (a) Thermoelectric couple [1], (b) Thermoelectric module [3].

In order to determine the maximum power output (P_o^{max}) of a TEM, the module can be considered in a simple electric circuit as a voltage source (V) with its resistor placed in series with the load. It is also assumed that the electrical load matching condition is met, namely that the resistance of

the electrical load (R_l) equals the electrical resistance of the TEM (R_{TEM}), so the maximum power output can be determined by:

$$P_o^{max} = \frac{V^2}{4 \cdot R_l} = \frac{\left[N \cdot (\alpha_n - \alpha_p) \cdot \Delta T\right]^2}{4 \cdot \rho \cdot l/S} \quad (1.8)$$

where N is the number of TE couples contained in the module, α_n and α_p are the Seebeck coefficients of the n-type and p-type thermoelements, while ρ, l and S are the electrical resistivity, length and cross-sectional area of the N×TE couples.

Starting from the TE couple, the maximum efficiency has been deduced by Ioffe [7], by determining optimum values in the conversion process. The efficiency is defined as the ratio between the electrical power delivered to the load and the heat absorbed at the hot junction (heat input, Q_h) [1]:

$$\eta = \frac{P_o}{Q_h} \quad (1.9)$$

If we make the following assumptions: (i) the contact resistances at the two junctions are negligible, (ii) the transport properties are constant throughout the two thermoelements and (iii) approximate average values of the transport properties (electrical conductivity, Seebeck coefficient and thermal conductivity) are taken into consideration (which in reality can vary with temperature), then the efficiency can be expressed as:

$$\eta = \eta_c \cdot \frac{\sqrt{1 + Z_c \cdot \frac{T_h + T_c}{2}} - 1}{\sqrt{1 + Z_c \cdot \frac{T_h + T_c}{2}} + \frac{T_c}{T_h}} \quad (1.10)$$

where T_h is the hot side temperature, T_c is the cold side temperature, η_c is the Carnot efficiency and Z_c is the figure of merit of the TE couple.

The Carnot efficiency is a fundamental limit on the thermal efficiency of all heat engines operating in the given temperature range:

$$\eta_c = \frac{T_h - T_c}{T_h} \quad (1.11)$$

The conversion efficiency also depends on the figure of merit, which is a measure of a material's TE performance. However, the figure of merit is only meaningful if we consider both materials; n-type and p-type, in a TE couple:

$$Z_c = \frac{(\alpha_n - \alpha_p)^2}{\left[\left(\frac{\kappa_n}{\sigma_n}\right)^{1/2} + \left(\frac{\kappa_p}{\sigma_p}\right)^{1/2}\right]^2} \quad (1.12)$$

where α_n (α_p), κ_n (κ_p) and σ_n (σ_p) are the Seebeck coefficient, thermal conductivity and electrical conductivity, respectively, of the n-type (p-type) thermoelement. The figure of merit shows that the efficiency of producing electricity becomes higher as the Seebeck coefficient and electrical conductivity increase and the nonproductive losses (i.e. thermal conductivity) decrease [8]. Also, n-type and p-type materials with similar properties are usually preferred to be used in thermoelectric couples. This can be accomplished either by using different materials or by appropriately doping one material to obtain either n-type or p-type properties, according to the dopants used. This will change the figure of merit to the more usual form for a given temperature:

$$ZT = \frac{\sigma \cdot \alpha^2}{\kappa} \cdot T \qquad (1.13)$$

where $\sigma \cdot \alpha^2$ is also known as the power factor.

For practical applications, the figure of merit of materials obviously needs to be as high as possible. However, the maximum value of the figure of merit of commercialized TE materials available today is near 1. The TE conversion efficiency is displayed in Figure 1.6, determined from equation (1.9), as a function of operating temperature difference for various values of the figure of merit (for comparison, the Carnot efficiency is also indicated).

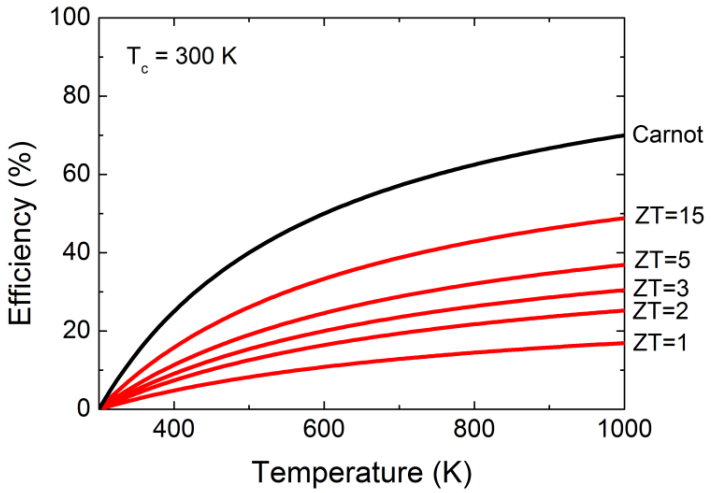

Figure 1.6. Conversion efficiency as a function of operating temperature difference.

As expected, by increasing the temperature difference, the Carnot efficiency increases as well. Therefore, for high TE efficiencies, not only high figures of merit are necessary, but also large temperature differences. Considering that for commercial applications the efficiency of thermoelectric materials ought to be at least 20%, efforts have been employed to reach into the 2-3 range of figures of merit. But there have not been a lot of success on this front, being only a few reports of ZT values exceeding 2: $AgPb_mSbTe_{2+m}$ bulk/'nanodot' material with ZT ~ 2.2 at 800 K [9], Bi_2Te_3/Sb_2Te_3

superlattice with ZT ~ 2.4 at 300 K [10], SnSe crystals with ZT ~ 2.6 at 923 K [11] and Bi-doped n-type PbSeTe/PbTe quantum-dot superlattice with a reported ZT ~ 3 at 550 K [12]. However due to different reasons, including the instability of some of the systems at high temperatures, the transition of these results to commercial applications is not yet likely and therefore, the engineering progress is limited for now to existing robust lower ZT materials.

In the case of TE refrigeration, the principle of which is based on the Peltier effect, the basic unit of a TE cooling device is shown in Figure 1.7. It is similar with that of a TE couple, with the exception that a current is passed through the circuit and therefore heat is pumped from the cold side (absorbed heat) to the hot side (dissipated/rejected heat).

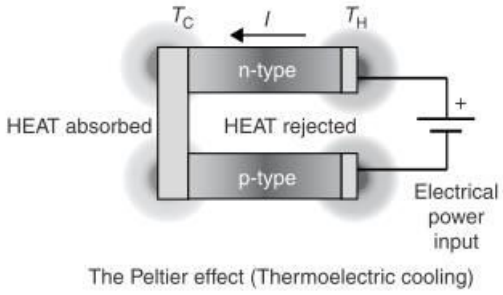

Figure 1.7. Thermoelectric refrigerator [1].

The performance of a TE cooling device is determined in general by its coefficient of performance (COP). The latter is defined as the ratio between the cooling power produced (absorbed heat, Q_a) and electrical power supplied (power input, P_i) [1]:

$$COP = \frac{Q_a}{P_i} \qquad (1.14)$$

Once again, the heat losses were considered negligible in the writing of the COP. By considering the figure of merit earlier mentioned and by optimizing the expression of the COP (determining the maximum current applied to the circuit for which the Peltier cooling effect still dominates over Joule heating), the maximum conversion efficiency is obtained:

$$COP_{max} = \frac{T_c}{T_c + T_h} \cdot \frac{\sqrt{1 + Z_c \cdot \frac{T_h + T_c}{2}} - \frac{T_c}{T_h}}{\sqrt{1 + Z_c \cdot \frac{T_h + T_c}{2}} + 1} \qquad (1.15)$$

TE cooling devices are used in many applications, although their efficiency doesn't yet match that of other refrigeration systems, e.g. using the vapor-compression cycle. Currently available TE cooling devices based on materials with a figure of merit bordering unity have an efficiency between 10-15% of Carnot (a COP between 1-1.5), compared to 60% found for vapor compression

technology [13]. Nevertheless, considering the high cooling density and the possibility to generate a temperature difference in the order of tens of degrees [14], TE refrigeration systems are used in various applications that require heat removal ranging from milliwatts up to several thousand watts. The technology is specifically suited for space applications where the temperature of critical sensors can be controlled due to precisions that can be better than 0.01 K [15].

1.1.3 Properties of thermoelectric materials: description and tailoring pathways

As was previously mentioned, the figure of merit (ZT) is the dimensionless parameter characteristic to all TE materials based on which their potential is quantified. The TE properties of materials need thus to be tuned in such way that the ZT is increased, with high electrical conductivity and Seebeck coefficient, while the thermal conductivity should be as low as possible.

The electrical properties of the three types of materials (metals, semiconductors and insulators) can be understood through their electronic band structure (Figure 1.8), based on the relative position of chemical potential (Fermi level) with respect to the conduction band and the valence band.

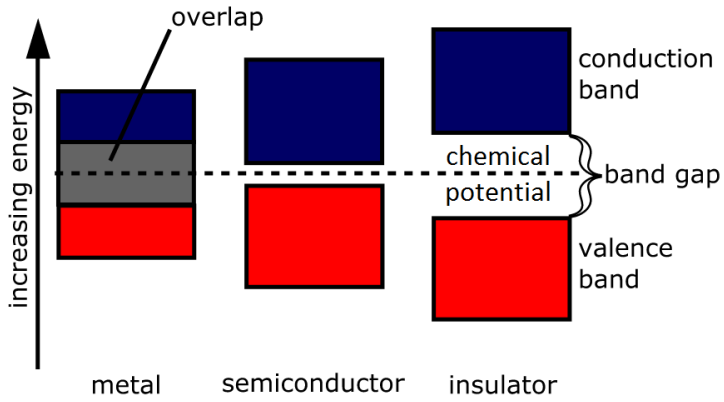

Figure 1.8. Representation of electronic band structures of metals, semiconductors and insulators.

In metals, the conduction and valence bands overlap, with the chemical potential inside. This leads to the free movement of the electrons and thus to conduction. In the case of intrinsic semiconductors, the conduction band and the valence band are separated by an energy gap of roughly 3 eV where electron states do not exist. In this case, the chemical potential is placed inside the band gap and for the conduction to start, the electrons from the valence band need to gain enough energy to cross the band gap. Therefore, the separation between bands indicates a lower conductivity in these materials. Finally, if the band gap is larger than 3 eV, then the materials are insulators. The higher band gap implies fewer electrons that can make the jump, explaining the cumbersome flow of current in this type of materials.

In Figure 1.9 is shown the dependence of the transport properties to the free carrier concentration, approximated for the three different types of materials. From there, it can be concluded that despite having a very good electrical conductivity, metals do not constitute good thermoelectric materials due to their low Seebeck coefficient and their very high value of thermal conductivity.

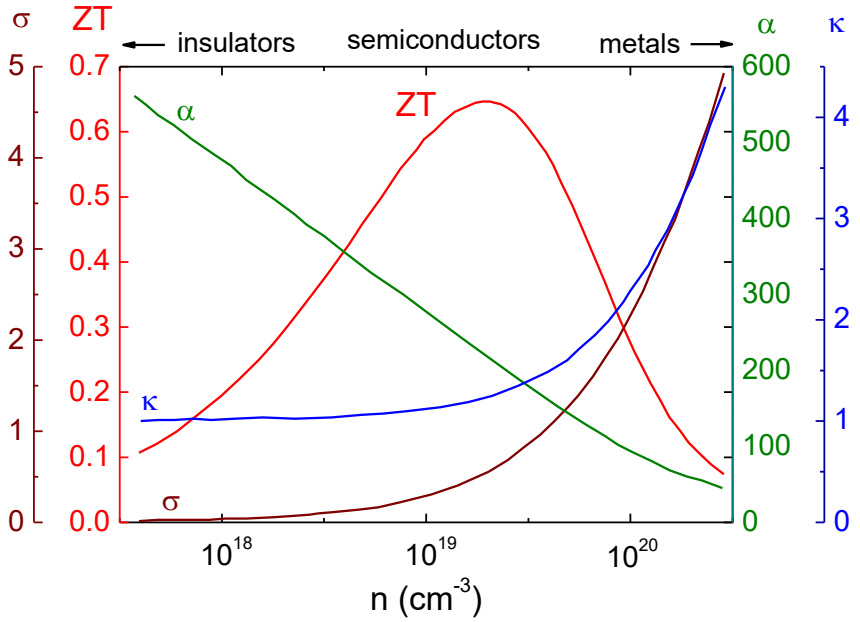

Figure 1.9. Dependence on carrier concentration (n) of electrical conductivity ($\sigma \times 10^5$, $\Omega^{-1}m^{-1}$), Seebeck coefficient (α, μV/K), thermal conductivity (κ, W/m·K) and figure of merit (ZT) [16].

On the other hand, insulators have a very high Seebeck coefficient and a very low thermal conductivity, but they do not manage to over-compensate the low electrical conductivity, which overall leads to insignificant figures of merit. Therefore, the materials that are most appropriate for thermoelectric applications are semiconductors. A clear advantage in using semiconductors, based on their intrinsic properties, is the control over their charge carrier concentration via doping, leading to high figures of merit for charge carrier concentrations in the range of 10^{19}-10^{20} cm^{-3}.

(i) Seebeck coefficient and electrical conductivity.

For the Seebeck coefficient to be large, the current transport should be determined by majority carriers throughout the material. Both n-type and p-type conduction will cancel out the voltages induced through Seebeck effect because both charge carriers will move to the cold side. For this reason semiconductors are useful, as they can exhibit primarily either electron conduction or hole conduction. In a material where both the majority and minority charge carriers are taken into account, the Seebeck coefficient is given by a weighted average of their electrical conductivity [17]:

$$S \approx \frac{S_n \sigma_n + S_p \sigma_p}{\sigma_n + \sigma_p} \qquad (1.16)$$

To allow an extrinsic conduction of the appropriate charge carrier, electrons or holes, it is required for the semiconductor to be doped with either donor or acceptor states, respectively. In other words, the aim is to have either a predominantly n-type material or predominantly p-type material.

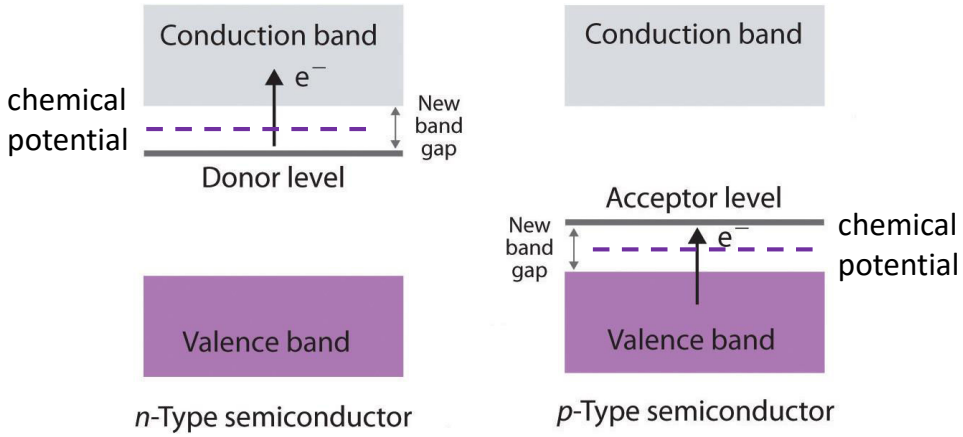

Figure 1.10. Representation of electronic band structures of n-type and p-type semiconductors.

The total Seebeck coefficient will be lower than that of either carrier unless the band gap is large enough. It was found that in the case of nondegenerate charge carriers, it is best to use semiconductors with the band gap much larger than $k_B T_0$ [8],where k_B is the Boltzmann constant $k_B = 1.38 \times 10^{-23}$ JK^{-1} and T_0 is the working temperature of the material. It was eventually derived that the optimum band gap of TE materials should be between 6 $k_B T_0$ and 10 $k_B T_0$ [18]. Having this band gap width while the chemical potential is close to the conduction or valence band due to doping (Figure 1.10), the concentration of the minority carriers are negligible (monopolar conductivity), thus leading to a higher Seebeck coefficient.

Two parameters that have a great influence on the Seebeck coefficient are temperature and carrier concentration. For most doped semiconductors, the evolution of the Seebeck coefficient with temperature is split into two regions. In the first region, the extrinsic charge carriers have priority in the conduction due to their excitation from the impurity levels. At this point, the Seebeck coefficient is increasing with temperature as the chemical potential is getting further away from the conduction band (n-type materials). This can be understood by following the reasoning behind the shift of the chemical potential with respect to the conduction band, for example, with temperature. At low temperatures, the ionization coefficient is low, which means that most of the donor states are still filled. Given its definition, the chemical potential is positioned, in this case, above the donor level. The second region is reached by continuing to increase the temperature. This also increases the ionization coefficient with

more electrons leaving the donor states by jumping in the conduction band, until all these states are empty. As a result, the chemical potential will shift lower than the donor level until it reaches very close to the intrinsic position. In other words, by increasing the temperature, the chemical potential will shift from a position very close to the conduction band to a position close to the middle of the band gap (intrinsic Fermi level). Thus, electron-hole pairs are formed across the band-gap which will decrease the Seebeck coefficient because of the presence of both types of carriers. Therefore, between these two regions there is a point where the Seebeck coefficient has a maximum value. This is better pictured considering that the Seebeck coefficient is proportional to the difference between the average carrier energy and Fermi energy (the separation between the chemical potential and the edge of the conduction band) [19]. This whole discussion can be applied to p-type materials as well.

There is also a strong correlation between the Seebeck coefficient and the carrier concentration according to [20]:

$$\alpha = \frac{8\pi^2 k_B^2}{3eh^2} m^* T \left(\frac{\pi}{3n}\right)^{2/3} \quad (1.17)$$

where m^* is the density-of-states effective mass of the carrier and n is the carrier concentration. This means that low carrier concentration will lead to high Seebeck coefficients. However the carrier concentration is connected to electrical conductivity as well through the carrier mobility μ:

$$\sigma = ne\mu \quad (1.18)$$

The opposing effect that the carrier concentration has on both TE parameters makes it difficult to increase the power factor at a high extent. Additionally, the effective mass of the charge carrier also leads to further conflicts [21]. Increasing the density-of-states effective mass (in the case of flat and narrow bands with high density of states at the Fermi level) translates, as it will be shown next, into a higher Seebeck coefficient. On the other hand, due to the relation between density-of-states effective mass and inertial effective mass, heavy carriers will move with slower velocities (mobilities) and therefore lead to lower electrical conductivities. Therefore, a balance needs to be found while manipulating materials, to find a compromise between the high effective mass and high mobility of the dominant charge carriers. This can be usually done by using materials which are based on elements with a small difference in their electronegativity (for high mobilities and low effective mass) or materials with narrow bands (for high effective masses and low mobilities).

The power factor can be optimized and maximized within the limitations and, as shown in Figure 1.9, this happens at a carrier concentration of about 10^{26} m^{-3}, corresponding to heavy doped semiconductors. This can also be understood under the concept of density of states. In a doped semiconductor the density of states curve is asymmetric in relation to the chemical potential, given its proximity the conduction band. In other words, there are more states available for transport above the

chemical potential than below it (for an n-type material). However, as the doping of the material is increased (higher carrier concentration), the energy states of the charge carriers are becoming degenerate as the chemical potential shifts inside the conduction band. If the Fermi energy is higher than k_BT, the density of states curve is becoming symmetrical, decreasing the Seebeck coefficient. Also at such concentrations and positions of the chemical potential, the energy of the charge carriers is almost independent of the temperature, which will make the electronic flows in the material, both at the hot side and the cold side, almost identical. Figure 1.11 is a representation of this decrease observed for n-type materials with respect to the Fermi level and conduction band (E_F-E_c), according to calculations [22]. It is obvious that although the electrical conductivity is increased, the augmentation of the carrier concentration is by no means beneficial to the Seebeck coefficient.

For clarification, k_BT is used as reference because it helps to determine the probability of available states that can be occupied at certain energy (E) in the Fermi-Dirac distribution (used for charge carriers such as electrons):

$$f(E) = \frac{1}{1 + exp\left(\frac{E-\mu}{k_BT}\right)} \qquad (1.19)$$

where μ is the chemical potential.

Accordingly, the power factor can be improved through lower-dimensional semiconductors by creating sharp features in the electronic density of states [23]. This whole discussion can be extended to p-type materials as well.

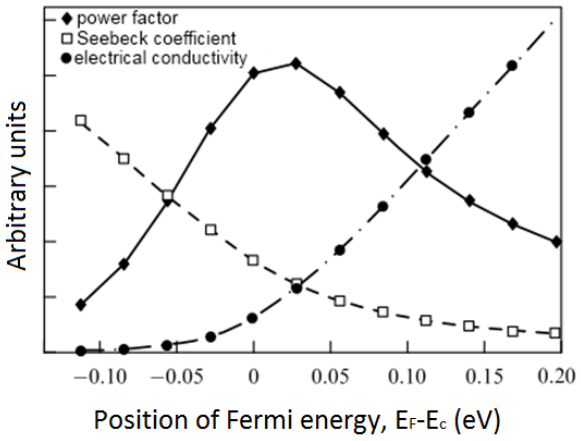

Figure 1.11 - Seebeck coefficient, electrical conductivity and power factor with respect to Fermi energy (E_F) and conduction band (E_c) [22].

Therefore, the best way to obtain high power factors and high figures of merit is by optimizing the semiconductors with respect to their evolution with temperature and carrier concentration:

- increase the temperature as much as possible before electron-hole pairs begin to have a contribution on the overall conduction (a relatively large band gap is also implied for doped semiconductors);
- increase the carrier concentration by doping to have a maximum electrical conductivity just at the point where the impurity levels are merging into a band and start behaving more like a conductor, before losing its favorable TE properties with the further decrease of the Seebeck coefficient (the peak of the power factor observed in Figure 1.11).

(ii) Thermal conductivity.

Another aspect of TE materials that has to be dealt with in order to maximize their figure of merit is the thermal conductivity. To this end, this property characteristic to all materials has to be lowered as much as possible, keeping in mind that there are two contributions to the overall thermal conductivity from: electrons and holes that transport heat (κ_e) and phonons that travel through the lattice (κ_l):

$$\kappa = \kappa_e + \kappa_l \qquad (1.20)$$

The electrical contribution to thermal conductivity κ_e is dependent on the electrical conductivity σ according to the Wiedemann-Franz relationship, making the ratio κ_e/σ constant at a given temperature for most of the TE materials:

$$\kappa_e = L_0 \sigma T \qquad (1.21)$$

The value of the Lorenz number is $L_0 = 2.48\times10^{-8}\ V^2K^{-2}$ for metals and usually is considered to be $2\times10^{-8}\ V^2K^{-2}$ for highly doped semiconductors. This relationship shows that increasing the electrical conductivity leads also to the increase of the electronic thermal conductivity, which cannot be remediated or counterbalanced. Therefore the only path that can guarantee the minimization of the total thermal conductivity is focusing on the phonon contribution.

The minimum possible lattice thermal conductivity is achieved in the case in which all the phonons have a mean free path equal to the interatomic distance between the constituent atoms [24]. The lattice thermal conductivity is given by

$$\kappa_l = \frac{1}{3} v_s C_V \lambda_p \qquad (1.22)$$

where v_S is the velocity of sound, C_V is the heat capacity at constant volume and λ_p is the mean free path of the phonons. At temperatures higher than the room temperature, the sound velocity and the heat capacity are independent of temperature, which means that the value of the lattice thermal conductivity is basically determined by the mean free path of the phonons.

Also due to the fact that the lattice thermal conductivity is almost completely independent of the charge carrier concentration, which has a great contribution in the interdependence of the other TE parameters, the notion of phonon glass-electron crystal (PGEC) has arisen [25]. This implies that the best possible TE material would have the electrical properties of a crystalline material and the thermal properties of an amorphous, glass-like material.

There are a number of possibilities in lowering the lattice thermal conductivity. One first option entails the use of materials made of elements with high atomic mass [7]. Using 'heavy' atoms means the lattice frequency is reduced in a wide range of temperature. However, the use of such elements also translates in a higher scattering cross-section for charge carriers, which leads also to a decrease of the electrical conductivity.

A second option is using the aforementioned concept of PGEC by creating complex crystal structures, which are intended to decouple the thermal and electrical properties. Three new classes of TE materials have emerged using this concept: skutterudites [26], clathrates [27] and TE cobaltite oxides [21]. In the first two types of materials, the decoupling is successfully accomplished via the conception of large voids (cages) inside the structures which can be filled with heavy atoms. Because of their weak bonding inside the cages, these atoms will have certain degrees of freedom in movement which means that they will effectively disperse phonons by rattling (hence their description as 'rattlers'). A clear correlation has been observed between the size and the vibrational motion of the rattlers and the thermal conductivity, promising high figures of merits [21]. In the case of TE cobaltite oxides (Na_xCoO_2 and Ca-Co-O-based materials), the Co-O layers form metallic layers which are separated by insulating, disordered layers, leading to PGEC characteristics.

A third option is via nanostructuring TE materials. This can be accomplished either by creating a matrix of nanosized particles grains or by embedding a minor second phase in the bulk matrix via precipitation from solid solution [28]. The lattice thermal conductivity is lowered in such materials due to the enhanced phonon scattering by interfaces and the nanoinclusions which act as scattering centers [29].

Another option is based on what is known about semiconductors: the electronic wavelength is much larger (10^{-8} m) than the interatomic distance, while most lattice vibrations occur at wavelength that is of the order of the lattice constant (10^{-10} m). This great difference between electron waves and phonons can suggest the idea of structures which will be effective in scattering phonons without any influence on the electrons. The scattering of the phonons can be accomplished by creating nanoscale superlattices (alternating thin layers of different materials stacked periodically) or by creating structures which involve inhomogeneities introduced in the lattice, like punctual defects. The latter can be done by inserting impurity atoms inside the material or by the formation of solid solutions, based on compounds that crystallize in similar structures. The effectiveness of this method is given by the

mass fluctuations that are formed inside the solid solutions which act just as punctual defects and manage to hinder the propagation of the phonons, thus decreasing the thermal conductivity. Although this path also presents the inconvenient of affecting the electrical conductivity by decreasing the carrier mobility, there is a solution that proved to reduce the dispersion of the charge carriers: using as substitution an element that is in the same group in the periodic table with one of the elements from the initial compound. This method has been widely used in the efforts to reduce the thermal conductivity and it proved to be most efficient.

Given the behavior of TE materials and their interdependent properties, the best approach in improving the former is by selecting a material that already has a favorable electrical/thermal conductivity ratio and then optimize its composition by doping in order to increase the density of states around the chemical potential, thus increasing the figure of merit.

1.1.4 Thin film based integrated thermoelectric modules

The ongoing miniaturization of electronic systems is accompanied by heat generation that can lead to significant increases in temperatures. This rise can cause failures for situations in which the temperatures that can be tolerated are quite limited and therefore heat management is very important. In other systems, heat losses are unavoidable, but they can be capitalized by using small TE devices for power generation. A recent approach in overcoming these thermal concerns is by using thin film TE devices.

The greatest advantage of using thin films lies in the potential of a high power density due to the inversely proportional dependence of the heat flux with the thickness of the material. This allows pumping a maximum heat flux of 100-400 W/cm^2, compared to less than 10 W/cm^2 for conventional bulk TE devices [30], as it can be seen in Figure 1.12.

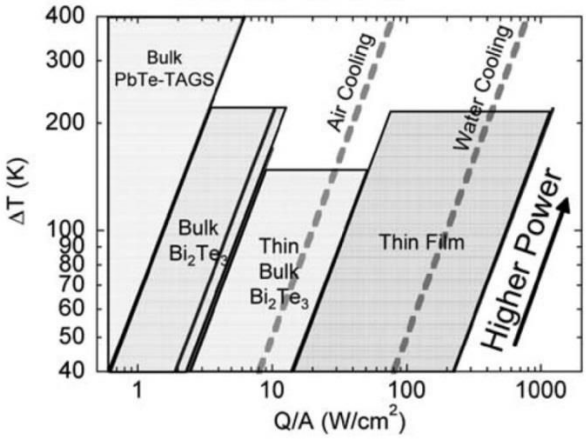

Figure 1.12. Comparison between bulk materials and thin films
based on their potential in achieving high power of density (Q/A) [31].

Moreover, it was theoretically deduced that in order to achieve power densities higher than 500 W/cm^2, the thickness of the thermoelectric material ought to be lower than 50 µm [32]. As a result, for example, a very high heat flux (~1300 W/cm^2) was achieved by using 5-8 µm thick Bi_2Te_3 superlattice based thin film TE coolers [32]. Additionally, thin film-based TEMs maintain a precise temperature control due to the low reaction times in the range of microseconds, which enables superior switching speed during the heating and cooling cycles in various applications that involve refrigeration.

Scaling down to thin films also allows manipulating the thermal conductivity beneficial for the TE properties of the materials. The grain size can be lowered down to nanometer scale in thin films, such that the scale is similar to that of the mean free path of phonons. Therefore the lattice thermal conductivity is reduced, which is of course beneficial to the overall TE properties of the material. For example, the effect of grain size on thermal conductivity has been investigated on Sb_2Te_3 thin films [33] and it was determined that values as low as 2 W/m·K can be obtained by reducing the grain size down to ~90 nm, compared to 4.6 W/m·K [34] for bulk materials. This, as was previously mentioned, can be accounted by the enhanced boundary scattering that follows the decrease in grain size. There have been examples of superlattices that can also be used for the same objective. For in-plane configurations, the thermal conductivity is decreased due to the interface scattering between the layers, but the electron performance is also enhanced due to the quantum size effects (sharp features in the electron density of states) [35]. For cross-plane configurations, the interfaces between layers are used once again for phonon scattering, while allowing the electrons to pass (phonon-blocking/electron-transmitting). These mechanisms have been capitalized through the elaboration of superlattice systems that led to figures of merit exceeding unity [10, 12].

1.2 Mg_2Si-based thermoelectric materials: properties, dopants and potential

In the search for highly efficient TE materials, Mg_2Si-based materials have attracted attention and especially $Mg_2Si_{1-x}Sn_x$ solid solutions have proved to be the most promising candidates for TE applications (at temperatures between 500 K and 850 K) according to a somewhat extended research that has been done lately, once the interest on these materials was revived last decade [36]. This interest is based on their TE properties, but also on the abundance and lightweight of its component elements and the fact that they constitute an environmentally friendly material.

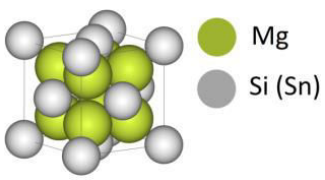

Figure 1.13. Mg_2Si (Mg_2Sn) crystal structure.

The Mg_2Si and Mg_2Sn compounds crystallize in an anti-fluorite cubic structure (Figure 1.13), both having unsettled lattice parameters with values reported of 6.39 Å [37] and 6.35 Å [38] for the former and values ranging between 6.75-6.77 Å [39] for the latter. Also, as it can be seen in Table 1.1, the compounds have promising band structures due to their relatively large band gaps (0.77 eV and 0.35 eV) and high carrier mobilities, leading to a good electrical conductivity according to relation 1.17.

Table 1.1. Parameters of the band structure of Mg_2Si and Mg_2Sn [39].

Compound	E_g (eV)	ΔE (eV)	μ_n (300K) ($cm^2/V{\cdot}s$)	μ_p (300K) ($cm^2/V{\cdot}s$)	κ_L ($W/m{\cdot}K$)
Mg_2Si	0.77	0.4	405	65	7.9
Mg_2Sn	0.35	0.016	320	260	5.9

In the case of Mg_2Si, extended work has been employed in the investigation of its TE properties. More specifically, the properties of Mg_2Si were further enhanced by the addition of various dopants in the effort of synthesize n-type thermoelements. A summary of the most significant and representative results on the TE properties of doped Mg_2Si bulk compounds can be found in Table 1.2, where Sb, Bi and Al were tested as dopants to generate n-type materials. The figures of merit are relatively high for temperatures that generally exceed 800 K, with values like 0.77 for Sb-doped materials, 0.86 for Bi-doped materials and 0.62 for Al-doped materials. These results were reported for optimized compositions in the respective works. The dopants are improving the electrical properties predominantly by increasing the carrier concentration of the initial material.

Table 1.2. Maximum figures of merit and corresponding power factors obtained for optimum bulk $Mg_2Si_{1-y}D_y$ materials (where D is Sb, Bi or Al)

Dopant	y content	Power factor (10^{-3} $W/m{\cdot}K^2$)	ZT_{max}	T_{ZTmax}	Ref.
Sb	0.015	3.15	0.77	862	[40]
	0.015	3.30	0.585	650	[41]
	0.02	2.45	0.56	862	[42]
	0.02	2.24	0.62	823	[43]
Bi	0.06	3.12	0.86	862	[44]
	0.06	3.5	0.74	840	[45]
Al	0.02	2.4	0.58	844	[46]
	0.06	2	0.62	855	[47]

However, the results vary from one report to another for the same composition on account of the synthesis method which can affect the general TE properties of the materials. For example, some methods (fusion, mechanical alloying or spark plasma sintering) make it difficult to properly control the composition of the compound or to adjust the relationship between structure and performance. This is caused by the oxidation and volatilization of Mg or due to different melting points and specific gravities of the initial materials (Mg, Si and dopants) [41]. Furthermore, there have been instances in which the transport properties of the resulting materials could vary not only based on the fabrication method, but also on the process parameters such as sintering temperature, sintering time and the gas in which they are synthesized [42], making the production of these TE materials with optimum and reproducible properties all the more precarious.

Nevertheless, regardless of the methods employed or even the TE properties, the choice of materials that are to be implemented in the formation of thermoelements is based on factors such as thermal stability and long-lifetime operation at elevated temperatures [47]. Accordingly, further tests in the stability of the aforementioned dopants showed that Bi exhibits local precipitation during operation at elevated temperatures and ultimately to the degradation of the structural and TE properties of the material [47]. As for the other two, Sb-doped materials proved to be much more stable at high temperatures than Al-doped Mg_2Si [48], increasing the likelihood of using Sb rather than the others in the synthesis of n-type Mg_2Si materials.

However, although doping Mg_2Si can lead to promising results in the context of thermoelectricity, there are other ways in which the properties of Mg_2Si-based materials can be augmented, as it will be next indicated.

(i) $Mg_2Si_{1-x}Sn_x$ solid solutions

As was shown in Table 1.1, the band structures of Mg_2Si and Mg_2Sn promoted good electrical properties. However, it is also shown that the thermal conductivities of these materials are quite high as well, making room for additional improvements other than, for example, merely doping. Therefore, a new path can be capitalized for increasing the figure of merit that these materials could have and this can be achieved through the formation of solid solutions based on these two compounds.

By creating solid solutions, the thermal conductivity is decreased due to the enhanced point defect phonon scattering stemmed from the great difference in atomic mass between Si and Sn atoms (m_a^{Si} = 28.0855 and m_a^{Sn} = 118.71). Also, by having both atoms in the unit cell will lead to strain fluctuations inside the lattice which as well have an impact in the scattering of phonons throughout the material.

An important feature of both compounds that can be effectively exploited is the presence of a second band above the minimum conduction band separated by ΔE of 0.4 eV and 0.016 eV for Mg_2Si and Mg_2Sn, respectively [36]. The lowest conduction band (C_1) is determined by Si states in the first

compound and by Mg states in the second (Figure 1.14.a). This separation is significant in the context of solid solutions by observing the evolution of their band structure as a function of Sn content based on Figure 1.14.b.

By increasing the content of Sn, a narrowing of the conduction gap is eventually observed until a band inversion occurs, at which point both conduction bands are separated by the same energy gap from the valence band (V_1, V_2, V). In other words, both bands offer the same contribution to the electrical conductivity. This has a great significance over the TE properties of the material due to the increase of the density of states near the Fermi level (translating into a higher Seebeck coefficient) without being detrimental to the overall electron mobility. Consequently, the optimization of the band structures of $Mg_2Si_{1-x}Sn_x$ solid solutions contributes to the enhancement of the figure of merit.

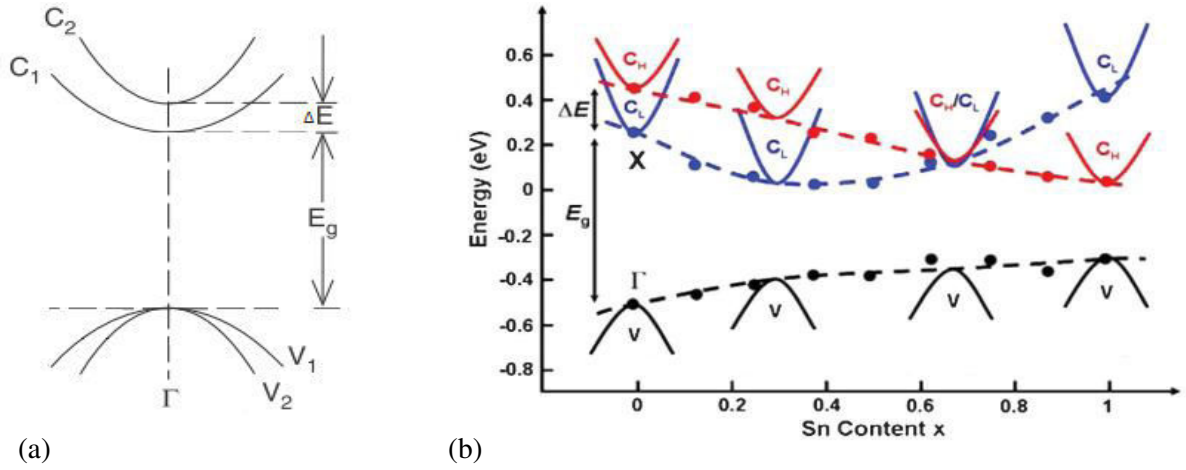

Figure 1.14 - (a) Representation of the band structure of Mg_2Si and Mg_2Sn;
(b) Evolution of the band structure of $Mg_2Si_{1-x}Sn_x$ solid solution with Sn content [49].

Therefore, considering the decrease of thermal conductivity, the increase of Seebeck coefficient by choosing the right composition and the possibility of doping in order to obtain n-type or p-type materials, $Mg_2Si_{1-x}Sn_x$ solid solutions are promising materials for TE applications.

Additionally, according to the phase diagram of Mg_2Sn-Mg_2Si from Figure 1.15, the two phases form a ternary solid solution only for certain compositions. A miscibility gap has been reported in a number of studies [50-53], but with its range being highly disputed. For example, the edges of the miscibility gap are $Mg_2Si_{0.4}Sn_{0.6}$ and $Mg_2Si_{0.6}Sn_{0.4}$ according to Nikitin et al. [50] or $Mg_2Si_{0.4}Sn_{0.6}$ and $Mg_2Si_{0.9}Sn_{0.1}$ from the work of Muntyanu et al [51]. Even more disjointed results can be extracted from the works of Riffel and Schilz [54] or Kozlov et al. [52] who reported gaps for a Si content between 0.09-0.72 and 0.21-0.88, respectively.

However, as it will soon be shown, single phased solid solutions were reported with various compositions, including $Mg_2Si_{0.5}Sn_{0.5}$ [55, 56], raising the possibility of stabilizing the material for any Si content by the method of synthesis (liquid-solid reaction, B_2O_3 flux sintering, etc.).

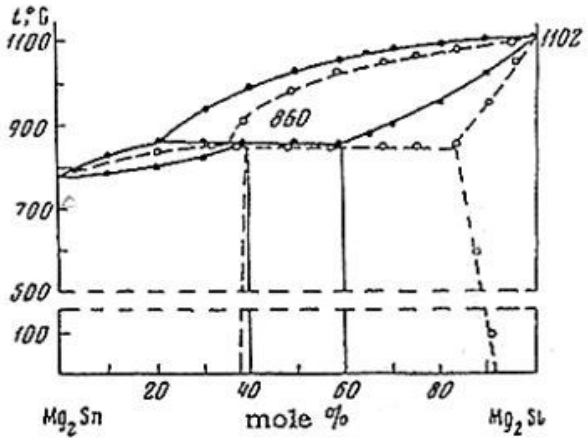

Figure 1.15. The pseudo-binary phase diagram of Mg_2Sn-Mg_2Si system, as determined by Nikitin et al. [50] (solid lines) and Muntyanu et al. [51] (dashed lines).

The search for the composition of $Mg_2Si_{1-x}Sn_x$ solid solutions which present the best TE properties has been coordinated alongside the research for dopants that could maximize the properties of the materials. This is because creating efficient TE devices can only be accomplished by using both p-type materials and n-type materials and their TE performances have to be on a par with each other. To this end, the improvement of both types has been investigated through the means of doping $Mg_2Si_{1-x}Sn_x$ solid solutions.

(ii) N-type $Mg_2Si_{1-x}Sn_x$ solid solutions

For n-type materials it was found that doping with Sb, Bi and La is effective, while for p-type materials, doping with Ag and Li. The most extended work was done on the Sb-doped $Mg_2Si_{1-x}Sn_x$ solid solutions at different values of Sn concentration. Sb doping introduces a large number of short-range disorder structures (point defects and lattice distortion) that favors and enhances the scattering of the phonons due to the mass and size difference between substituting atoms (Sb) and host atoms (Si) [57]. As an immediate effect, the thermal conductivity is decreased by Sb-doping, but it also has a significant influence on the band structure and the electrical properties of the $Mg_2Si_{1-x}Sn_x$ TE materials.

The first inquiries were done on bulk materials using Sb as dopant and the best TE properties at high temperatures were obtained for $Mg_2Si_{0.4}Sn_{0.6}$ and $Mg_2Si_{0.6}Sn_{0.4}$, which in the temperature range 400-850 K had the average values of ZT about 0.83 for $x = 0.6$ and 0.78 for $x = 0.4$ (with $ZT_{max} = 1.1$ for the latter at ~750 K) [36]. These results are conveyed in Figure 1.16 based on different electron concentrations at high temperatures. Thus, it was proved from the beginning that the $Mg_2Si_{1-x}Sn_x$ solid solutions show very good TE properties for Sn content $0.4 \leq x \leq 0.6$ which is not surprising considering the later analysis of their band structure [49], where it was concluded that the band inversion occurs at $x \approx 0.6$-0.65 (Figure 1.14.b). In this investigation on the optimization of the band structure it was reported that the highest figure of merit, based on Sn content, was obtained for the

$Mg_2Si_{0.4}Sn_{0.6}$ solid solution with a value of ZT = 1.3 at 750 K (with similar performances for $Mg_2Si_{0.3}Sn_{0.7}$ as well). This value has been reached by Sb-doping after it was established that the best TE performance occurs when the electron density is close to 2×10^{-26} m^{-3}. Furthermore, in more recent reports, values for the figure of merit of as high as 1.5 were obtained for $Mg_{2.08}Si_{0.4-x}Sn_{0.6}Sb_x$ [58] and 1.4 for $Mg_2Si_{0.5875}Sn_{0.4}Sb_{0.0125}$ [59].

Although the best results were obtained for $Mg_2Si_{0.4}Sn_{0.6}$ solid solution (Table 1.3), the effect of Sb used as dopant on the improvement of the TE properties was established for all the materials with different Sn concentration. For example, in the case of $Mg_2Si_{0.3-y}Sn_{0.7}Sb_y$ [60], the effect of Sb on the electron concentration is obvious, considering its increase over three orders of magnitude compared with the un-doped material (from $n = 10^{23}$ m^{-3} for un-doped material to $n = 10^{26}$ m^{-3} for y = 0.025). Thus, although the Seebeck coefficient has the tendency to decrease with the addition of the dopant (as expected), the power factor is vastly increased (over six times larger). Accordingly, it would have been only logical to assume that by increasing the dopant, the electron concentration would further increase. However in numerous reports [55, 60-62] it was observed that increasing the amount of dopant will ultimately decrease the carrier concentration and so reverse the process that led to high power factors (high figures of merit). This has been explained [61] as a result of the vacancies that are increasingly created at Mg sites with higher Sb concentration. As it will be explained later, these vacancies create electron acceptor states and counterbalance the contribution from the Sb donors.

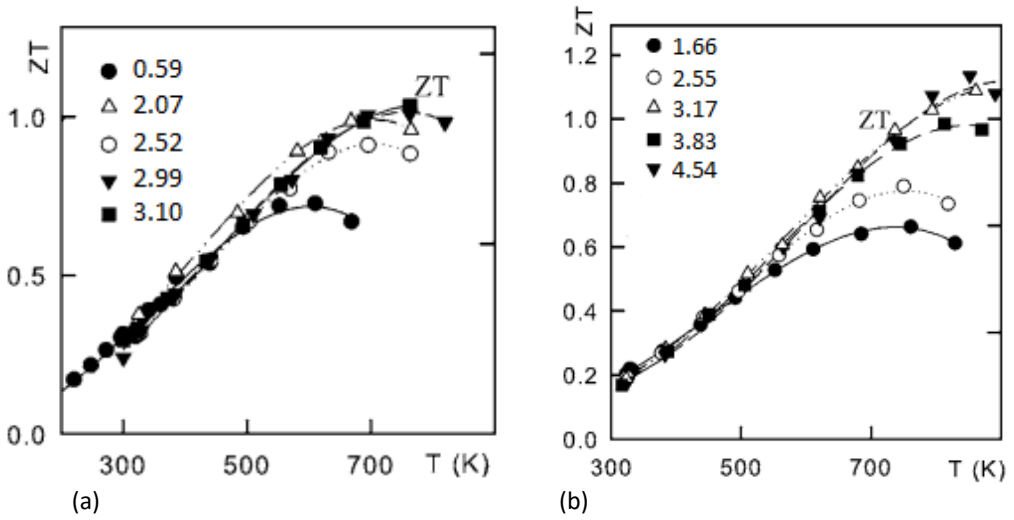

Figure 1.16. Temperature dependence of the figure of merit of (a) $Mg_2Si_{0.4}Sn_{0.6}$ solid solutions and (b) $Mg_2Si_{0.6}Sn_{0.4}$ solid solutions for different electron concentrations (n, 10^{26} m^{-3}) [36].

This also implies a solubility limit whereby Sb forms a secondary phase. In other words, below the solubility limit the TE properties are improving along with the increase of the Sb-doping fraction, while they start to deteriorate after exceeding it. In the case of $Mg_2Si_{0.3-y}Sn_{0.7}Sb_y$ this happens after exceeding y = 0.025, but overall the solubility limit depends on the composition of the solid

solution. Therefore the TE properties can be efficiently enhanced only by precisely altering the Sb doping content.

Other attempts to improve the properties of $Mg_2Si_{1-x}Sn_x$ solid solutions (as n-type materials) have been led by using Bi and La as dopants. Bismuth was considered as a candidate because of its larger radius and heavier mass, the exact reasons for which Sb-doping proved to be efficient. Although the work on Bi-doped materials hasn't been as extensive as on Sb, it is evident that for $Mg_2Si_{0.8}Sn_{0.2}$ it is almost just as adequate with a ZT = 1.17 at 850 K [63]. However, the Bi-doped materials show a lower electrical conductivity compared to Sb-doped compounds, which is most likely caused by being more difficult for Bi electrons to transit to the conduction band than for Sb electrons due to the higher energy barrier between the impurity level and the conduction band.

Table 1.3. Maximum figures of merit obtained for n-type $Mg_2Si_{1-x}Sn_x$ solid solutions.

Solid solution	ZT_{max}	T_{ZTmax} (K)	Dopant	Report
$Mg_2Si_{0.3}Sn_{0.7}$	1	640	Sb	[60]
$Mg_2Si_{0.4}Sn_{0.6}$	1	750	Sb	[36]
	1.1	780	Sb	[62]
	1.3	750	Sb	[49]
	1.5	716	Sb	[58]
$Mg_2Si_{0.5}Sn_{0.5}$	1.1	620	Sb	[56]
	1	760	Sb	[55]
$Mg_2Si_{0.6}Sn_{0.4}$	1.4	780	Sb	[59]
	1.1	750	Sb	[36]
	1.1	860	Sb	[57]
	0.65	700	Bi	[64]
	0.81	810	La	[65]
$Mg_2Si_{0.7}Sn_{0.3}$	0.54	650	Sb	[55]
$Mg_2Si_{0.8}Sn_{0.2}$	1.17	850	Bi	[63]

As for La as dopant, the effort proved to be less impressive in comparison with the previous research mentioned, considering that the maximum ZT obtained was 0.81 at 810 K [65].

Recently, a study on Sb-doped $Mg_2Si_{1-x}Sn_x$ solid solutions was also done for thin films [66]. The Sn concentrations on which this report was focused are x = 0.4, 0.5 and 0.6 and for all un-doped samples the charge concentration is of the order of 10^{24} m^{-3}, a bit higher than the values obtained for bulk materials of the same composition [56, 57, 62, 65]. For the case of doped samples, the maximum charge concentration 4×10^{25} m^{-3} was obtained for $Mg_2Si_{0.6}Sn_{0.4}$ composition. This is one order of magnitude lower than the value connected to the best figure of merit of a bulk material with the same

Sb doping fraction. Also, the electrical conductivity of thin films is lower than for bulk materials, which may be explained by the increased grain boundary scattering as a result of decreased grain size and by their lower density that leads to low charge mobility [67]. Overall, the TE performance of the thin films is lower than their equivalent in bulk. However, there is still room for improvement of the thin films in terms of morphology and density [66] which could lead to better results.

(iii) P-type $Mg_2Si_{1-x}Sn_x$ solid solutions

The research on p-type $Mg_2Si_{1-x}Sn_x$ solid solutions was less extended, however the effect of Ag and Li double-doping on TE performance was investigated [68]. It was observed that double doping is effective in increasing the carrier concentration, which results in the reduction of the Seebeck coefficient and an increase of electrical conductivity and because of the larger atomic radius and atomic mass of Ag than those of Li, the addition of Ag proved effective in reducing the thermal conductivity. However, these improvements are happening at a small scale, with minute differences between TE properties.

The efficiency of Ag in the search for good p-type TE materials is more obvious in working with thin films [69]. A significant increase in electrical conductivity was shown through the addition of Ag compared to un-doped materials for different Sn compositions (two orders of magnitude difference). Once again, doping $Mg_2Si_{0.4}Sn_{0.6}$ results to most enticing properties.

Overall, it seems that fine tuning the Sn concentration close to 0.6 in $Mg_2Si_{1-x}Sn_x$ system leads to promising TE properties evident in bulk and evocative in thin films, which favor its choosing for further use in the elaboration of TE devices, while Sb and Ag are the main candidates in the development of n-type and p-type materials.

(iv) Effect of Mg content on the thermoelectrical properties of $Mg_2Si_{1-x}Sn_x$ solid solutions

In the case of bulk materials, the elaboration of $Mg_2Si_{1-x}Sn_x$ solid solutions proved to be problematic due to the emergence of MgO and also to the evaporation of Mg during synthesis. An obvious solution to counteract the latter issue that has been applied with regularity is the addition of extra Mg at the beginning of the process. This led to the quantification of the impact that Mg has on the TE properties of $Mg_2Si_{1-x}Sn_x$ solid solutions.

The Mg excess leads to interstitial Mg and Si-Sn vacancies, while Mg deficiency results in Mg vacancies and Si substitution in Mg lattice. This change of the stoichiometry of the material affects the electron properties of $Mg_2Si_{1-x}Sn_x$ solid solutions due to the formation of charged point defects [70]. This can be explained by mentioning that each Mg vacancy acts as a double-electron acceptor and on the other hand, each Mg interstitial as a double-electron donor, thus it is important to note that Mg content does indeed have a significant impact on the band structure of the material.

Inquiries in this matter [71, 72] showed how the Mg content affects the electrical properties of Sb-doped $Mg_2Si_{1-x}Sn_x$ (x = 0.4, 0.5) solid solutions. The excess of Mg (5-10 mol%) leads to an improvement of the electric concentration and the electrical conductivity by one order of magnitude and it is an increase that is registered over an entire range of temperatures (each interstitial Mg augments the carrier concentration with the two corresponding electrons added to the conduction band). However, as expected, this leads to a decrease of the Seebeck coefficient, but the degree in which the Mg content affects both properties (S and σ) is disproportional. Consequently, it is reported an improvement of the power factor with values as high as double than those corresponding to stoichiometric $Mg_2Si_{1-x}Sn_x$ solid solutions.

From the perspective of thermal properties, an intensification of phonon-point defect scattering with the addition of Mg (which would have resulted in a lower thermal conductivity) was expected. This, however, does not happen and, in the contrary, a certain increase of the thermal conductivity has been observed.

Nevertheless, the figure of merit is enhanced reaching values of ZT = 1.25 at 800 K for $Mg_{2.2}Si_{0.49}Sn_{0.5}Sb_{0.01}$, which was an enhancement of 60% than the stoichiometric $Mg_2Si_{0.49}Sn_{0.5}Sb_{0.01}$ obtained in the study [71]. It was also observed that the maximum of ZT can be adjusted to different temperatures with the addition of Mg (by pushing the starting point of intrinsic conduction to higher temperatures).

The case of Mg-deficient solid solutions has also been investigated [73] and what was reported is that the resulting Mg vacancies are not only hindering the electrical properties of $Mg_2Si_{1-x}Sn_x$, but also compensates the effect of Sb on the solid solutions and saturates the carrier concentration.

In conclusion, point defects that result from an over-stoichiometry of Mg have an unambiguous desirable effect on the TE properties of $Mg_2Si_{1-x}Sn_x$ solid solutions, leading to higher power factors and figures of merit.

1.3 Diffusion barriers for thermoelectric modules

As was earlier established, to make TE devices, n-type and p-type materials are joined electrically in series and thermally in parallel. The joining is done by using electrical (ohmic) contacts and the efficiency and reliability of TE device depends upon the metal contacts used. Given that the performance of the TE device is greatly influenced by its internal resistance, the power output being inversely proportional to the latter, the contribution of the metal contact to the total resistance needs to be minimized as much as possible. For example, the contact surface area between the TE material and the ohmic contact is an important factor, as an improper contact can lead to resistance to the flow of carriers, by reduction in the surface area between TE material and contact. These contact materials,

must be able to operate efficiently in the range of operation of the TE material too and to sustain the thermal cycles to which a TE device is subjected to during its operation without leading to fracturing.

The most significant expected characteristics of the metal contact in the development of TE modules are a good adhesion to the TE material (similar thermal expansion coefficients), low contact resistance and to have no reaction with the TE material.

Most of the work employed in solving these aspects in the domain of metallic contacts was done within the integrated circuit technology, where they represented constant challenges throughout the development of Si-based electronics.

For example, the most widely used materials as electrical contacts in the electronics industry is copper (Cu), due to its very low electrical resistance (the order of 10^{-8} Ω at ambient temperature), high electro/stress-migration resistance and high melting point [74] and aluminum (Al) for the same reasons (despite its higher electro-migration resistance which leads to lower lifetime [75]). However, despite promising electrical properties, both Al and Cu diffuse and react with Si, leading to the formation of corresponding alloys and ultimately to the degradation of the contacts performances. Therefore a diffusion barrier is necessary to separate the two materials. However, it is worth mentioning that in thermoelectrics, as opposed to integrated circuit technology, certain alloys are exploited for specific applications, such as AlSi with a Si content of 10% which is used as a brazing joint in this work.

The same has been observed for TE materials in the case of Cu deposition on Bi_2Te_3, the most commonly used TE material for ambient temperature applications, for which even at room temperature Cu diffuses in the bismuth telluride [76]. This leads to the formation of a Cu-Te alloy which reduces the TE performance of the material. Accordingly, a diffusion barrier is also needed to prevent this intermixing of the two materials.

In order for a diffusion barrier to be useful, it is required that is satisfies the following conditions [77]:

- The layer should constitute a kinetic barrier to the diffusion of both materials across it (the transport rate of substrate and electrical contact materials across the diffusion layer should be small).
- The barrier layer should be thermodynamically stable against the neighboring materials, so that its existence in their presence is preserved (or a small rate of loss of barrier material into the others).
- The barrier layer should well adhere to the two surrounding materials, to have a low contact resistivity with them, to have high electrical and thermal conductivities, to be resistant to thermal and mechanical stresses and to be laterally uniform in thickness and structure.

Usually, however, the lack of reactivity between the diffusion barrier and the adjacent layers can translate into a poor adhesion. Furthermore, the transport of atoms across the diffusion layer is dependent on the defects structure of the layer and specifically of its microstructure. In thin films, where extensive defects such as grain boundaries sometimes crossing the whole thickness of the film, atomic diffusion processes via defects entirely dominates the kinetics in the film [77], reducing the intrinsic effectiveness of the barrier material used. The atomic mobility is enhanced by the paths formed by the grain boundaries and extended defects [78]. This can also explain how atomic diffusion can, in some cases, occur even at room temperatures, regardless of the diffusion properties of the materials determined in bulk. Defects and grain boundaries are therefore significant in the search and characterization of diffusion barriers.

(i) Diffusion barriers for integrated circuit technology

Therefore, materials have been searched to act as valid diffusion barriers, predominantly in the development of integrated circuits. For example, to avoid the reaction of Cu with Si, materials based on Ti [79-81] and Ta [82-84] have been widely investigated and proved to show great promise. Using tantalum nitride, TaN, as an intermediate layer, led to good diffusion barrier properties due to its amorphous or nano-crystalline characteristics [85]. However, TaN only remains a barrier as long as the crystallization temperature is higher than the annealing temperature [83]. At high temperatures, after the crystallization of TaN, the emergence of the Cu-Si alloy indicates that the transition from amorphous structure to polycrystalline structure is responsible for the failure of the intermediate layer as a diffusion layer. On the other hand, the addition of a Ta layer to form a Ta/TaN bilayer led to amelioration, to a more stable diffusion barrier, even at temperatures slightly higher than the crystallization of the TaN layer. This is due to the enlargement of the diffusion path for Cu atoms through the bilayer than for individual layers of Ta or TaN, retarding the reaction between Cu and the underlying Si substrate.

The advantages brought by an amorphous structure and the importance of the microstructure are put forward by the results obtained on TiN [86] for systems with Al metallization. This material is an attractive barrier based on its chemical and thermodynamic stability, but the deposition of TiN layer on Si leads to the formation of a columnar grain structure. This was immediately followed by the failure of the diffusion barrier on account of the fast diffusion paths along the columnar grains at relatively high temperatures. A solution was found in this case, by once again adding another barrier, a Ti layer, which interrupts the columnar growth and reducing the open grain boundaries of the TiN layer. On the other hand, amorphous Ni-Ti layers as thin as 5 nm have been deposited on Si and were highly effective as diffusion barriers against Cu for high temperatures, but only as long as dewetting is avoided [87].

However, there have been cases in which a sacrificial layer is added in the system, which although it reacts with the neighboring layers, it forms a stable alloy which hinders further diffusion. This was observed while using Ta as a diffusion barrier against Cu atoms [82]. This resulted in the formation of $TaSi_2$ and Cu_3Si alloys which are in local equilibrium and therefore stopped further reactions to develop.

(ii) Diffusion barriers for TE applications

Diffusion barriers have also been investigated for TE applications (though at a lower degree than for integrated circuit technology), leading to the characterization and assessment of compatibility between various materials.

In the case of Bi_2Te_3-based bulk commercial TE devices, Ni has been widely employed as the barrier of choice [88]. However, despite being considered a negligible effect for Ni layers with a 3-5 μm thickness, it has been known that Ni diffuses in the TE material [89]. As possible replacements, diffusion barriers based on Au, Ag, TiN, TiW, Ta [90] and Co [89] have been additionally tested. Of these materials, the most promising results have been brought forward by Co, suffering no diffusion through the TE material and had lower impact on the degradation of its TE properties than Ni, which showed the formation of a Ni-Te alloy at the interface between layers [89]. Similar results have been obtained for Au and TiW, which were deposited for hindering diffusion of the Sn soldering into the Bi_2Te_3 thin films [90]. Although traces of Sn have been found in the TE material, the content was considered relatively low (6% and 11 %, respectively).

For $CoSb_3$-based TE modules, Au, Pt and Ti thin films (of 2.5 μm thickness) have been deposited by dc magnetron sputtering as diffusion barriers [91]. Of these, Pt proved to be the less effective due to poor adhesion to the TE material leading to its delamination. Au and Ti showed better adherence, but both have diffused in the $CoSb_3$ leg. The difference however is regarding the depth, which for Au was much larger (7 μm) than for Ti (0.32 μm). Additionally, the interface layer formed between the $CoSb_3$ and Ti originates from the difference in chemical potential between Co and Ti, leading to their mutual diffusion and to the formation of a stable compound that ultimately has little effect on the electrical properties of the system.

The effect of various metal contacts on the mechanical and electrical properties on TE modules based on higher manganese silicide (HMS) has been also examined [92]. This study included as metal contacts Co, Mo, Cr, Ti, Ni (chosen on grounds of cost and due to their large work functions), MnSi and $TiSi_2$, which were added during the sintering process to the HMS legs. The first four elemental materials have proved to form an alloy with Si after the latter diffused in the metal layers, which is brittle and has poor contact strength. The same has been observed for Ni, which diffuses in the HMS and forms a MnNiSi alloy. On the other hand, introducing Cr between Ni and HMS greatly reduced the diffusion for moderate temperatures. The best results have been obtained for the

compounds MnSi and $TiSi_2$, which led to sharp interfaces even at high temperatures (973 K) with no diffusion between the layers.

Lastly, the interfaces between Ni electrodes and Mg_2Si legs (prepared by plasma-activated sintering) by the addition of transition-metal silicides ($CoSi_2$, $CrSi_2$, $TiSi_2$ and NiSi) have been analyzed [93]. The objective was to reduce the electrical resistance of the contact between Ni and Mg_2Si. Individually, the metal silicides have proven to be improper as diffusion layers on account of the poor thermo-mechanical properties. These were determined by the emergence of cracks from the Mg_2Si-electrode interface, suggesting the existence of a residual thermal stress due to difference in thermal expansion coefficients. However, by mixing Ni with the metal silicides in a 50:50 in wt% ratio resulted in obvious improvements, stopping the formation of cracks and resulting in a good adhesion of the layers to the Mg_2Si legs (with the exception for $TiSi_2$). Furthermore, the electrical resistance of the contacts were decreased to such degree that values lower by 35% were obtained (for Ni/$CoSi_2$ mixture) and a corresponding 27% increase of power output.

Therefore, it was clearly concluded that diffusion barriers can lead to the improvement of the overall performance of the TE legs. However, the types of materials which are suitable to be used as diffusion barrier vary according to the system in which they are to be implemented. This means that diffusion barriers do not necessarily maintain their properties in their interaction with other materials and they need to be investigated for each case.

1.4 Objectives and structure of the thesis

In the present work, the investigation of the TE materials started from a design of a thin film-based TE module in which they were to be implemented. The TE module is meant to take advantage of the heat produced by the exhaust in automobiles and convert it into electricity with a sufficiently high electric power output for various onboard applications. As it can be seen in Figure 1.17.a, the proposed design of the module consists of a stack of alternating layers (rings) of n-type and p-type TE materials, separated by insulators, while connected by metallic electrodes. The hollow cylinder that is formed (Figure 1.17.b) would then be placed in the exhaust line where it would be subjected to a flow of hot gas reaching temperatures as high as 823 K. Cooling water would flow inside the hollow module, acting as heat sink and allowing to create a temperature gradient in the plane of layers, taking thus advantage of the in-plane TE properties of the thin films.

Therefore, the aim is to investigate p-type and n-type TE materials as thin films with sufficiently high figures of merit that may show promise in the development of the aforementioned TE module and to determine the feasibility of their integration along with insulators and metallic electrodes. To this end, the reactivity at the interfaces between the TE materials and the adjacent layers needs to be examined and be used as a key factor in the search for appropriate materials.

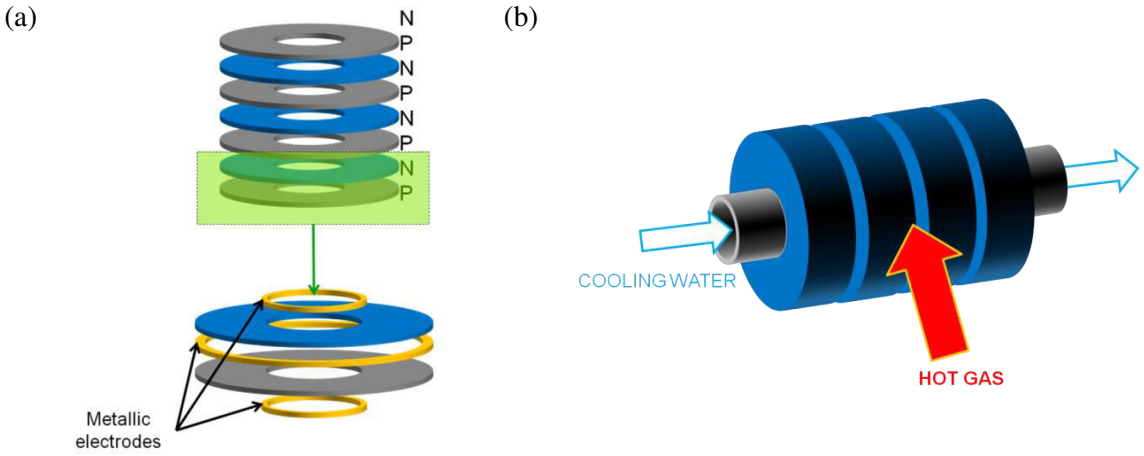

Figure 1.17. Design of proposed TE module (Valeo).

Another aspect that has to be kept in mind as well is the necessary thermal stability required from the materials that are to be used in TE applications. They need to show stability at the working temperatures in order to ensure a long lifetime of the module. Considering that atomic diffusion at the interfaces between contacts and TE materials can have a detrimental effect on the properties of the material at high temperatures, these are effects that also need to be considered during the investigation of the candidates.

For this reason, the thermoelectric properties and thermal stability of Mg_2Si and $Mg_2Si_{1-x}Sn_x$ solid solutions are investigated as thin films in the elaboration of a functioning and effective TE module. The films are deposited by plasma-assisted co-sputtering, taking advantage of the high control of the stoichiometry of this method.

Additionally, a second objective of this work is to investigate the path of depositing diffusion barrier layers on $Mg_2Si_{0.4}Ge_{0.6}Bi_{0.02}$ bulk TE legs which are subsequently connected to metallic electrodes (Al or Ni) through brazing (using a brazing joint of Al-Si alloy). The purpose is to ascertain which materials are appropriate to be used as diffusion barrier layers in order to optimize the thermo-mechanical and electrical properties of the interface between the TE legs and the metallic electrode, as well as its thermal and chemical stability, for the development of a TE module.

References

[1] D. M. Rowe, General Principles and Basic Considerations, in Thermoelectrics Handbook, CRC Press (2005) pp.1.

[2] R. Furlong, U.S. space missions using radioisotope power systems, Nuclear News, 42 (1999) 26.

[3] G. Gromov, Thermoelectric Cooling Modules, Global photonics applications & technology, (2002).

[4] http://mars.jpl.nasa.gov/mars2020/files/mep/MMRTG_FactSheet_update_10-2-13.pdf

[5] http://people.clarkson.edu/~bhelenbr/Research_Pages/Thermoelectrics.html

[6] http://www.biolitestove.com/products/biolite-campstove

[7] A. F. Ioffe, Semiconductor thermoelements, and Thermoelectric cooling, Infosearch London (1957).

[8] A. V. Dmitriev and I. P. Zvyagin, Current trends in the physics of thermoelectric materials, Physics-Uspekhi, 53 (2010) 789.

[9] K. F. Hsu, S. Loo, F. Guo, W. Chen, J. S. Dyck, C. Uher, T. Hogan, E. K. Polychroniadis, and M. G. Kanatzidis, Cubic $AgPb_mSbTe_{2+m}$: Bulk Thermoelectric Materials with High Figure of Merit, Science, 303 (2004) 818.

[10] R. Venkatasubramanian, E. Siivola, T. Colpitts, and B. O'Quinn, Thin-film thermoelectric devices with high room-temperature figures of merit, Nature, 413 (2001) 597.

[11] L.-D. Zhao, S.-H. Lo, Y. Zhang, H. Sun, G. Tan, C. Uher, C. Wolverton, V. P. Dravid, and M. G. Kanatzidis, Ultralow thermal conductivity and high thermoelectric figure of merit in SnSe crystals, Nature, 508 (2014) 373.

[12] T. C. Harman, M. P. Walsh, B. E. laforge, and G. W. Turner, Nanostructured thermoelectric materials, Journal of Electronic Materials, 34 (2005) L19.

[13] D. R. Brown, T. B. Stout, J. A. Dirks, and N. Fernandez, The Prospects of Alternatives to Vapor Compression Technology for Space Cooling and Food Refrigeration Applications, Energy Engineering, 109 (2012) 7.

[14] S. Godfrey, An introduction to thermoelectric coolers, Electronics Cooling Magazine, 2 (1996).

[15] J. Meseguer, I. Pérez-Grande, and A. Sanz-Andrés, Spacecraft Thermal Control, Woodhead Publishing (2012).

[16] P. Bellanger, Etude de l'influence des paramètres nano et microstructuraux sur les propriétés thermoélectriques des siliciures de magnésium $Mg_2(Si,Sn)$ de type-n Bordeaux, Ph.D thesis (2014)

[17] H. J. Goldsmid, Thermoelectric Properties of Metals and Semiconductors, in Introduction to Thermoelectricity, Springer Berlin Heidelberg (2010) pp.23.

[18] J. O. Sofo and G. D. Mahan, Optimum band gap of a thermoelectric material, Physical Review B, 49 (1994) 4565.

[19] P. Pichanusakorn and P. R. Bandaru, The optimal Seebeck coefficient for obtaining the maximum power factor in thermoelectrics, Applied Physics Letters, 94 (2009) 223108.

[20] Z.-G. Chen, G. Han, L. Yang, L. Cheng, and J. Zou, Nanostructured thermoelectric materials: Current research and future challenge, Progress in Natural Science: Materials International, 22 (2012) 535.

[21] G. J. Snyder and E. S. Toberer, Complex thermoelectric materials, Nature Materials, 7 (2008) 105.

[22] Y. Gelbstein, Z. Dashevsky, and M. P. Dariel, High performance n-type PbTe-based materials for thermoelectric applications, Physica B: Condensed Matter, 363 (2005) 196.

[23] A. Shakouri, Recent Developments in Semiconductor Thermoelectric Physics and Materials, Annual Review of Materials Research, 41 (2011) 399.

[24] T. M. Tritt, Thermoelectric Phenomena, Materials, and Applications, in Annual Review of Materials Research, (D. R. Clarke and P. Fratzl, eds.), Annual Reviews, Palo Alto (2011) pp.433.
[25] A. S. Glen, New Materials and Performance Limits for Thermoelectric Cooling, in CRC Handbook of Thermoelectrics, CRC Press (1995)
[26] B. C. Sales, D. Mandrus, B. C. Chakoumakos, V. Keppens, and J. R. Thompson, Filled skutterudite antimonides: Electron crystals and phonon glasses, Physical Review B, 56 (1997) 15081.
[27] H. Kleinke, New bulk Materials for Thermoelectric Power Generation: Clathrates and Complex Antimonides, Chemistry of Materials, 22 (2010) 604.
[28] L.-D. Zhao, V. P. Dravid, and M. G. Kanatzidis, The panoscopic approach to high performance thermoelectrics, Energy & Environmental Science, 7 (2014) 251.
[29] L. D. Chen, X. Y. Huang, M. Zhou, X. Shi, and W. B. Zhang, The high temperature thermoelectric performances of $Zr_{0.5}Hf_{0.5}Ni_{0.8}Pd_{0.2}Sn_{0.99}Sb_{0.01}$ alloy with nanophase inclusions, Journal of Applied Physics, 99 (2006) 064305.
[30] Laird Technologies, Thin film thermoelectric handbook, 2012
[31] G. J. Snyder, Thermoelectric Energy Harvesting, in Energy Harvesting Technologies, (S. Priya and D. Inman, eds.), Springer US (2009) pp.325.
[32] I. Chowdhury, R. Prasher, K. Lofgreen, G. Chrysler, S. Narasimhan, R. Mahajan, D. Koester, R. Alley, and R. Venkatasubramanian, On-chip cooling by superlattice-based thin-film thermoelectrics, Nature Nanotechnology, 4 (2009) 235.
[33] N.-W. Park, W.-Y. Lee, J.-E. Hong, T.-H. Park, S.-G. Yoon, H. Im, H. S. Kim, and S.-K. Lee, Effect of grain size on thermal transport in post-annealed antimony telluride thin films, Nanoscale Research Letters, 10 (2015) 20.
[34] J.-E. Hong, S.-K. Lee, and S.-G. Yoon, Enhanced thermoelectric properties of thermal treated Sb_2Te_3 thin films, Journal of Alloys and Compounds, 583 (2014) 111.
[35] H. Bottner, G. Chen, and R. Venkatasubramanian, Aspects of Thin-Film Superlattice Thermoelectric Materials, Devices and Applications, Mrs Bulletin, 31 (2006) 211.
[36] V. K. Zaitsev, M. I. Fedorov, E. A. Gurieva, I. S. Eremin, P. P. Konstantinov, A. Y. Samunin, and M. V. Vedernikov, Highly effective $Mg_2Si_{1-x}Sn_x$ thermoelectrics, Physical Review B, 74 (2006) 045207.
[37] K. Maex, M. van Rossum, INSPEC, and I. o. E. Engineers, Properties of Metal Silicides, INSPEC (1995).
[38] M. H. Jacobs, The structure of the metastable precipitates formed during ageing of an Al-Mg-Si alloy, Philosophical Magazine, 26 (1972) 1.
[39] V. K. Zaitsev, Thermoelectrics on the Base of Solid Solutions of Mg_2B^{IV} Compounds (B^{IV} = Si, Ge, Sn), in Thermoelectrics Handbook, CRC Press (2005) pp.29.
[40] T. Nemoto, T. Iida, J. Sato, T. Sakamoto, N. Hirayama, T. Nakajima, and Y. Takanashi, Development of an Mg_2Si Unileg Thermoelectric Module Using Durable Sb-Doped Mg_2Si Legs, Journal of Electronic Materials, 42 (2013) 2192.
[41] L. M. Zhang, C. B. Wang, H. Y. Jiang, and Q. Shen, Thermoelectric properties of Sb-doped Mg_2Si by solid state reaction, Thermoelectrics, 2003 Twenty-Second International Conference on - ICT, (2003) 146.
[42] J. Tani and H. Kido, Thermoelectric properties of Sb-doped Mg_2Si semiconductors, Intermetallics, 15 (2007) 1202.
[43] J. Y. Jung, K. H. Park, and I. H. Kim, Thermoelectric Properties of Sb-doped Mg_2Si Prepared by Solid-State Synthesis, IOP Conference Series: Materials Science and Engineering, 18 (2011) 142006.
[44] J. Tani and H. Kido, Thermoelectric properties of Bi-doped Mg_2Si semiconductors, Physica B: Condensed Matter, 364 (2005) 218.
[45] S.-M. Choi, K.-H. Kim, I.-H. Kim, S.-U. Kim, and W.-S. Seo, Thermoelectric properties of the Bi-doped Mg_2Si system, Current Applied Physics, 11 (2011) S388.
[46] X. Hu, D. Mayson, and M. R. Barnett, Synthesis of Mg_2Si for thermoelectric applications using magnesium alloy and spark plasma sintering, Journal of Alloys and Compounds, 589 (2014) 485.

[47] T. Sakamoto, T. Iida, S. Kurosaki, K. Yano, H. Taguchi, K. Nishio, and Y. Takanashi, Thermoelectric Behavior of Sb- and Al-Doped n-Type Mg_2Si Device Under Large Temperature Differences, Journal of Electronic Materials, 40 (2011) 629.
[48] T. Sakamoto, T. Iida, Y. Taguchi, S. Kurosaki, Y. Hayatsu, K. Nishio, Y. Kogo, and Y. Takanashi, Examination of a Thermally Viable Structure for an Unconventional Uni-Leg Mg_2Si Thermoelectric Power Generator, Journal of Electronic Materials, 41 (2012) 1429.
[49] W. Liu, X. J. Tan, K. Yin, H. J. Liu, X. F. Tang, J. Shi, Q. J. Zhang, and C. Uher, Convergence of Conduction Bands as a Means of Enhancing Thermoelectric Performance of n-Type $Mg_2Si_{1-x}Sn_x$ Solid Solutions, Physical Review Letters, 108 (2012) 166601.
[50] E. N. Nikitin, E. N. Tkalenko, V. K. Zaitsev, A. I. Zaslavskii, and A. K. Kuznetsov, A study of the phase diagram for the Mg_2Si-Mg_2Sn system and the properties of certain of its solid solutions, Journal of Inorganic Materials, 4 (1968) 1656.
[51] S. Muntyanu, E. B. Sokolov, and E. S. Makarov, Study of the Mg_2Sn-Mg_2Si system, Journal of Inorganic Materials, 2 (1966) 870.
[52] A. Kozlov, J. Gröbner, and R. Schmid-Fetzer, Phase formation in Mg–Sn–Si and Mg–Sn–Si–Ca alloys, Journal of Alloys and Compounds, 509 (2011) 3326.
[53] I. H. Jung, D. H. Kang, W. J. Park, N. J. Kim, and S. Ahn, Thermodynamic modeling of the Mg-Si-Sn system, Calphad-Computer Coupling of Phase Diagrams and Thermochemistry, 31 (2007) 192.
[54] M. Riffel and J. Schilz, Mechanically alloyed $Mg_2Si_{1-x}Sn_x$ solid solutions as thermoelectric materials, Thermoelectrics, 1996., Fifteenth International Conference on, (1996) 133.
[55] H. Gao, T. Zhu, X. Liu, L. Chen, and X. Zhao, Flux synthesis and thermoelectric properties of eco-friendly Sb-doped $Mg_2Si_{0.5}Sn_{0.5}$ solid solutions for energy harvesting, Journal of Materials Chemistry, 21 (2011) 5933.
[56] Y. Isoda, T. Nagai, H. Fujiu, Y. Imai, and Y. Shinohara, Thermoelectric properties of Sb-doped $Mg_2Si_{0.5}Sn_{0.5}$, ICT'06: XXV International Conference on Thermoelectrics, Proceedings, (2006) 406.
[57] W. Liu, X. F. Tang, and J. Sharp, Low-temperature solid state reaction synthesis and thermoelectric properties of high-performance and low-cost Sb-doped $Mg_2Si_{0.6}Sn_{0.4}$, Journal of Physics D: Applied Physics, 43 (2010) 085406.
[58] P. Gao, I. Berkun, R. Schmidt, M. Luzenski, X. Lu, P. Bordon Sarac, E. Case, and T. Hogan, Transport and Mechanical Properties of High-ZT Mg2.08Si0.4−x Sn0.6Sb x Thermoelectric Materials, Journal of Electronic Materials, 43 (2014) 1790.
[59] G. Bernard-Granger, C. Navone, J. Leforestier, M. Boidot, K. Romanjek, J. Carrete, and J. Simon, Microstructure investigations and thermoelectrical properties of an N-type magnesium–silicon–tin alloy sintered from a gas-phase atomized powder, Acta Materialia, 96 (2015) 437.
[60] W. Liu, Q. Zhang, X. F. Tang, H. Li, and J. Sharp, Thermoelectric Properties of Sb-Doped $Mg_2Si_{0.3}Sn_{0.7}$, Journal of Electronic Materials, 40 (2011) 1062.
[61] G. S. Nolas, D. Wang, and X. Lin, Synthesis and low temperature transport properties of $Mg_2Ge_{1-y}Sb_y$, Physica status solidi (RRL) – Rapid Research Letters, 1 (2007) 223.
[62] Q. Zhang, J. He, T. J. Zhu, S. N. Zhang, X. B. Zhao, and T. M. Tritt, High figures of merit and natural nanostructures in $Mg_2Si_{0.4}Sn_{0.6}$ based thermoelectric materials, Applied Physics Letters, 93 (2008) 102109.
[63] W. J. Luo, M. J. Yang, F. Chen, Q. Shen, H. Y. Jiang, and L. M. Zhang, Preparation and Thermoelectric Properties of Bi-Doped $Mg_2Si_{0.8}Sn_{0.2}$ Compound, Materials Transactions, 51 (2010) 288.
[64] Z. Du, T. Zhu, and X. Zhao, Enhanced thermoelectric properties of $Mg_2Si_{0.58}Sn_{0.42}$ compounds by Bi doping, Materials Letters, 66 (2012) 76.
[65] Q. Zhang, J. He, X. B. Zhao, S. N. Zhang, T. J. Zhu, H. Yin, and T. M. Tritt, In situ synthesis and thermoelectric properties of La-doped Mg_2(Si, Sn) composites, Journal of Physics D: Applied Physics, 41 (2008) 185103.
[66] H. Le-Quoc, S. Béchu, S. Populoh, A. Weidenkaff, and A. Lacoste, Thermoelectric properties of thin films of Sb doped $Mg_2Si_{1-x}Sn_x$ solid solutions, Journal of Alloys and Compounds, 546 (2013) 138.

[67] P. Wissmann and H.-U. Finzel, Electrical Resistivity of Thin Metal Films, Springer-Verlag Berlin Heidelberg (2007).
[68] Y. Isoda, S. Tada, T. Nagai, H. Fujiu, and Y. Shinohara, Thermoelectric Properties of p-Type $Mg_{2.00}Si_{0.25}Sn_{0.75}$ with Li and Ag Double Doping, Journal of Electronic Materials, 39 (2010) 1531.
[69] H. Le-Quoc, A. Lacoste, S. Béchu, A. Bès, D. Bourgault, and D. Fruchart, Deposition of thin films of $Mg_2Si_{1-x}Sn_x$ solid solution by plasma-assisted co-sputtering, Journal of Alloys and Compounds, 538 (2012) 73.
[70] W. Liu, X. F. Tang, H. Li, K. Yin, J. Sharp, X. Y. Zhou, and C. Uher, Enhanced thermoelectric properties of n-type $Mg_{2.16}(Si_{0.4}Sn_{0.6})_{(1-y)}Sb_y$ due to nano-sized Sn-rich precipitates and an optimized electron concentration, Journal of Materials Chemistry, 22 (2012) 13653.
[71] W. Liu, X. Tang, H. Li, J. Sharp, X. Zhou, and C. Uher, Optimized Thermoelectric Properties of Sb-Doped $Mg_{2(1+z)}Si_{0.5-y}Sn_{0.5}Sb_y$ through Adjustment of the Mg Content, Chemistry of Materials, 23 (2011) 5256.
[72] Z. Du, T. Zhu, Y. Chen, J. He, H. Gao, G. Jiang, T. M. Tritt, and X. Zhao, Roles of interstitial Mg in improving thermoelectric properties of Sb-doped $Mg_2Si_{0.4}Sn_{0.6}$ solid solutions, Journal of Materials Chemistry, 22 (2012) 6838.
[73] T. Dasgupta, C. Stiewe, R. Hassdorf, A. J. Zhou, L. Boettcher, and E. Mueller, Effect of vacancies on the thermoelectric properties of $Mg_2Si_{1-x}Sb_x$ ($0<x<0.1$), Physical Review B, 83 (2011) 235207.
[74] T. Nitta, T. Ohmi, M. Otsuki, T. Takewaki, and T. Shibata, Electrical Properties of Giant-Grain Copper Thin Films Formed by a Low Kinetic Energy Particle Process, Journal of the Electrochemical Society, 139 (1992) 922.
[75] J. Tao, N. W. Cheung, and H. Chenming, Characterization and modeling of electromigration failures in multilayered interconnects and barrier layer materials, Electron Devices, IEEE Transactions on, 43 (1996) 1819.
[76] B. M. Goltsman, V. A. Kudinov, and I. A. Smirnov, Semiconductors Thermoelectric Materials Based on Bi_2Te_3, (1972).
[77] M. A. Nicolet and M. Bartur, Diffusion barriers in layered contact structures, Journal of Vacuum Science & Technology, 19 (1981) 786.
[78] M. A. Nicolet, Diffusion barriers in thin films, Thin Solid Films, 52 (1978) 415.
[79] H. Joswig and W. Pamler, Stoichiometry effects in TiN diffusion barriers, Thin Solid Films, 221 (1992) 228.
[80] J. Y. Park, Comparison of TiN and TiN/Ti/TiN multilayer films for diffusion barrier applications, Journal of the Korean Physical Society, 35 (2003) 817.
[81] M. Fugger, M. Plappert, C. Schäffer, O. Humbel, H. Hutter, H. Danninger, and M. Nowottnick, Comparison of WTi and WTi(N) as diffusion barriers for Al and Cu metallization on Si with respect to thermal stability and diffusion behavior of Ti, Microelectronics Reliability, 54 (2014) 2487.
[82] T. Laurila, K. Zeng, J. K. Kivilahti, J. Molarius, and I. Suni, Chemical stability of Ta diffusion barrier between Cu and Si, Thin Solid Films, 373 (2000) 64.
[83] Q. Xie, X.-P. Qu, J.-J. Tan, Y.-L. Jiang, M. Zhou, T. Chen, and G.-P. Ru, Superior thermal stability of Ta/TaN bi-layer structure for copper metallization, Applied Surface Science, 253 (2006) 1666.
[84] W.-L. Wang, K.-T. Peng, H.-C. Kuo, M.-H. Yeh, H.-J. Chien, and T.-H. Ying, The contact resistance reduction of Cu interconnects by optimizing the crystal behavior of Ta/TaN diffusion barrier, Materials Science in Semiconductor Processing, 27 (2014) 860.
[85] M. Stavrev, D. Fischer, F. Praessler, C. Wenzel, and K. Drescher, Behavior of thin Ta-based films in the Cu/barrier/Si system, Journal of Vacuum Science & Technology A, 17 (1999) 993.
[86] W.-F. Wu, K.-C. Tsai, C.-G. Chao, J.-C. Chen, and K.-L. Ou, Novel multilayered Ti/TiN diffusion barrier for Al metallization, Journal of Electronic Materials, 34 (2005) 1150.

[87] B. T. Liu, L. Yang, X. H. Li, K. M. Wang, Z. Guo, J. H. Chen, M. Li, D. Y. Zhao, Q. X. Zhao, and X. Y. Zhang, Ultrathin amorphous Ni–Ti film as diffusion barrier for Cu interconnection, Applied Surface Science, 257 (2011) 2920.
[88] M. T. Terry, Electrical and Thermal Transport Measurement Techniques for Evaluation of the Figure-of-Merit of Bulk Thermoelectric Materials, in Thermoelectrics Handbook, CRC Press (2005) pp.23.
[89] W. H. Chao, Y. R. Chen, S. C. Tseng, P. H. Yang, R. J. Wu, and J. Y. Hwang, Enhanced thermoelectric properties of metal film on bismuth telluride-based materials, Thin Solid Films, 570, Part B (2014) 172.
[90] N.-H. Bae, S. Han, K. E. Lee, B. Kim, and S.-T. Kim, Diffusion at interfaces of micro thermoelectric devices, Current Applied Physics, 11 (2011) S40.
[91] B. Song, S. Lee, S. Cho, M.-J. Song, S.-M. Choi, W.-S. Seo, Y. Yoon, and W. Lee, The effects of diffusion barrier layers on the microstructural and electrical properties in $CoSb_3$ thermoelectric modules, Journal of Alloys and Compounds, 617 (2014) 160.
[92] X. Shi, Z. Zamanipour, J. Krasinski, A. Tree, and D. Vashaee, An Investigation of Electrical Contacts for Higher Manganese Silicide, Journal of Electronic Materials, 41 (2012) 2331.
[93] T. Sakamoto, T. Iida, Y. Honda, M. Tada, T. Sekiguchi, K. Nishio, Y. Kogo, and Y. Takanashi, The Use of Transition-Metal Silicides to Reduce the Contact Resistance Between the Electrode and Sintered n-Type Mg_2Si, Journal of Electronic Materials, 41 (2012) 1805.

Chapter 2. Experimental procedures

This chapter presents the set of experimental methods that have been used in the two topics of this work which are the synthesis and characterization of thermoelectric thin films and the search for efficient diffusion barriers for TE legs.

First, we will discuss the deposition method used for the synthesis of the thin films described in this study and the characterization techniques that were employed in the investigation of their structural and thermoelectric properties. The thin films were grown by physical vapor deposition (PVD), using microwave plasma-assisted co-sputtering in order to obtain stoichiometric materials. A short introduction on PVD is offered and the deposition equipment and process are described. For the investigation of the structural properties of thin films, x-ray diffraction techniques were employed (out-of-plane and grazing in-plane). The film microstructure was monitored by scanning electron microscope (SEM), while the chemical composition was determined by energy-dispersive x-ray spectroscopy (EDX). In regards to the thermoelectric properties of the thin films, four-point probes and van der Pauw methods were used to determine the electrical conductivity, the carrier concentration and the carrier mobility, while 3-ω method was made use to investigate the thermal conductivity. Additionally, the Seebeck coefficient was also ascertained by measuring the resulting voltages from the application of a temperature gradient.

Finally, the brazing process is described which is applied at an industrial scale by Valeo by using NOCOLOK® flux technology in a prototype furnace. This process is employed within the efforts of finding diffusion barrier layers that are to optimize the thermo-mechanical and electrical properties of the interface between the TE legs and the metallic electrode in the development of a TE module. The interfaces were subsequently investigated by SEM and EDX to determine their adherence to the TE legs and their chemical stability, while the electrical properties, specifically to determine the contact resistance, were measured by 4-point probe technique.

2.1 Thin films synthesis

2.1.1 Physical vapor deposition process

The synthesis of thin films via physical vapor deposition (PVD) process entails the vaporization of a solid material in a form of atoms or molecules, followed by their condensation to a surface. There are two possible methods used to generate atoms that are to be deposited: through pulverization or evaporation. In the first case, the atoms are ejected from the target material by bombarding it with energetic particles which commences a process called sputtering. The second method is accomplished through heat. Both are effective by supplementing enough energy to the surface of the target material for the atomic energy bonds to be broken.

The method used in this study for the formation of thin films is the sputtering process in which the atoms are physically ejected from the surface of the target material by momentum transfer from bombarding particles, which in this case are ions accelerated from an Ar-based plasma. The sputtered atoms are directed to a substrate on which it is intended for the deposition to take place and their energy evolution depends on the number of collisions between the time of pulverization and contact with the surface. This number is a function of pressure and distance between the target and the substrate. In low pressure plasma-assisted sputtering, the pressure inside the deposition chamber is around 1-5 mTorr (0.13-0.66 Pa) which may imply collisions between the Ar ions and the sputtered atoms depending on the mean free path of the latter. However, if the distance between the target and the substrate is maintained at a value lower than the mean free path, then the atoms will reach the substrate without losses in their energy.

By controlling the sputtering, transport and film growth processes, it is possible to control the composition and microstructure of the thin films in order to adjust the resulting material with the aimed properties.

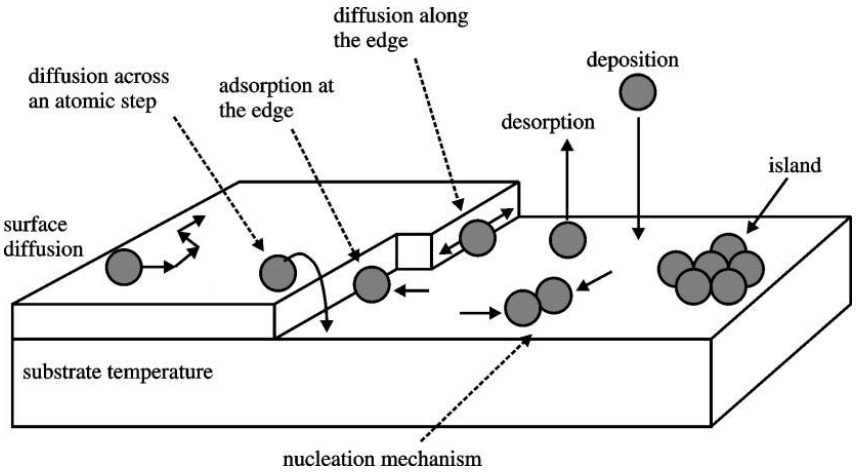

Figure 2.1. Schematic of adatoms behavior during deposition.

The thin film growth on a substrate is a process that depends on many factors, like the substrate temperature, the energy and flux of the incident atoms and the superficial interactions. The phenomena that are present during the growth of the thin films can be observed in Figure 2.1.

The growth of thin films is a non-equilibrium process based on the competition between kinetics and thermodynamics and it is accomplished mainly by nucleation. As incident atoms are impinging at the surface of the substrate, there are two distinct possibilities depending on the aforementioned factors. If the deposition parameters are such that the incident atoms have the required kinetic energy, they may be adsorbed at the surface and by diffusing randomly until encountering other adatoms, they lead to the formation of clusters (nuclei). However, if their energy is too high, the atoms will either completely reflect on the surface or they will temporarily diffuse across the surface of the substrate followed by the phenomenon called desorption in which the atoms are released once again. Once the nuclei are formed and stable, their size and density strongly depend on the deposition's parameters, like the deposition rate and substrate's temperature, which will also determine the dimensions of the resulting grains that will form the thin film. Keeping this in mind, the microstructure of the thin films, which greatly depends on the type of interactions between the adatoms and the surface and therefore their mobility at the surface, can be adjusted with a fine control over the temperature of the substrate, the pressure inside the deposition chamber and the energy of the incident atoms.

To this end, a most effective PVD method is the microwave assisted plasma co-sputtering that is used in this work considering the independent control of energy and flux of the particles (ions and atoms) focused on the targets and substrate due to the decoupling of plasma parameters (power supply, Ar pressure) and the bias voltages applied to each surface [1].

2.1.2 Microwave plasma-assisted co-sputtering method

This method consists of generating plasma inside the deposition chamber by using sources powered by microwaves situated on the walls of the chamber. The microwaves are transmitted from one end of a microwave applicator to the other where a magnetic dipole is placed. In the steady magnetic field, a resonance phenomenon takes place between the applied microwave frequency and the electron cyclotron frequency. Due to this cyclotron resonance, the electrons (supplied by Ar) rotate in phase with the circularly polarized wave, under a steady electric field over many such orbits. The result is the production of enough energy gain of the electrons in order to ionize the background gas [2] and create plasma (electrons and ions).

Using such plasma sources allows work at very low Ar pressures, 1-10 mTorr (0.13-1.33 Pa), and high ion densities (10^{11} cm^{-3}) which will ensure the generation and sustainment of plasma at relatively low values of microwave power (100-150 W per applicator). However these plasma sources

need to be matched before each deposition to ensure a maximum transmission of the microwave power through each microwave applicator and to avoid the reflected power that lead to their malfunction in time by overheat.

In Figure 2.2.a, a schematic of the deposition chamber is shown in which the plasma sources are circularly positioned in two rows around the chamber. The surfaces that are involved in the deposition process are positioned horizontally, facing each other, with the upper surface being the targets (depending on the configuration and aimed characteristics of the set-up, the number of targets can vary) and the lower one, the substrate. Both these surfaces are immersed in plasma and are individually biased during the process. The substrate will be subjected to an RF bias with the purpose of cleaning the surface of any contaminants and native oxides before the deposition. The choice of an RF power supply is motivated by the type of substrates that is often used for depositions (insulators). During the deposition, the targets are biased using a DC power supply that will lead to their bombardment with Ar ions from the plasma and commences the sputtering process (Figure 2.2.b). The mean energy (E_{mean}) of the resulting sputtered atoms is connected to the surface binding energy (U_s) of each material according to [3]:

$$E_{mean} = 2 \cdot U_s \cdot \left(\ln w + \frac{2}{w} - \frac{1}{2 \cdot w^2} - \frac{3}{2} \right) / \left(1 - \frac{1}{w} \right)^2 \qquad (2.1)$$

where $w = E_i/E_{th}$, the ratio between the ion energy (E_i) and the threshold energy of the material(E_{th}). By implementing equation (2.1) for determining the mean energy of the sputtered atoms, values that range between 10 and 30 eV have been calculated for the materials used in this work. For example, these values are much higher than those which are obtained by thin film deposition by evaporation, 0.2 eV [4].

The independent control over the bias voltages for surfaces and the microwave power supply for the generation of plasma is very significant. This decoupling allows the ionic flux between the targets and the substrate to be controlled by the power of the plasma sources, while the energy of the ions contributing to the sputtering process (and thus the sputtering rate) is regulated by the bias voltages for each target. This alone is a great advantage in the efforts of attaining thin films with defined stoichiometry.

However there are number of other advantages brought forward by this setup [5]. The use of different possible targets (metallic or isolators) leads to the deposition of complex compounds. Moreover, the deposition rate is increased due to the high density of plasma, but also controlled by the pressure inside the chamber and the bias voltages on the targets (affecting the sputtering rate).

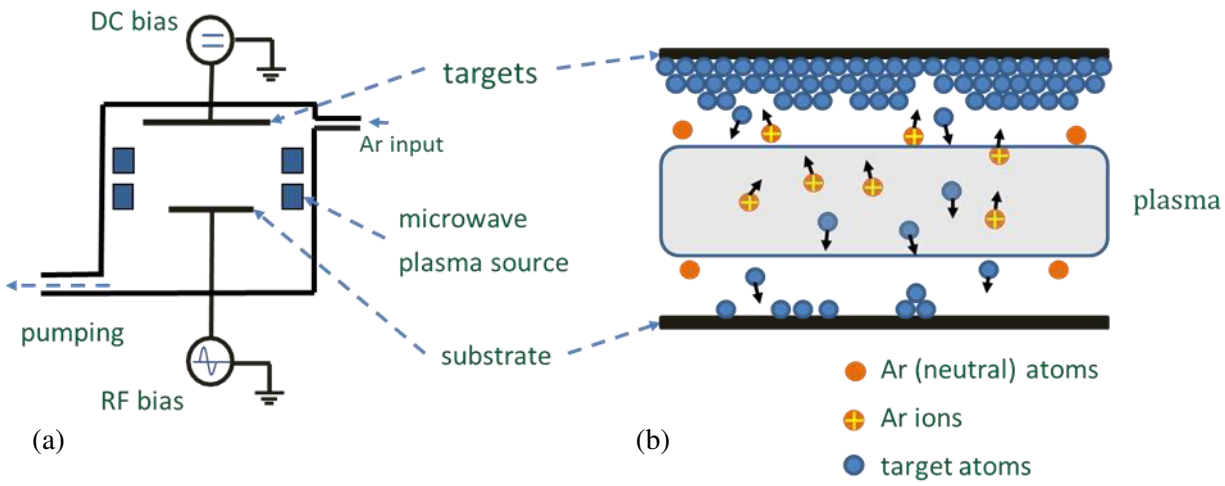

Figure 2.2. (a) Schematic of the deposition chamber, (b) Representation of the sputtering and deposition process.

The pressure inside the chamber regulates the energy loss of the sputtered atoms between the targets and the substrate, taking into account the mean free path (λ) of the sputtered atoms due to collisions with the background gas. The mean free path can be approximated using [6]:

$$\lambda = \frac{k_B \cdot T}{\pi \cdot \left(r_s + r_g\right)^2 \cdot p} \qquad (2.2)$$

where T and p are the temperature and pressure of the background gas, r_s and r_g are the atomic radii of the sputtered atoms and the background gas, respectively, while k_B is the Boltzmann constant. Using equation (2.2) for the approximation of the mean free paths of the materials used in this work for an Ar pressure of 1 mTorr, values between 11 and 20 cm were obtained. As it will later be shown, these values match closely or surpass the distance used during the deposition process, suggesting a process almost without sputtered atoms-gas collisions during deposition.

2.1.3 Deposition equipment

The setup that was assembled at the beginning of the present work is shown in Figure 2.3. The plasma is produced by the use of two microwave generators (magnetrons) each supplied by a 1.7 kW power generator diverted through 20 dipolar plasma sources arranged circularly around the deposition chamber in two rows. This redistribution of power is accomplished using power dividers.

The deposition chamber and the load-lock (used as exchange chamber, in order to maintain at all time the vacuum in the main chamber) are brought to very low pressures (10^{-7}-10^{-6} mbar) using rotational and turbo-molecular pumps, while the ulterior control of the pressure required for the deposition is done by using mass flow controllers that regulate the flow of Ar (and H during the

substrate cleaning). The working pressures for deposition are between 1 and 10 mTorr (0.13-1.33 Pa), due to the configuration of the plasma sources. Higher pressures cause the formation of plasma inside the microwave applicator and thus lead to the heating and metallization of the quartz windows (required for microwave transfer), disabling the plasma sources.

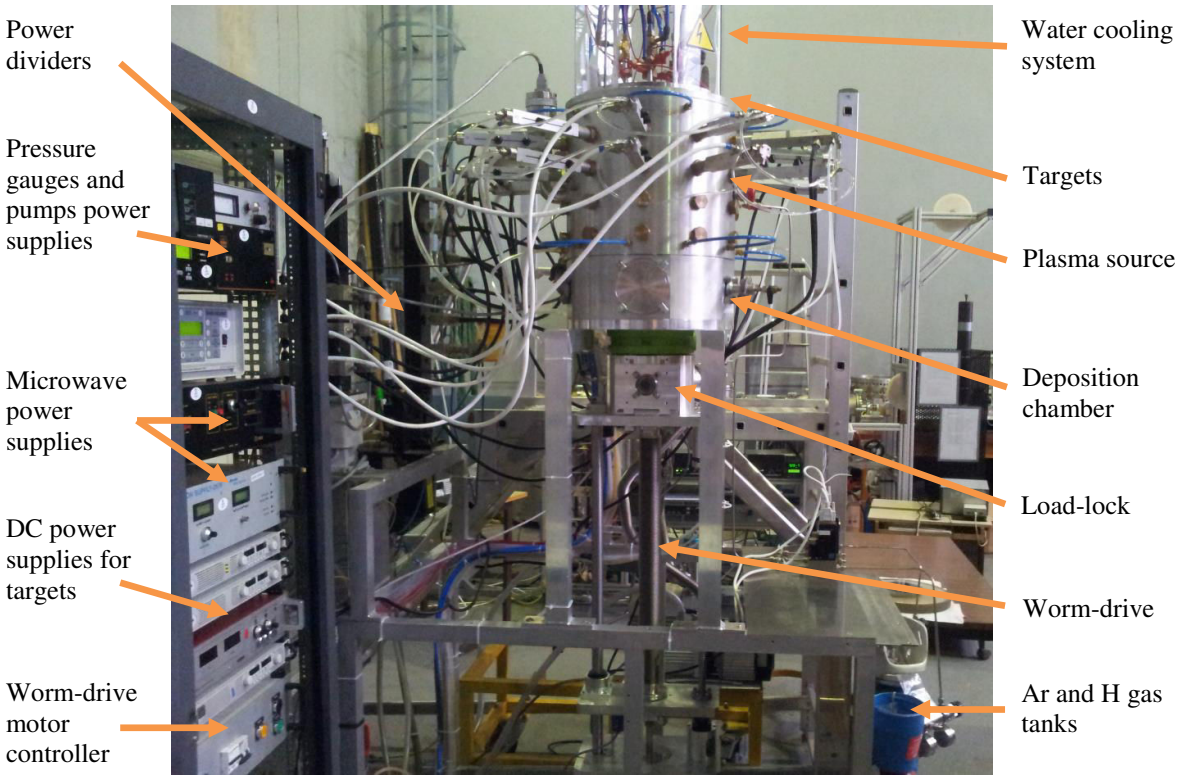

Figure 2.3. The microwave plasma-assisted co-sputtering setup.

As for the targets used in this work, they are arranged as shown in Figure 2.4. The dual co-sputtering of a type of material with the targets positioned diametrically opposed on the target holder ensure a homogeneous deposition of the each element on the substrate. As for the central position, this is kept for different dopants that will be used for obtaining n-type or p-type materials or for the deposition of certain diffusion layers.

Before depositions, the substrate is introduced inside the load-lock separated by the main deposition chamber through a valve that is opened and closed electronically. Through a worm-drive system, the sample holder is lifted inside the main chamber to the appropriate distance for deposition. Because of the positioning of the targets on the target holder and also their dimensions, the target-substrate distance is significant in the optimization of the deposition parameters. It determines the homogeneity in the distribution of the different type of atoms on the substrate.

For a good homogeneity the distance has to be high, but this would lead to a decrease of the deposition rate. This happens because of the increase in collisions between the sputtered and Ar atoms. Indeed, having the configuration of the targets shown in Figure 2.4, there is an angular distribution of

the flux of sputtered atoms from the targets, which means there is a distance that maximizes the flow of atoms towards the substrate. Considering the impact on the resulting film's microstructure, the distance has to be chosen in such way as to optimize both the deposition rate and the homogeneity at the level of the substrate. In previous research on similar deposition setup [5], it was established that the optimized distance (in terms of uniformity, deposition rate and resulting grain sizes in the order of tens of nanometers) is 12 cm, value which has been used as well in the work presented in this work.

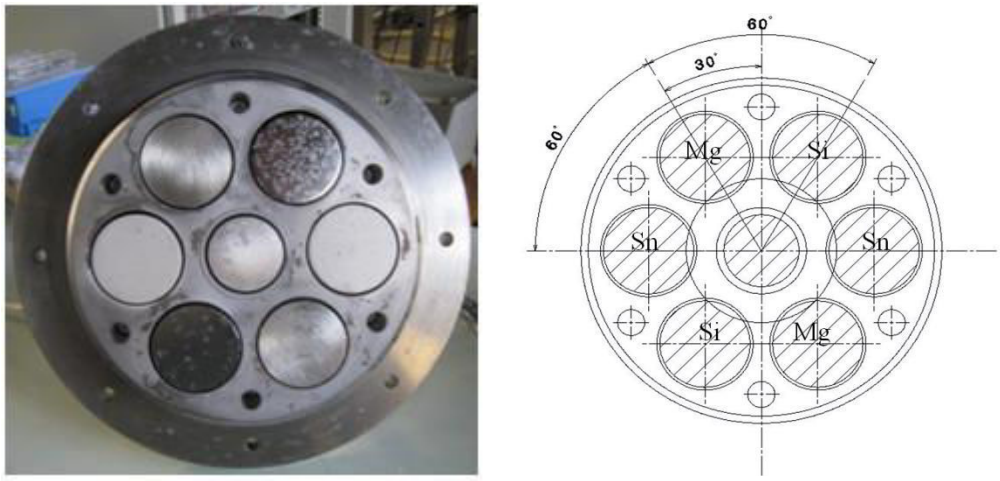

Figure 2.4. Position of the targets on the target holder.

To test the homogeneity of the deposition at this distance, Si was deposited for 2 h on a SiO_2/Si wafer with the diameter of 100 mm (covering the entire surface of the substrate holder). The cross section of the resulting Si film was investigated by SEM along the connecting line between the two Si targets in order to measure its thickness. The profile of the deposition is shown in Figure 2.5 where the center of the wafer is suggested by the null value of the distance (the negative and positive values are only reflecting the left-right symmetry with respect to the center).

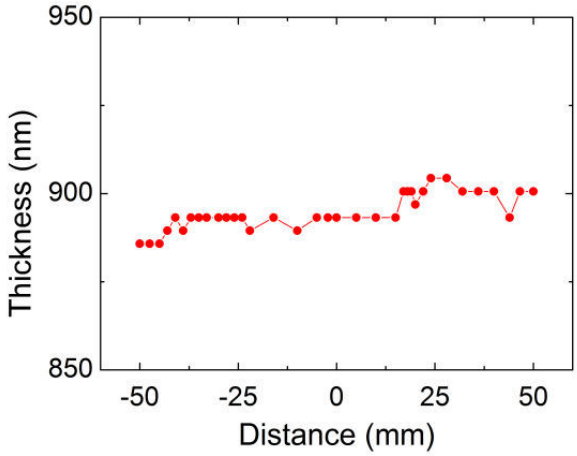

Figure 2.5. Si film thickness profile data across the distance of 100 mm.

The Si film has a relatively constant thickness across the entire diameter (considering the scale, the variations are small), indicating the uniform deposition with a relative standard deviation lower than 1% on the wafer and proving that the target-substrate distance is not low enough for the angular distribution of the sputtered atoms to pose a problem.

Furthermore, the calibration of the deposition process was necessary in order to obtain stoichiometric $Mg_2(Si,Sn)$ thin films. With a fixed Ar pressure of 1 mTorr (0.13 Pa), this was accomplished by varying the bias applied to each set of targets, until the aimed sputtering rate of the materials was achieved. For example, to obtain the $Mg_2Si_{0.4}Sn_{0.6}$ solid solution, it was found that the following set of bias values were to be used: 400 V (Mg targets), 420 V (Si targets) and 220 V (Sn targets), while the Mg_2Si thin films were deposited by applying a bias of 150 V to the Mg targets and 600 V to the Si targets. In the case of depositions of single element thin films, the maximum available bias of 600 V was used to obtain the highest deposition rate.

As substrates for the deposition of $Mg_2(Si,Sn)$ and Mg_2Si thin films, multiple materials were used depending on the requirements in terms of adherence and electrical properties (insulating or conductive substrates), namely SiO_2/Si, MgO, borosilicate glass and Ni substrates. The first were 0.5 mm-thick, bore-doped Si substrates with (100) orientation covered with a 500 nm-thick SiO_2 layer, acquired from Siltronix (polished on one side). The MgO substrates were supplied by CrysTec with a (100) orientation and thickness of 0.5 mm (also polished on one side). As borosilicate glass substrates, regular 1 mm-thick microscope slides were used, while 2 mm-thick polycrystalline Ni sheets were cut into pieces and used as substrates after being polished with silicon carbide paper and with a slurry of 1 µm in diameter suspended diamond particles.

For the investigation of diffusion barrier layers within the context of TE applications, 6×6×4 mm^3 Mg_2Si-based pellets were deposited on one side with various thin films. The pellets, prepared by spark plasma synthesis (SPS), were provided by Valeo and subsequently polished prior to the deposition. However, polishing this material results at times to inhomogeneity and roughness of the surface that do not match the planarity and quality of a 'model substrate', as it's reflected in Figure 2.6 where a deposition on a $Mg_2(Si,Ge)$ leg is compared with the deposition on a SiO_2/Si substrate.

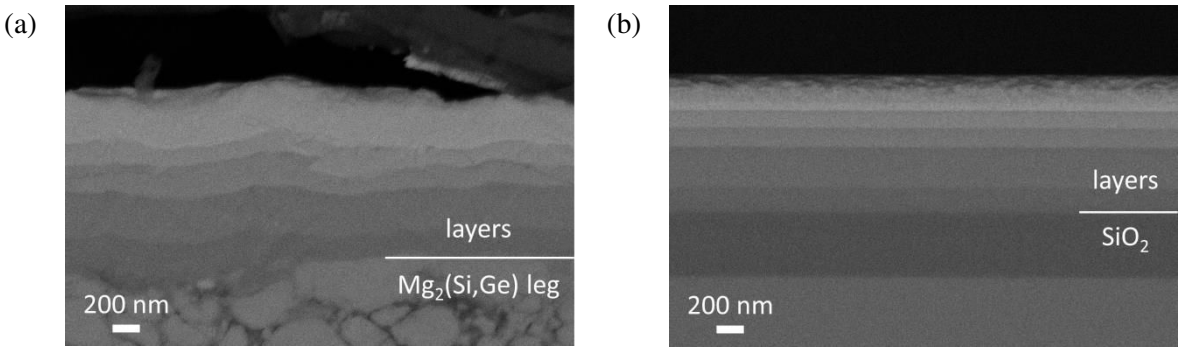

Figure 2.6. ESB-SEM cross-sectional images of deposited film on (a) Mg_2Si legs and (b) SiO_2/Si substrate.

The deposition process was performed on substrates that were kept either at room temperature (RT) or higher temperatures (HT). The substrate holder was maintained at RT by water cooling and heated by a graphite-based electrical resistor. The thermal transfer between the substrates and the substrate holder was done through a 2 mm-thick Cu disk whose contact with the neighboring surfaces was ensured by using silver lacquer. Due to difficulties of in-situ measurements of temperature during the deposition process, a calibration was needed previously. The calibration of the heating process was achieved by varying the current applied to the resistor, while the temperature of the substrate holder was determined with a thermocouple. To guarantee a more accurate measurement, the thermocouple was imbedded with silver lacquer in the center of a modified Cu disk, by pushing it sideways under the disk through a 1.5 mm deep trench, specifically cut to secure a level contact between the disk and the substrate holder, as is shown in Figure 2.7. During the calibration, the substrate holder was kept in the same conditions as the actual deposition (target-substrate distance, floating potential and plasma parameters, i.e. gas pressure and microwave power).

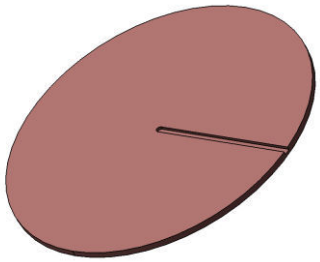

Figure 2.7. The bottom side of the Cu disk used during substrate temperature calibration, with trench visible for the placement of the thermocouple.

Additionally, a thermocouple was also attached under the substrate holder, which was used as a reference both during the calibration process and the following depositions. For example, in the case of a deposition temperature of 463 K, a current of 20 A was applied to the electrical resistor for 8 min, during which both thermocouples register an increase of temperature (more significant for the bottom thermocouple, considering it is connected to the surface closer to the resistor). After the current is cut-off, the bottom thermocouple indicates the under-side of the substrate holder leveling at an equilibrium temperature, while the upper thermocouple registers the increase of temperature at the surface of substrate on account of it being heated by the plasma. Finally, once the sputtering is initiated, the temperature of the substrate reaches equilibrium roughly at about 463 K. In Figure 2.8, it is shown that after the current cut-off and sputtering, the surface of the substrate holder was kept in plasma for 30 min. However, during the actual deposition, this time was increased to 1 h to allow better stabilization of the temperature. Also there was a small increase in temperature (10 K) after the sputtering process was initiated, showing the thermal impact on the substrate of the sputtered atoms.

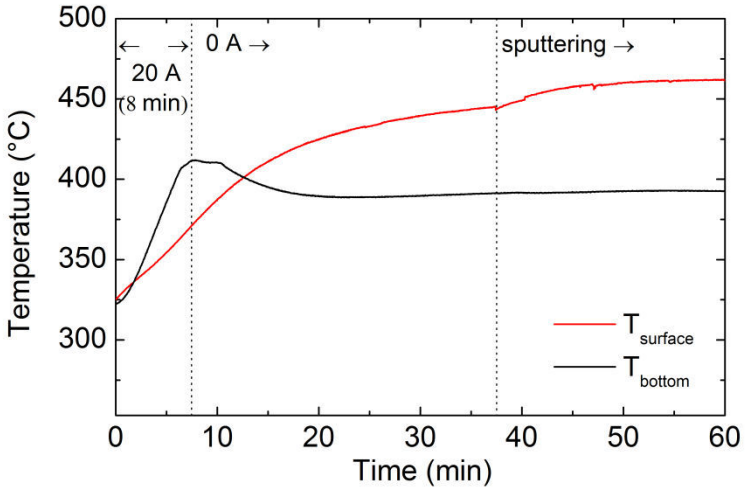

Figure 2.8. Temperature measurements with thermocouples during the heating of the substrate up to 463 K.

Moreover, before each deposition, the substrates were cleaned and this is accomplished through their consecutive immersion in acetone and ethanol in an ultrasonic bath for 5 min in each and then dried out using nitrogen flow. The substrate was further subjected to a physical and chemical cleaning process in Ar/H_2 plasma, by applying to the substrate holder an RF negative self-bias potential (V_0) of 30 V for 5-10 min. Taking into account the plasma potential, the cleaning is therefore done through the bombardment of Ar ions with the energy of $e\cdot(V_p-V_0)$ and reactive species of hydrogen.

The cleaning of the targets is also performed before the deposition in order to remove all the impurities or native oxide layers formed at their surface between processes. This is done in solely Ar-based plasma by applying to each set of targets the dc bias which is also to be used for the actual deposition, for at least 10 min.

For the formation of plasma, the Ar gas pressure was selected to be 1 mTorr (0.13 Pa) and the total microwave power of 1.7 kW (distributed through a divider guide to all 20 plasma sources). These parameters and the target-substrate distance kept at 12 cm ensure a deposition rate of ~2 μm/h. Electrically, the substrate holder was maintained at floating potential ($V_f \approx 10$ V) which can be considered, at a certain degree, an ion assisted deposition with ions with an energy of $e\cdot(V_p-V_f)$, where V_p is the plasma potential.

2.2 Structural and chemical characterizations

2.2.1 Scanning electron microscope (SEM)

The scanning electron microscope (SEM) is based on the thermal emission of a beam of electrons that is scanned over the sample surface and the detected signals are correlated to its position.

Among the detectable signals generated by the interaction between the electron beam and the surface, those originating from the secondary and backscattered electrons are suitable for surface analysis. Secondary electrons are ejected from the specimen due to inelastic scattering with the incident electrons. They typically have low energy and can only be emitted from the first few nanometers of the sample surface (Figure 2.9). Therefore, topographical information of the sample surface can be gathered by using the secondary electron (SE) detector. Backscattered electrons occur via elastic scattering and the detected electrons can originate from a larger volume within the sample due to their substantially higher energy. Since the intensity of the backscattered electrons is related to the atomic number, the resulting SEM image can give element-specific contrast. Accordingly, qualitative information about the variation in composition can be acquired by using the energy selective backscattered (EsB) detector. The resolution of the SEM is not only determined by the spot size of the electron beam, but rather by the interaction volume where the signal originates from. Nevertheless, high resolutions can be obtained (~10 nm).

Therefore, SEM is effective in observing the microstructure of the deposited thin film and also their thickness by analyzing the profiles of the samples. A Zeiss Ultra+ Field Emission Scanning Electron Microscope was used in this study. The morphology of the films' cross section was characterized at EHT voltage levels of 3 kV after the samples were either cleaved (depositions on SiO_2/Si and MgO substrates), cut (depositions on glass substrates) or polished (depositions on Ni substrates or TE legs).

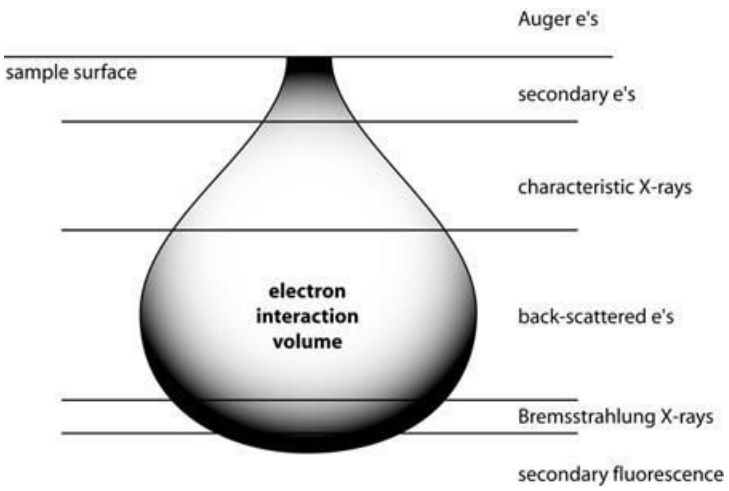

Figure 2.9. Diagram illustrating the depths at which various electron-sample interactions occur.

2.2.2 Energy dispersive x-ray spectroscopy (EDX)

Energy dispersive x-ray spectroscopy (EDX) is a qualitative and quantitative x-ray microanalytical technique that can provide information on the chemical composition of a sample for elements with atomic number $Z > 3$. An energy dispersive detector is usually incorporated in a scanning electron microscope. When the sample is bombarded by the SEM's electron beam, as

mentioned before, electrons are ejected from the atoms comprising the sample's surface. The resulting electron vacancies are filled by electrons from a higher state, and an x-ray is emitted to balance the energy difference between the two electrons states. The x-ray energy is characteristic of the element from which it was emitted.

An important aspect in the microanalysis of thin films is the energy of the electron beam. Because the interaction volume inside the sample (and therefore the depth) depends on the electron beam energy, it is important to choose a value of this energy that corresponds to a depth of interaction lower than the thickness of the thin film. Otherwise the resulting characteristic x-rays will include the signal from the substrate used in the process of deposition and lead to incorrect measurements of the composition.

In this study, a Bruker silicon drift detector EDX microanalyzer was used to determine the stoichiometry of the films and to create images with composition contrast in the investigation of the interfaces between layers, but also to map the cross sections of the films for compositional contrast. Additionally, for quantitative measurements of the composition, the system was calibrated using appropriate standards in order to reach errors lower than 1 wt% (value inherent to calibrated measurements). The measurements were performed at EHT level of 10 kV, which was appropriate for thin films with a thickness ranging between 2 µm and 4 µm. Higher accelerating voltages would have extracted information from the substrate due to the increase of the interaction volume between the electron beam and the materials. For the detection and quantification of the elements in the thin films, the characteristic x-ray energy corresponding to each component has been investigated (predominantly Kα lines for Mg and Si, Lα for Sn and Sb).

2.2.3 X-ray diffraction (XRD)

X-ray diffraction is non-destructive characterization technique which provides structural information. It is widely used for phase identification and quantification of crystalline materials and, additionally, it allows determining the degree of crystallinity, the size of the crystallites, the texture of the material and also the strains of the lattice.

An incident x-ray beam is directed towards the sample and penetrates the material where it can be partially reflected by the lattice planes. The Bragg condition is fulfilled when constructive interference occurs:

$$n\lambda = 2d_{hkl}sin\theta \qquad (2.3)$$

where n indicates the diffraction order, λ is the wavelength of the x-ray beam, d_{hkl} is the distance between the lattice planes (or interplanar d-spacings) and θ is the diffraction angle between the incident beam and the surface of the sample.

(i) In-plane XRD measurements

If the incident angle is large, then it is an out-of-plane measurement where the incident x-rays will penetrate deep inside a sample and the crystal lattice planes parallel to the surface are investigated according to the regular θ-2θ geometry (Figure 2.10.a). For thin films it is recommended to use the grazing incidence x-ray diffraction (GIXRD), in order to control the penetration depth of the x-rays (as the incident beam is travelling across a larger distance inside the film) so that the contribution of the substrate to the diffraction pattern will be minimized and the peaks of the thin films intensified.

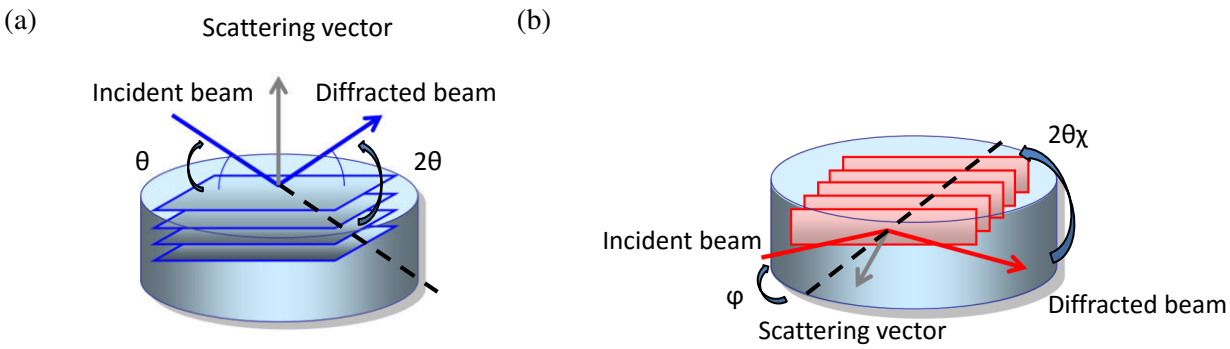

Figure 2.10. Geometries of (a) out-of-plane and (b) in-plane XRD measurements [7].

Additional to regular out-of-plane measurements, in-plane XRD is also used for measuring diffraction intensities from the crystal lattice planes normal to the surface of a sample (Figure 2.10.b). In this case, the incident angle of the x-rays is controlled independently to the sample rotation angle (φ) and the position of the detector (2θχ). This kind of a measurement is used as a non-destructive structure-depth analysis of a thin film, but it can also be particularly useful for crystalline structure validation in textured thin films.

(ii) Pole figure measurements

The previous two configurations can be usually used with a certain facility to estimate the presence of texturing inside a thin film by comparing the integrated intensities in the diffraction patterns with the peaks found in a data base for powders. However, to further characterize the structure of thin films and, most importantly, their texture, pole figure measurements can be performed. This technique (Figure 2.11.a) implies keeping fixed the diffraction angle (2θ) and collecting the diffraction intensity by changing two geometrical parameters: the tilt angle from sample surface normal direction (α, but it can also appear in literature as χ or Ψ) and the rotation angle around sample surface normal direction (β). The resulting diffraction intensity is plotted as a function of both α and β (Figure 2.11.b). The center of the pole figure is defined as $\alpha = 0°$, while the outer ring is at $\alpha = 90°$. In other words, the lattice plane normal is parallel to the sample surface normal for $\alpha = 0°$ and perpendicular for $\alpha = 90°$.

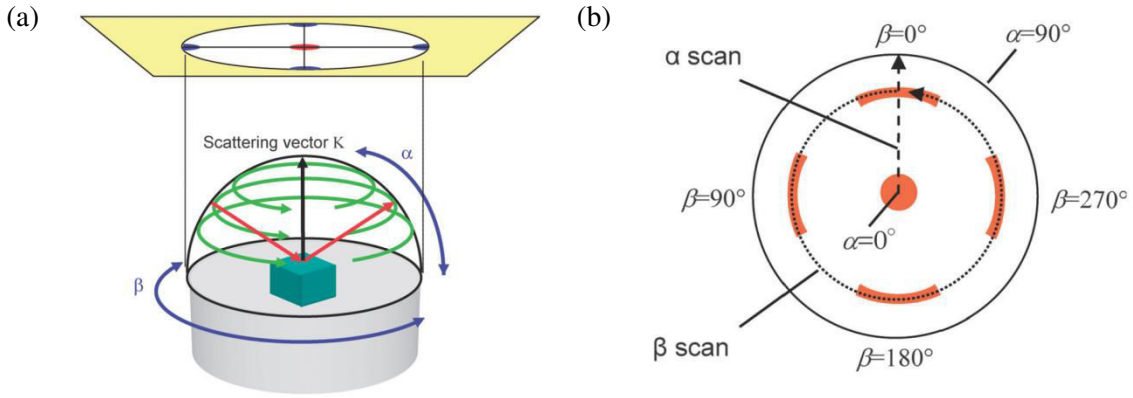

Figure 2.11. Representation of (a) pole figure measurement and (b) geometric parameters, α and β [8].

The resulting image is a stereographic projection of the crystallographic directions present in the grains of the investigated sample. This offers information on the preferential orientation of the grains and can also be used in the overall investigation of stresses and strains within the material.

(iii) Stress determination

To determine the stresses inside the thin films, the $\sin^2\Psi$ technique was used in this work. In this technique, the strains are determined from the diffraction patterns obtained for various tilt angles Ψ. The strains are considered in terms of inter-planar distances and are used to evaluate the stresses, σ_s, using the following expression [9]:

$$\sigma_s = \frac{E}{1+\upsilon} \cdot \frac{(d_\Psi - d_0)/d_0}{sin^2\Psi} \qquad (2.4)$$

where E and υ are the Young's modulus and the Poisson's ratio, respectively, of Mg_2Si, while d_Ψ is the inter-planar distance determined for the film positioned at a tilt angle Ψ, which is compared to the unstrained inter-planar distance d_0. This equation can be used to calculate the stresses in any direction exclusively from the inter-planar distanced obtained from at least two measurements.

The diffractometers used throughout this work for the out-of-plane measurements are based on diffraction in reflection mode with Bragg-Brentano θ-2θ geometry, an angular resolution of 0.2° and wavelengths of 1.54 Å (Gonio4 Philips) and 1.79 Å (D5000 Bruker). The in-plane measurements were performed with SmartLab Rigaku diffractometer (λ = 1.54 Å) and the pole figures were formed based on measurements with D8 Bruker diffractometer (λ = 1.54 Å) and reproduced by MTEX simulations (using 117.3 MPa and 0.184 as values for the Young modulus and Poisson's ratio, respectively, of Mg_2Si). The measurements of texture and strains were performed in collaboration with Mathieu Salaun from Néel Institute, Grenoble.

2.3 Thermoelectric properties measurements

2.3.1 Four-point probe measurement

The most common way of measuring the resistivity of a semiconductor thin film is by using a four-point probe. This technique involves bringing 4 equally spaced probes in contact with the film, as shown in Figure 2.12.

The advantage of using this method instead of the usual two-point probe configuration is the elimination of the errors in the measurement brought by the resistance of the contact between the probes and the sample as well as additional resistances due to probe wires.

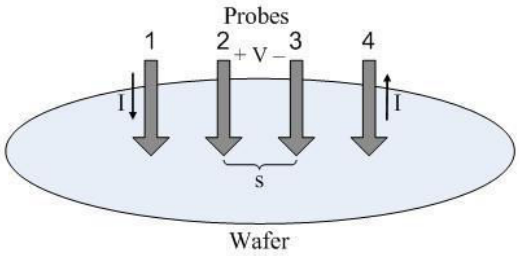

Figure 2.12. Four-point probe configuration.

As shown in Figure 2.12, the two outer probes are used for sourcing current (I) and the two inner probes are used for measuring the resulting voltage drop (V) across the surface of the sample. The ratio V/I is proportional with the resistivity (ρ) of the material according to the relation:

$$\rho = 2\pi s F \frac{V}{I} \qquad (2.5)$$

where s is the distance between each probe and F is a correction factor that takes into account the probe location near sample edges, sample thickness, sample diameter, probe placement and sample temperature [10]. The correction parameter can be established by examining appropriate tables.

An important issue that has to be kept in mind during resistivity measurements done on thin films is the possible contribution of the substrate to the overall signal. Accordingly, to avoid the flow of the current outside the thin film, it's best to use electrically non-conductive substrates (such as SiO_2). In-plane resistivity measurements were performed with a non-commercial setup implemented by Pole Automatisation at Néel Institute, with the samples kept under helium atmosphere during the experiment in the temperature range of 300-700 K, with a heating/cooling rate of 10 K/min.

2.3.2 Van der Pauw method and Hall coefficient measurements

The electrical resistivity can also be determined by using the van der Pauw method, which has the additional benefit of offering the means to measure the Hall coefficient, giving further information

on the transport properties of the investigated materials (carrier concentration, carrier mobility). The main advantage of the method is that it does not impose as many restrictions as other methods on the geometry of the sample, so it can be arbitrarily shaped as long as it is two-dimensional (which makes it suitable for thin films).

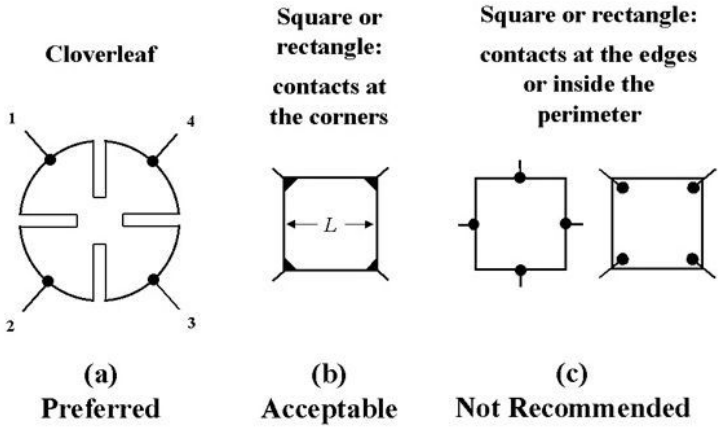

Figure 2.13. Sample geometries during use of Van der Pauw method [11].

The four contacts which are made during the measurement need to be placed on the outer edges of the sample, preferably not inside the perimeter, as it is seen in Figure 2.13. The voltages are measured between two contacts, while current is applied between the other two. For example, if a current is injected in contact 1 and extracted at contact 2 (current I_{12}), then the voltage is measured between contacts 4 and 3 ($V_{43} = V_4 - V_3$). By reversing the direction of the current between contacts 1 and 2 (I_{21}), then voltage V_{34} is obtained between the other two contacts. The resulting resistances defined as:

$$R_{12,43} = \frac{V_{43}}{I_{12}} \qquad \text{and} \quad R_{21,34} = \frac{V_{34}}{I_{21}} \tag{2.6}$$

which should have equal values. The rest of resistances are measured in the same way with a total of 8 values ($R_{12,34}$, $R_{21,43}$, $R_{23,14}$, $R_{32,41}$, $R_{34,21}$, $R_{43,12}$, $R_{41,32}$ and $R_{14,23}$) ultimately obtained for every possible combination between the currents applied between two contacts and the voltages measured between the other two. It may seem unnecessary to make 8 measurements considering the equality between every two pairs, however it is a revealing indicator on the repeatability of the measurements and the ohmic contact quality.

Following the aforementioned measurements, the electrical resistivity (ρ) can be determined from the van der Pauw equation [12]:

$$e^{-\pi \cdot \frac{d}{\rho} \cdot R_a} + e^{-\pi \cdot \frac{d}{\rho} \cdot R_b} = 1 \tag{2.7}$$

where d is the thickness of the sample/film and R_a and R_b are two characteristic resistances defined as following:

$$R_a = \frac{R_{12,43} + R_{21,34} + R_{34,21} + R_{43,12}}{4}, \quad R_b = \frac{R_{23,14} + R_{32,41} + R_{41,32} + R_{14,23}}{4} \qquad (2.8)$$

Other transport properties characterizing a material, e.g. carrier concentration and carrier mobility, can be determined from Hall-effect measurements. The Hall effect is the manifestation of the Lorentz force which is the combination of the electric force and magnetic force that act upon charge carriers. If the charge carrier are moving along the direction of the electric field that is perpendicular to an applied magnetic field, it experiences a magnetic force acting normal to both directions. This leads to formation of a transverse voltage difference V_H (Hall voltage):

$$V_H = \frac{I \cdot B}{q \cdot d \cdot n} \qquad (2.9)$$

where I is the current, B is the applied magnetic field, q is the charge, d is the sample thickness and n is the charge carrier concentration of the sample.

Experimentally, certain error sources (non-symmetric contact placement, sample shape) are overcome by acquiring Hall voltage measurements for positive and negative magnetic field direction. On the same principle as previously, assuming a current is injected in contact 2 and extracted at contact 4 (current I_{24}) and a positive magnetic field B (applied in the positive z direction), the Hall voltage between contacts 1 and 3 is determined (V_{13P}). Finally, a set of eight measurements is obtained: V_{13P}, V_{24P}, V_{31P}, V_{42P}, V_{13N}, V_{24N}, V_{31N} and V_{42N} (where N is an indication of magnetic field reversal). These values are used to determine the overall Hall voltage:

$$V_H = \frac{V_{13P} - V_{13N} + V_{24P} - V_{24N} + V_{31P} - V_{31N} + V_{42P} - V_{42N}}{8} \qquad (2.10)$$

whose polarity indicates the type of material (positive if p-type and negative if n-type).

Once the electrical resistivity and the charge carrier concentration are determined from equations (2.7) and (2.9), respectively, the carrier mobility, μ, can also be calculated:

$$\mu = \frac{1}{q \cdot n \cdot \rho} \qquad (2.11)$$

For all measurements in this work using the van der Pauw technique, a non-commercial set-up was used from IMEP-LAHC, Grenoble. The sample, with a size of 1×1 cm^2, were connected to the four electrical leads by direct contact through pressure according to the geometry shown in Figure 2.13.b and the transport properties were determined after applying a current between 10^{-4} A and 10^{-3} A and a 0.5 T magnetic field.

2.3.3 Seebeck coefficient measurements

The measurement of Seebeck coefficient of a thermoelectric thin film can be performed by measuring the difference of electrical potential in the plane of the film when it is subjected to a temperature gradient:

$$\alpha = -\frac{\Delta V}{\Delta T} = -\frac{V_{hot} - V_{cold}}{T_{hot} - T_{cold}} \qquad (2.12)$$

where the sign of α depends on the type of the majority charge carriers inside the investigated material: it's negative for n-type semiconductor and positive for p-type semiconductor.

It involves the measurement of the electrical potential difference between the sides of the sample where a temperature gradient of about 10 K has been induced. In such measurements, it is important to make good electrical and thermal contacts between the sample and the measuring device.

In this study, the Seebeck coefficient was measured at room temperature with a non-commercial device (Figure 2.14) implemented by Daniel Bourgault at Néel Institute, with an estimated accuracy of 5% [13].

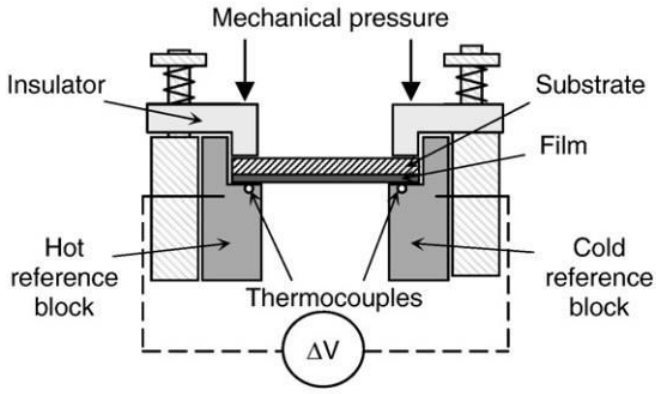

Figure 2.14. Schematic of experimental set-up for measuring the Seebeck coefficient [13].

A temperature gradient (measured by two K-type thermocouples) was applied along the plane of the film ensured by a heating cartridge, while the electrical and thermal contacts were done by mechanical pressure applied to the surface of the sample at the hot and cold ends of the set-up.

2.3.4 Thermal conductivity measurements

The investigation of thermal conductivities for thin films investigation is relatively troublesome due to different theoretical models that have to be employed while taking into account the interface between the thin film and the substrate, the thermal anisotropy or the heat dissipation by

convection, conduction and radiation. Also there are technical difficulties in conceiving the appropriate setup that can deal with materials at such low scale.

Nevertheless, there are two types of methods to determine the thermal conductivity, based on the dependency of the applied heating source over time: transient and steady-state. The transient method is used to determine the thermal conductivity based on measurement of the thermal diffusivity, while the steady-state method allows a direct assessment. The most widely used techniques are 3-ω (transient) and Völklein (steady-state) methods [14, 15].

The 3-ω method helps calculating the thermal conductivity by measuring the temperature response of the thin film to a transducer (metal strip) deposited on its surface (Figure 2.15). The basic principle is that a sinusoidal current of angular frequency ω heats the sample through Joule effect. The heating leads to a temperature oscillation, ΔT, with frequency 2ω. Keeping in mind that the resistance of the transducer (which also acts as a thermometer) is a function of temperature, a voltage oscillation at 3ω is observed and measured. Additionally, in order to determine the thermal conductivity of thin films, a differential measurement is required, with a reference system which is identical with the original sample except the presence of the deposited thin film. This means that the thermal conductivity of the thin films is determined by subtracting the value obtained for the substrate from that obtained after the measurement of the whole system (substrate and thin film).

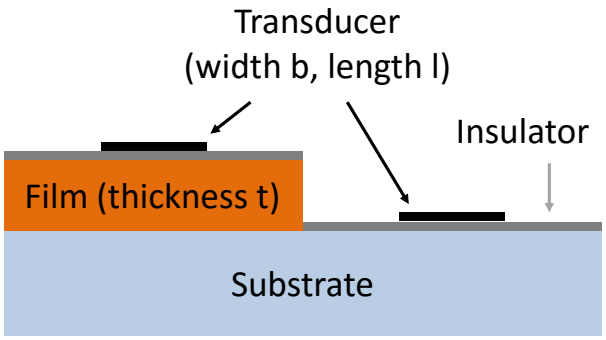

Figure 2.15. Schematic for the measurement of thermal conductivity using 3-ω method.

The thermal conductivity of the substrate, κ_0, is determined by [16]:

$$\kappa_0 = -\frac{1}{2 \cdot \pi \cdot l} \cdot \left[\frac{d\left(\frac{\Delta T}{P_l}\right)}{d ln\omega} \right]^{-1} \quad (2.13)$$

where l is the distance between the voltage leads, $\frac{d\left(\frac{\Delta T}{P_l}\right)}{d ln\omega}$ is the slope of a linear fit of the curve $\frac{\Delta T}{P_l}$ as a function of lnω at low frequencies, with P_l being the linear heat dissipation power.

The thin film deposited on the substrate is considered as a thermal barrier resistance, R, for the heat flux, bringing a shift in the temperature oscillation which, if normalized to the dissipated heat power, can be determined with the delta parameter:

$$\Delta\left(\frac{\Delta T}{P_l}\right) = \frac{R}{2 \cdot b \cdot l} \tag{2.14}$$

where b is the width of the transducer. This can be used to find the thermal conductivity κ of the thin film, having thickness t, using:

$$\kappa = \frac{t}{\Delta\left(\frac{\Delta T}{P_l}\right) \cdot 2 \cdot b \cdot l - R_i} \tag{2.15}$$

where R_i is the effective interface thermal resistance.

The differential 3-ω method is used in the measurement of thermal conductivity in the cross-plane direction of the thin films, being less accurate for in-plane measurements [14].

For in-plane thermal characterization, the Völklein method is more useful. This method is based once again on a transducer deposited on thin films with heat generated by Joule effect, only this time by a dc current. The temperature of the transducer is established by the change of its resistance. Considering that the increase of temperature is dependent on the heating power and thermal conductivity of both the thin film and the transducer, a setup can be designed to measure the latter specifically of the thin film (Figure 2.16).

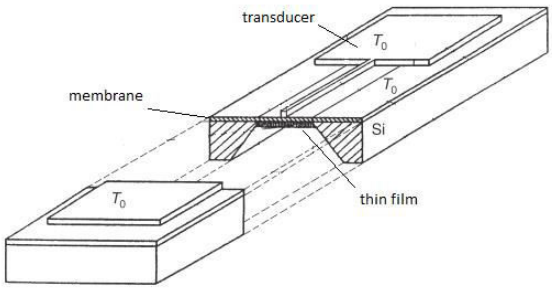

Figure 2.16. Schematic for the measurement of thermal conductivity using Völklein method [17].

Here, a suspended membrane is formed through different lithographic and etching techniques surrounded by a silicon frame. The transducer is deposited on top according to the schematic, while on the back of the membrane is the thin film that is to be investigated. The silicon frame is assumed to be at a fixed temperature acting as heat sink, meaning that the heat flow within the membrane from the transducer to the frame takes place in-plane (as long as the membrane length is far larger than its width) [14]. However, in order to calculate the thermal conductivity of the thin film, the thermal

conductivity of the membrane has to be known. This can be measured on a reference system in which the thin film is missing.

On account of availability, the technique used for the measurement of thermal conductivity in this work was the 3-ω method for out-of-plane characterization, in collaboration with the group of Olivier Bourgeois from Néel Institute, Grenoble. For this measurement, the films were coated with Al_2O_3 to ensure insulation from the Pt transducer layer (width 30 µm, length 2 mm) that was used as heater and thermometer. The method employed for the growth of the 100 nm insulating film is atomic layer deposition (ALD) based on Trimethylaluminium (TMA) and water precursors using Savannah S100 from Cambridge Nanotech as equipment, while the 100 nm Pt film was deposited by dc magnetron sputtering. Furthermore, considering the relatively high thickness of the measured films (~2 µm) and their low thermal conductivity compared to the Si substrate, the interface thermal resistance is low and was approximated in the range of 10^{-8} K·m^2/W.

2.4. Thermal treatments

The thermal stability of the thin films deposited during this work was tested after prolonged thermal treatments. These processes were performed with the use of a furnace, schematically drawn in Figure 2.17. During the thermal treatments, the samples were introduced in the alumina tube and placed in the middle of the furnace on a ceramic support. To minimize oxidation at high temperatures (although not entirely possible), the alumina tube was connected to an Ar gas tank and the samples were under Ar flow during the entire length of the thermal treatment. The heating and cooling rate used for all processes was 10 K/min and with a dwelling time at chosen temperatures for extended periods of time up to 2 weeks.

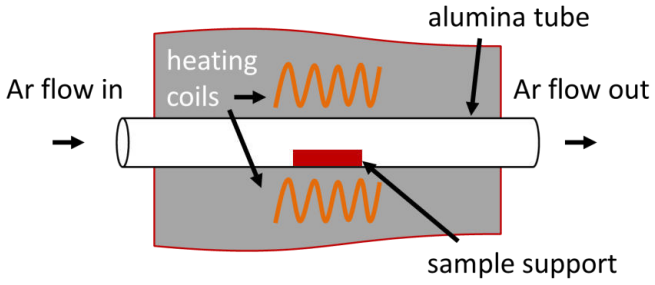

Figure 2.17. Schematic representation of the furnace used during thermal treatments.

2.5 Brazing process

Brazing is a thermal process for joining together two distinct materials at temperatures higher than 723 K without the melting of the two. However, a filler metal (brazing joint) is needed between the two materials to make the joint. The latter is accomplished by the brazing joint which is drawn

after melting to the joint by capillary forces and anchors the parts together [18]. Therefore, the melting temperature of the brazing joint needs to be lower than the melting temperatures of the neighboring materials.

The TE legs which have been deposited in this work for finding potential diffusion barrier layers have been brazed to Al or Ni electrodes using an Al-Si alloy-based brazing joint. The brazing was performed at Valeo in a prototype furnace shown in Figure 2.18 using NOCOLOK® flux technology. The TE legs were covered with the brazing joint (tens to hundreds of µm Al-Si foils) and the Al or Ni electrodes (few hundreds of µm foils) which were subsequently pressed together mechanically to ensure a proper and uniform contact between surfaces.

The TE legs pass through three zones inside the furnace during the brazing process which is performed in inert atmosphere (N_2). In the first zone, the TE legs are heated up at an intermediate temperature and maintained there for 20 min. This warm-up ensures a high quality N_2 atmosphere for the TE legs. Then the samples are moved in the second zone where the brazing takes place. Here the temperature is raised up between 820 K and 890 K with an appropriate heating rate. This temperature is high enough to melt the brazing joint which has a melting temperature in this range and thus satisfying the brazing conditions. The samples are immediately cooled down to ambient temperature with an appropriate cooling rate and thus reaching what is considered the third zone (cooling zone).

Figure 2.18. Prototype of the furnace used for the brazing process at Valeo.

The brazed samples were investigated in terms of adherence and chemical reactivity between different elements by the use of SEM and EDX after being polished (to obtain a flat cross section necessary for a proper characterization). In addition, resistivity measurements, done by 4-point probe technique, allowed testing the quality of the interface and to determine the extent to which the contact resistance (which, for the purpose of this study, needs to be minimized) is increasing.

References

[1] H. Le-Quoc, A. Lacoste, S. Béchu, A. Bès, D. Bourgault, and D. Fruchart, Deposition of thin films of $Mg_2Si_{1-x}Sn_x$ solid solution by plasma-assisted co-sputtering, Journal of Alloys and Compounds, 538 (2012) 73.

[2] Wiley-Interscience, http://lib.myilibrary.com?id=25507

[3] G. Falcone, Sputtering transport theory: The mean energy, Physical Review B, 38 (1988) 6398.

[4] D. M. Mattox, Chapter 6 - Vacuum Evaporation and Vacuum Deposition, in Handbook of Physical Vapor Deposition (PVD) Processing (Second Edition), (D. M. Mattox, ed.), William Andrew Publishing, Boston (2010) pp.195.

[5] H. Le-Quoc, A. Lacoste, E. K. Hlil, A. Bès, T. T. Vinh, D. Fruchart, and N. Skryabina, Thin films of thermoelectric compound Mg_2Sn deposited by co-sputtering assisted by multi-dipolar microwave plasma, Journal of Alloys and Compounds, 509 (2011) 9906.

[6] S. Mahieu, K. Van Aeken, and D. Depla, Transport of Sputtered Particles Through the Gas Phase, in Reactive Sputter Deposition, (D. Depla and S. Mahieu, eds.), Springer Berlin Heidelberg (2008) pp.199.

[7] http://homepage.ntu.edu.tw/~kcyuan/form/For-Rigaku-Upload_thinfilm.pdf

[8] K. Nagao and E. Kagami, Pole figure measurement, The Rigaku Journal, 27 (2011) 6.

[9] G. E. Totten, Handbook of Residual Stress and Deformation of Steel, ASM International (2002).

[10] D. Schroder, Semiconductor Material and Device Characterization, John Wiley and Sons (2006).

[11] NIST, http://www.nist.gov/pml/div683/hall_resistivity.cfm

[12] L. J. v. d. Pauw, A Method of Measuring Specific Resistivity and Hall Effect of Discs of Arbitrary Shapes, Philips Research Reports, 13 (1958) 1.

[13] D. Bourgault, C. G. Garampon, N. Caillault, L. Carbone, and J. A. Aymami, Thermoelectric properties of n-type $Bi_2Te_{2.7}Se_{0.3}$ and p-type $Bi_{0.5}Sb_{1.5}Te_3$ thin films deposited by direct current magnetron sputtering, Thin Solid Films, 516 (2008) 8579.

[14] A. Jacquot, Improvements of on-membrane method for thin film thermal condcutivity and emissivity measurements, Sensors and Actuators A, 117 (2005) 203.

[15] J. Yang, Thermal conductivity measurement of thin films by a dc method, Review of Scientific Instruments, 81 (2010) 114902.

[16] D. G. Cahill, Thermal conductivity measurement from 30 to 750 K: the 3ω method, Review of Scientific Instruments, 61 (1990) 802.

[17] F. Volklein, Measurement of the Thermal Conductivity of Thin Films, in Thermoelectrics Handbook, CRC Press (2005) pp.24.

[18] M. M. Schwartz, Brazing, ASM International (2003).

Chapter 3. Synthesis and characterization of $Mg_2(Si,Sn)$ and Mg_2Si thermoelectric thin films

This chapter concerns the synthesis and characterization of $Mg_2(Si,Sn)$ and Mg_2Si thin films deposited by microwave plasma-assisted co-sputtering. These materials are known as promising TE materials in the temperature range of 300-850 K. The objective is to determine the potential of these materials for being implemented in a thin film-based TE module, with a design promoted by Valeo.

The deposition process of the Mg_2Si-based thin films is presented, with description of the calibration for obtaining thin films with aimed stoichiometries. First, the $Mg_2(Si,Sn)$ thin films are investigated after their deposition on multiples substrates: SiO_2/Si, borosilicate glass, MgO and Ni. The choice of substrates was based on their inherent properties suitable for thermoelectric applications either as insulators or electrodes. The structural properties and morphology of the thin films are characterized after their deposition at room temperature and 463 K, while their adherence to each substrate is also verified. The thin films are then subjected to thermal treatments at temperatures up to 850 K in order to determine their thermal stability over prolonged periods of time, but also the degree of reactivity with the substrates. Furthermore, the transport properties (Seebeck coefficient and electrical conductivity) of the films were measured and compared to the values obtained in the literature for bulk materials.

Second, the effect of deposition temperature on the thermoelectric properties of Sb-doped Mg_2Si thin films was investigated. Accordingly, the structural and thermoelectric properties (Seebeck coefficient, electrical and thermal conductivities) of the doped thin films were explored, while also extracting the solubility limit for the Sb dopant from the transport properties.

3.1 Deposition of $Mg_2(Si,Sn)$ thin films: process, parameters and substrates

The growth of the $Mg_2(Si,Sn)$ thin films was done by microwave plasma-assisted co-sputtering, deposition technique which was described in Chapter 2, using 99.99% pure Mg, Si and Sn targets (60 mm in diameter). The aim is to investigate the structural, thermal and TE properties of $Mg_2(Si_{0.4}Sn_{0.6})$ solid solutions, more specifically, within the context of a thin film-based TE module described in Chapter 1.

The parameters that affect the deposition of thin film using this technique are the following:

a. the power of microwave-generated plasma
b. the Ar gas pressure inside the deposition chamber
c. the distance between the targets and the substrate
d. the voltage biases applied to the targets
e. the temperature and bias of the substrate.

The initial step in the synthesis of thin films is to adjust the voltage biases applied to each set of targets in order to obtain thin films with stoichiometric solid solutions. The stoichiometry chosen in this work for investigation as thin films is $Mg_2Si_{0.4}Sn_{0.6}$. The biases have to be chosen so that the ratio between the sputtering rates of Si, Sn and Mg are: Si/Mg = 0.4/2 = 0.2 and Sn/Mg = 0.6/2 = 0.3.

In order to calculate the appropriate voltage biases that correspond to these ratios, there was the possibility of using different models regarding energy dependence of ion-induced sputtering yields based on semi-empirical calculations, such as those put forward by Yamamura [1] and Eckstein [2] (the models are described in greater detail in Appendix 1). Initially, these models have been applied for a fixed negative bias of 600 V for the Mg target, value chosen to maximize the deposition rate, within the limitations of the DC power generator. Figure 3.1 presents the resulting calculations.

According to the Yamamura's model, the sputtering rate of Si is not sufficient even at a negative voltage bias of 600 V to reach the Si/Mg ratio of 0.2. As for Sn, the bias that ought to be applied for a Sn/Mg ratio of 0.3 is ~140 V, which translates into an acceleration of the bombarding ions at a potential of 160 V by taking into account the additional contribution determined by the plasma potential $V_p \approx 20$ V. The bias values obtained with Eckstein's model in the same conditions are 135 V for Si and 75 V (95 V with V_p) for Sn.

However, as it is seen, there is an obvious discrepancy between the outputs of the two models, most likely due to their semi-empirical nature and their imprecision for low ion energies such as those used in this work. Therefore, the attention was directed towards a previous research on $Mg_2(Si,Sn)$ thin film depositions [3] performed on a setup with a similar configuration. According to that study, in order to obtain the aimed stoichiometry, values of 600 V, 320 V and 155 V voltage biases have to be applied to the Mg targets, Si targets and the Sn targets, respectively. Finally, after a compositional

calibration of the deposition process (Table 3.1), the following set of bias values was determined for obtaining $Mg_2Si_{0.4}Sn_{0.6}$ thin films which are very close to stoichiometry: 350 V (Mg targets), 420 V (Si targets) and 220 V (Sn targets).

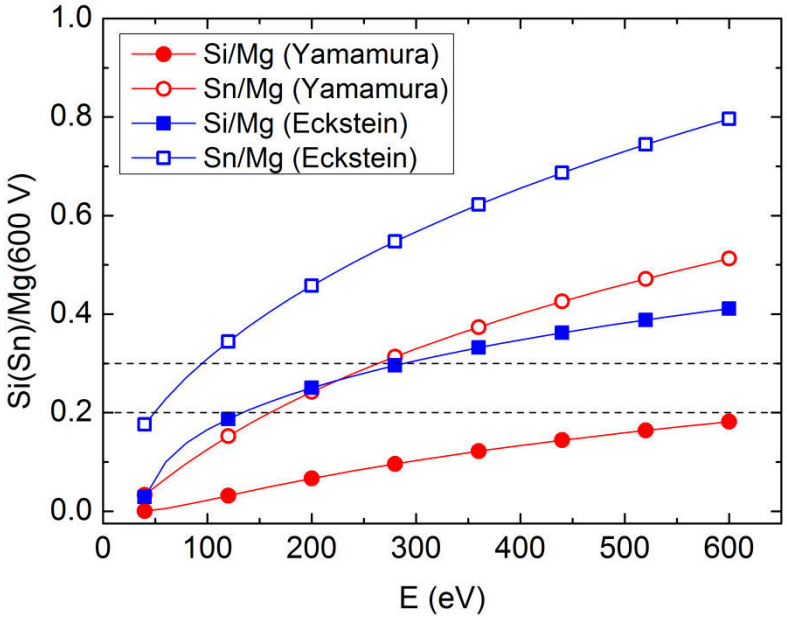

Figure 3.1. Si/Mg and Sn/Mg atomic ratios as a function of bias voltages applied to Si and Sn targets (for a fixed value of 600 V for Mg targets) according to Yamamura and Eckstein models.

The different number of plasma sources used in this work (20 sources instead of 24), as well as the different process parameters (power, pressure), can explain the different set of values necessary for the deposition of the same stoichiometry compared to the other work. The composition was investigated through quantitative measurements by EDX with an error lower than 1 wt% and further confirmed by EPMA measurements. Also, in Table 3.1 are indicated the equivalent compositions after they were normalized to the sum of Si and Sn content. This is useful in determining the Si and Sn content of the thin films deposited in this work relative to their position on the Mg_2Si-Mg_2Sn pseudo-binary phase diagram.

For the deposition of the thin films, various substrates have been used during this work, including oxidized Si wafers (0.5 mm-thick Si with an amorphous SiO_2 layer of 500 nm), 0.5 mm-thick MgO (100) substrates, 1 mm-thick borosilicate glass substrates and 2 mm-thick polycrystalline Ni substrates. The temperatures to which these substrates were kept during deposition were either room temperature (RT = 300 K) or at high temperatures (HT` = 373 K or HT = 463 K). For the formation of plasma, the Ar gas pressure was selected to be 1 mTorr (0.13 Pa) and the total microwave power of 1.7 kW (distributed through a divider guide to all 20 plasma sources). Also, to minimize energy loss between the targets and the substrate due to sputter atoms-gas collisions, the distance of 12 cm was chosen between surfaces. These parameters (power, pressure, distance, bias

values and substrate temperature) ensure overall a deposition rate of ~2 μm/h.

Table 3.1. EDX measurements of the composition of $Mg_2(Si,Sn)$ thin films deposited for different sets of bias applied to the targets

Mg/Si/Sn bias (V)	Composition	Equivalent composition
600/320/155	$Mg_{2.41}Si_{0.28}Sn_{0.31}$	$Mg_{4.08}Si_{0.47}Sn_{0.53}$
400/320/155	$Mg_{2.20}Si_{0.31}Sn_{0.49}$	$Mg_{2.75}Si_{0.39}Sn_{0.61}$
350/350/200	$Mg_{2.01}Si_{0.33}Sn_{0.66}$	$Mg_{2.03}Si_{0.33}Sn_{0.67}$
350/400/180	$Mg_{2.04}Si_{0.42}Sn_{0.53}$	$Mg_{2.15}Si_{0.44}Sn_{0.56}$
350/400/200	$Mg_{2.03}Si_{0.43}Sn_{0.55}$	$Mg_{2.14}Si_{0.44}Sn_{0.56}$
350/400/210	$Mg_{2.00}Si_{0.42}Sn_{0.58}$	$Mg_{2.00}Si_{0.42}Sn_{0.58}$
350/440/225	$Mg_{1.98}Si_{0.41}Sn_{0.61}$	$Mg_{1.94}Si_{0.40}Sn_{0.60}$
350/420/220	$Mg_{1.99}Si_{0.40}Sn_{0.61}$	$Mg_{1.97}Si_{0.40}Sn_{0.60}$

Before the deposition, the substrates were cleaved or cut in pieces with a general size of 1.5×1.5 cm^2 and placed in the center of the substrate holder. As was mentioned in Chapter 2, the pre-deposition process entails the cleaning of the substrates in an ultrasonic bath and of all involved surfaces by ion bombardment in the chamber.

3.2 Structural properties of as-deposited $Mg_2(Si,Sn)$ thin films.

$Mg_2(Si,Sn)$ thin films of composition close to $Mg_2Si_{0.4}Sn_{0.6}$ with a thickness of ~4 μm have been deposited on SiO_2(500 nm)/Si substrates at RT and HT (463 K). In Figure 3.2 are shown the cross-sectional SEM images of the two depositions. In the whole range of substrate temperature that we investigated, the as-deposited films showed no cracks, nor delamination. The film deposited at RT (Figure 3.2.a) has a relatively dense columnar microstructure with submicron in-plane feature sizes. By increasing the deposition temperature, it results to an even denser columnar morphology (Figure 3.2.b) and to highly crystalline films, due to the surplus of energy allocated to the atoms at the surface of the substrate. This translates to an enhancement of the surface diffusion and mobility of the adatoms which directly affects the resulting structure of the film.

The x-ray diffraction patterns of the films deposited on SiO_2/Si substrates at RT and HT are shown in Figure 3.3. All the peaks are accounted for, corresponding to the ternary solid solution and to the Si substrate. Within the angular resolution of the diffractometer, the RT as-deposited films appear as corresponding to a single phased $Mg_2(Si,Sn)$ solid solution with an antifluorite structure (space group Fm-3m). Depositing the films at higher temperature leads to their growth in either of two crystal structures although the deposition parameters are supposedly the same for all films. The first polymorph corresponds to the regular antifluorite structure of the solid solution. On the other hand, the second structure, although not finding a crystallographic card that matches its structure, might be

described as a hexagonal symmetry related to the $P6_3/m$ space group. Such a polymorph was previously reported not for solid solutions, but for Mg_2Sn and Mg_2Si synthesized in high pressure and high temperature conditions [4-7]. The formation of metastable polymorph is also relatively common in thin films deposited by PAPVD [8]. However, for confirmation, the structure of the second polymorph could be better characterized by Reitveld refinement, which has not been performed during this work as of yet.

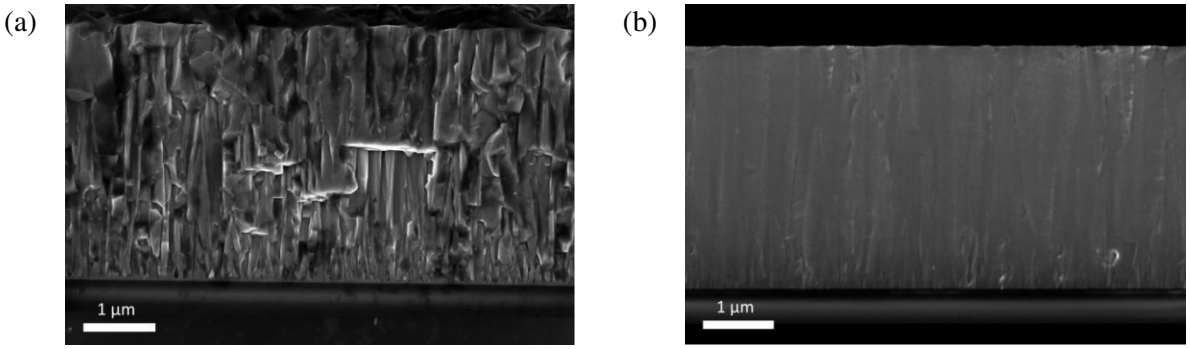

Figure 3.2. SEM cross-sectional images of $Mg_2(Si,Sn)$ thin films deposited on SiO_2/Si substrate at (a) RT and (b) HT (463 K).

Furthermore, traces of the metastable phase can be found in the thin film having, predominantly, a cubic structure (or vice-versa), suggesting that the two polymorphs can coexist in the same deposition. The mechanism behind the deposition of the films with different crystalline structures, while maintaining the deposition process assumingly unchanged, has not been determined.

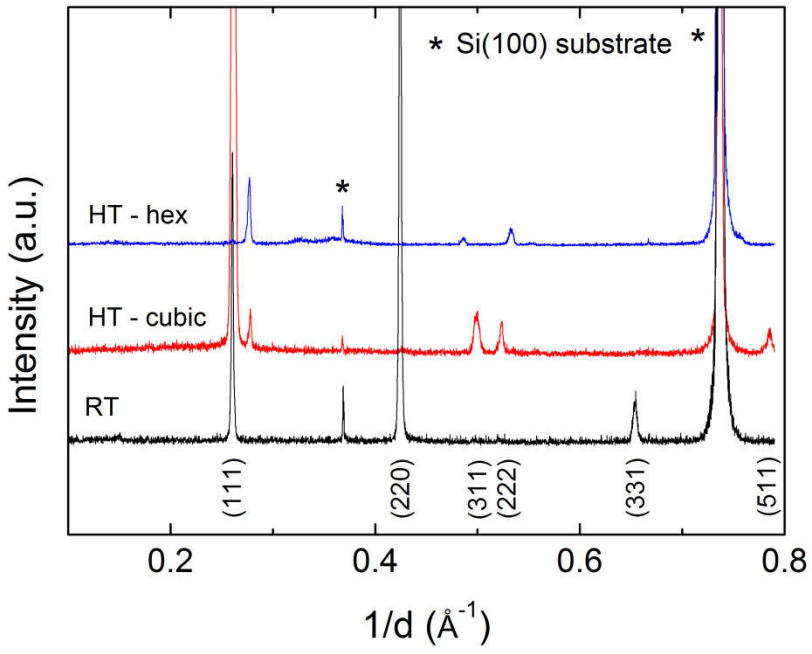

Figure 3.3. X-ray diffraction patterns of $Mg_2(Si,Sn)$ thin films deposited on SiO_2/Si substrate at RT and HT (450 K), with the crystallographic planes corresponding to the cubic phase indicated.

Considering the films with an antifluorite structure deposited at RT and HT, the two diffraction patterns testify a difference in the crystallinity of the two samples. As opposed to the film grown at RT, the film deposited at HT shows no preferential orientation, meaning that the higher deposition temperature inhibits the texturing of the film, which explains the difference in the observed Bragg peaks. Also, the broadening of the (111) peak with increasing deposition temperature testifies a decrease of the grain size inside the film.

3.3 Thermal behavior of $Mg_2(Si,Sn)$ thin films.

The $Mg_2(Si,Sn)$ thin films have been subjected to thermal treatments at various temperatures. Considering that these solid solutions are expected to be used as TE materials at temperatures as high as 850 K, the evolution and characteristics of the thin films need to be investigated at appropriate temperatures. Also, given the extended use of TE materials at the working temperatures, the thermal stability of the films and their reaction with the substrates were examined.

3.3.1 Thermal treatment at 700 K.

(i) Effects of CTE mismatch between film and substrate

The $Mg_2(Si,Sn)$ thin film, deposited at RT on SiO_2/Si substrate, was subsequently subjected to a thermal treatment at 700 K for 2 h in He flow (heating/cooling rate of 10 K/min). However, the film suffers total delamination by the end of the process. This poses the question of whether the difference in coefficients of thermal expansion (CTE) between the film and the substrate could be responsible for this behavior. The CTE of SiO_2 is widely known to be $\sim 0.5 \times 10^{-6}$ 1/°C; however the value for $Mg_2(Si,Sn)$ solid solutions has not been yet specifically determined. Nevertheless, the CTE are known for Mg_2Si (7.5×10^{-6} 1/K [9] or 11.5×10^{-6} 1/K [10]) and Mg_2Sn (9.9×10^{-6} 1/K [10]), from where it can be deduced that there is an order of magnitude separating the values of SiO_2 and $Mg_2(Si,Sn)$.

In an attempt to improve the adherence of the film to the substrate, the temperature of the latter has been increased during deposition to reduce the thermal stress of the film at high temperatures. Therefore, the deposition temperature was first increased to 373 K. This resulted to a slight amelioration of the adherence, but although the film no longer suffers a total delamination after the thermal treatment at 700 K, it continues to fracture and detach from the SiO_2 substrate (Figure 3.4.a). Due to the CTE mismatch, the film gets under tension during the cooling process and starts to fracture at ~400 K. This assumption is supported by the observed sudden drop in electrical conductivity in the cooling curve (Figure 3.4.b) during the measurement of the transport properties.

As a result, the deposition temperature was further increased to 463 K. The resulting film has a very good adherence to the SiO_2 layer, but the detachment now takes place locally at the interface between the oxide layer and Si (Figure 3.5.a). This may be explained by the increased adherence

between the film and the SiO_2 layer, while the CTE difference still leads to unavoidable fracturing of the two layers. The electrical conductivity measurement between 300 and 700 K confirms once again the fracturing at ~400 K during the cooling curve (Figure 3.5.b).

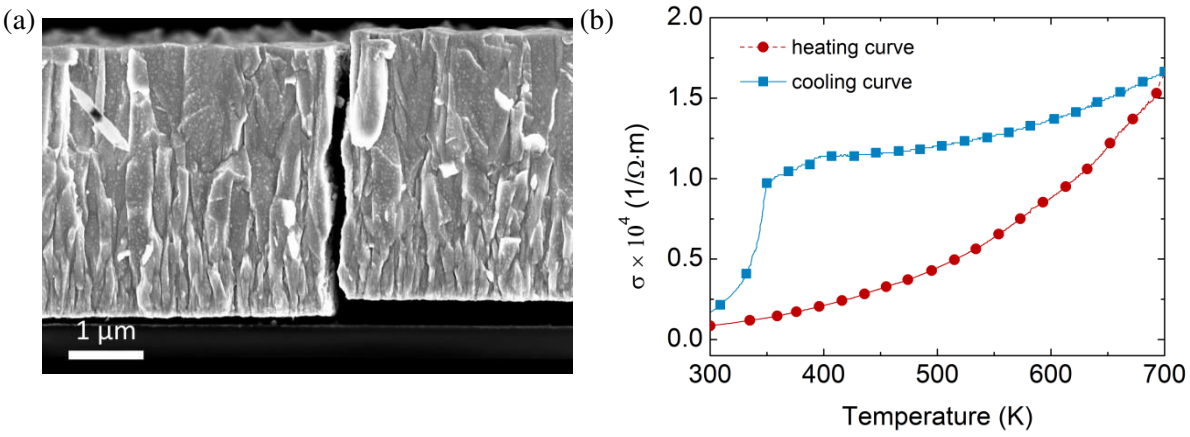

Figure 3.4. $Mg_2(Si,Sn)$ thin film deposited on SiO_2/Si substrate at 373 K after TT (700K): (a) cross-sectional SEM image and (b) electrical conductivity measurement.

This brings into focus the unlikely possibility to circumvent the mechanical properties of the interface between the film and the SiO_2/Si substrate due to the CTE mismatch solely by increasing the deposition temperature.

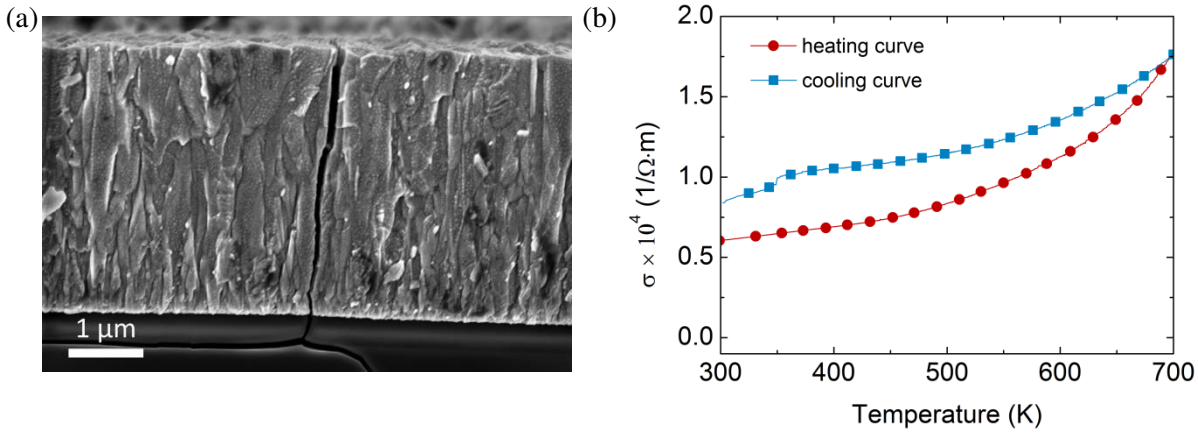

Figure 3.5. $Mg_2(Si,Sn)$ thin film deposited on SiO_2/Si substrate at 463 K after TT (700 K): (a) cross-sectional SEM image and (b) electrical conductivity measurement.

As a result, the only alternative is to find a substrate with a closer CTE to that of the film, within the constraints brought by the design of the TE module, by the deposition process and by the properties of the substrate. In other words, the substrate needs to:

- Be either a dielectric, which would ultimately act as an insulator between the TE thin films, or a metal, acting as the electrode in the assembling of the TE module, which possess good thermo-mechanical properties.
- Have a null or very low reactivity with the film within the working temperatures.

- Be cost compatible and easily implemented with large scale production.

Based on these conditions, to test the mechanical stability of the film on substrates with higher CTE at high temperatures, depositions were done at 463 K on borosilicate glass ($CTE_{glass} = 9 \times 10^{-6}$ 1/K), MgO ($CTE_{MgO} = 9\text{-}12 \times 10^{-6}$ 1/K) and Ni ($CTE_{Ni} = 13 \times 10^{-6}$ 1/K). The deposition temperature was maintained at 463 K throughout following depositions on the mentioned substrates, with no further tests being performed at room temperature.

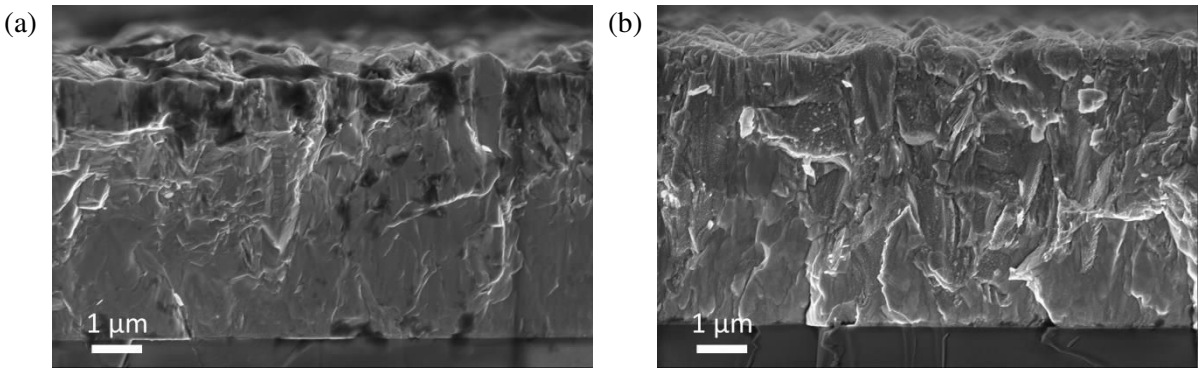

Figure 3.6. Cross-sectional SEM images of $Mg_2(Si,Sn)$ thin film deposited on borosilicate glass substrate at 463°K, (a) before and (b) after TT at 700 K (freshly cut cross-sections).

In the same deposition conditions, the film grown on borosilicate glass (Figure 3.6.a) shows no adherence issues with respect to the substrate after TT at 700 K and it no longer fractures either (Figure 3.6.b). Also we can notice that the microstructure of the film doesn't seem to be modified by the TT.

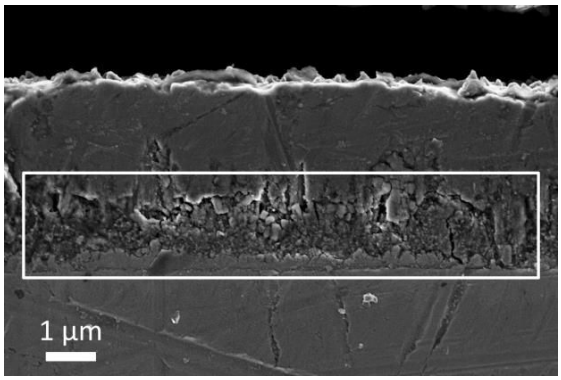

Figure 3.7. SEM cross-sectional image of $Mg_2(Si,Sn)$ thin film deposited on Ni substrate at 463 K after TT (700 K).

Similar results have been obtained for depositions done on MgO and Ni substrates, although measurements of the electrical conductivity on the latter were not performed due to the impossibility of separating the contribution of the film from that of the metallic substrate. Nevertheless, the cross section of the film grown on Ni (Figure 3.7) after the thermal treatment at 700 K reflects the lack of

fracturing or detachment. The apparent breaking of the film is due to the polishing process, which specifically affects the interface between the surfaces with different hardness.

These results confirm the necessity of using a substrate with a closer CTE to that of the film, within the aforementioned bounding properties. Based exclusively on the adherence of the film, borosilicate glass, MgO and Ni substrates satisfy the first condition.

(ii) Phase separation for Si content between 0.40 and 0.43.

Additionally, according to the post-annealing structural characterization of the films, a separation of the solid solutions into two cubic phases is visible for samples, deposited either at RT or HT, with a Si content between 0.40 and 0.43 (values normalized to Mg content) according to the phase diagram shown in Figure 3.8, regardless of the substrate on which the films were deposited.

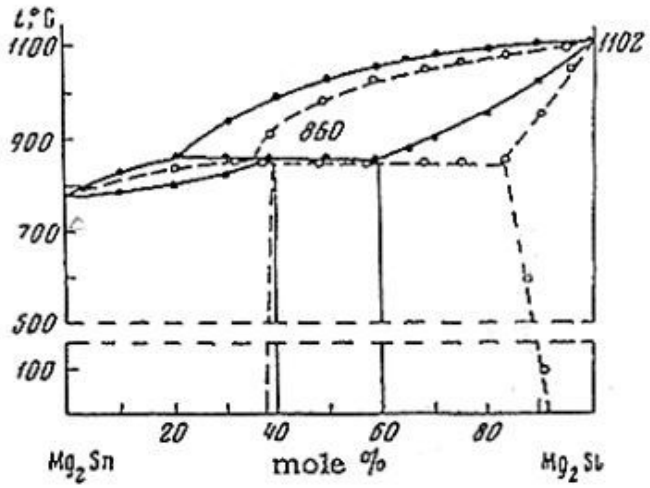

Figure 3.8. The pseudo-binary phase diagram of Mg_2Sn-Mg_2Si system, as determined by Nikitin et al. [11] (solid lines) and Muntyanu et al. [12] (dashed lines).

In the case of the as-deposited hexagonal phase, the separation is preceded by a phase transformation (exemplified for the Ni substrate in Figure 3.9) after TT at 700 K (however, the same phase separation has been observed for films with a cubic structure prior to the annealing). The two resulting phases have lattice parameters of 6.59 Å and, 6.71 Å, respectively, indicating the co-existence of two solid solutions with different Si content. This shows that the first TT acts as annealing, changing the material to a thermodynamically more stable state. The composition of the resulting two phases could have been approximated with Vegard's law, but due to the possible strains throughout the film and even the empirical nature of the law, its use would lead, in this context, to unquantifiable inaccuracies. On the other hand, the phase separation confirms the metastability of the deposited films prior to the thermal treatment for the indicated compositions.

Similar phase separation has been recently reported for $Mg_2(Si,Sn)$ materials prepared as powders by ball milling and then used to prepare bulk pellets by spark plasma synthesis [13]. The samples were thermally treated in air atmosphere up to 700 K. The emergence of the second Mg_2Sn-rich $Mg_2(Si,Sn)$ phase was observed from a temperature as low as 550 K in the case of powders with a more significant increase in content of the secondary phase at 700 K and additional heating cycles. The pellets, although proving to be more stable, also showed the presence of the Mg_2Sn-rich phase.

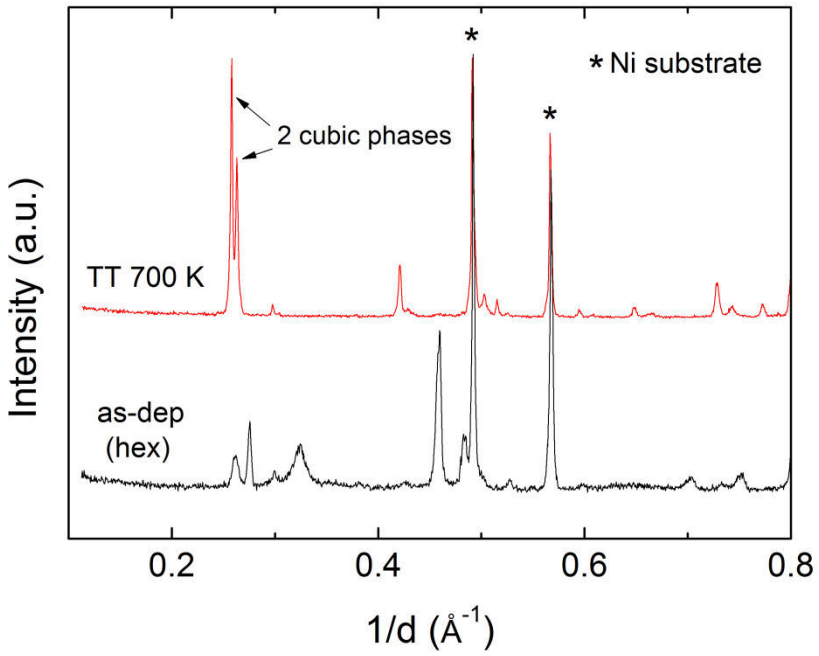

Figure 3.9. Diffraction patterns of $Mg_2(Si,Sn)$ thin films deposited at 463 K on Ni (before and after TT at 700 K).

Therefore, the instability of the $Mg_2(Si,Sn)$ solid solutions in this compositional range (Si content between 0.4 and 0.43) at moderately high temperatures, previously noticed for powders and bulk materials in a limited number of studies [13-15], is now also confirmed for thin films. It is thus suggested that the material with a Si content in the range of 0.40-0.43 lies within the miscibility gap in the pseudo-binary Mg_2Sn-Mg_2Si phase diagram. However, the actual edges of the gap are highly disputed [11, 12, 16, 17] as mentioned in Chapter 1. Nevertheless, as will later be shown, slightly changing the initial composition of the film may lead to the shift outside of the gap and consequently to the synthesis of more stable solid solutions.

3.3.2 Thermal treatment at 850 K. Decomposition of the $Mg_2(Si,Sn)$ thin films.

To investigate the behavior of the $Mg_2(Si,Sn)$ thin films and also the interface with the substrate at higher temperatures, further thermal treatments (TT) were performed at 850 K, under inert

atmosphere (He). These were done on films deposited on aforementioned substrates (SiO_2/Si, borosilicate glass and Ni).

What has been observed was the decomposition of the films, followed (or induced) by chemical reactions with each substrate. This is clearly visible from the cross sections of the films after TT (Figure 3.10). The structure of the films drastically changes (especially visible in Figure 3.10.a for the film deposited on a SiO_2/Si substrate) and all depositions present a layer underneath where the reaction with the substrate is apparent.

The decomposition of the $Mg_2(Si,Sn)$ solid solutions has been recently reported in the case of powders and bulk materials [14]. According to this report, the decomposition starts for both during prolonged thermal treatments at 630 K, particularly in the case of powders. In the case of bulk materials, a black layer with an undetermined thickness, but porous and inhomogeneous, is formed at the surface of the pellet-shaped solid solutions at temperatures as high as 775 K, promoting further decomposition inside the sample.

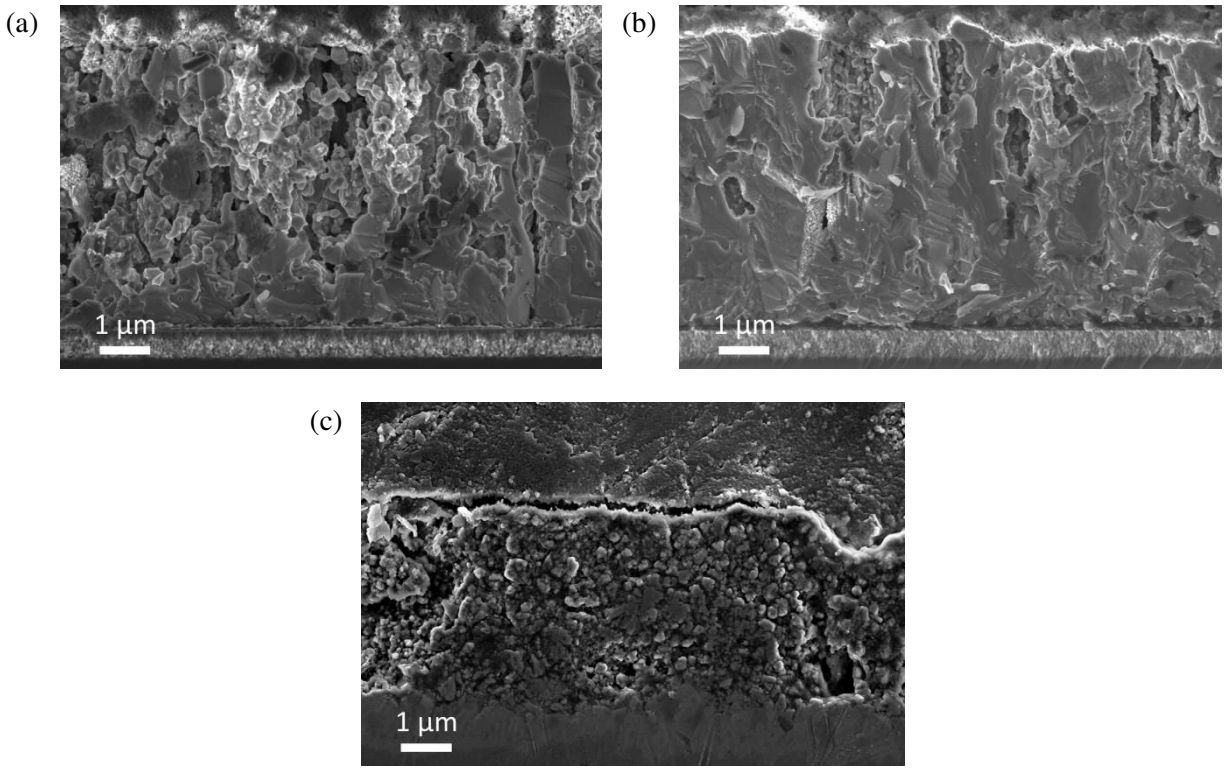

Figure 3.10. Cross sectional SEM images of $Mg_2(Si,Sn)$ films on (a) SiO_2/Si, (b) borosilicate glass and (c) Ni substrates, deposited at 463 K after TT (850 K).

For thin films, in this work, the decomposition of the ternary solid solution into metal Sn, Si, Mg and Sn-rich $Mg_2(Si,Sn)$ is also observed in the diffraction patterns corresponding to films deposited on SiO_2/Si, borosilicate glass and Ni substrates thermally treated at 850 K. The reaction of

film's components with the substrates is also visible due to the presence of a Mg-Si-Ni alloy in the film deposited on the Ni substrate.

These results, complemented by those reported for powders and bulk materials, are implying, so far, that $Mg_2(Si,Sn)$ solid solutions may not be suitable for TE applications in the expected temperature range up to 850 K, as was generally accepted [18].

3.3.3 Thermal stability of $Mg_2(Si,Sn)$ solid solutions.

(i) Si content: 0.40-0.43.

Considering the decomposition of the films with a Si content of 0.4-0.43 at moderately high temperatures (850 K), the resulting two phases must be stable only up to certain lower temperatures. In order to determine the highest temperature for which their stability is maintained, thin films have been deposited on Ni substrates and then consecutively subjected to a thermal treatment for 40 h at 700 K, 723 K and 753 K. Further tests on thermal stability were performed on MgO and borosilicate glass substrates, as will later be shown. The thermal treatments were performed in an oven with heating and cooling rates of 5 K/min and in an Ar flow atmosphere.

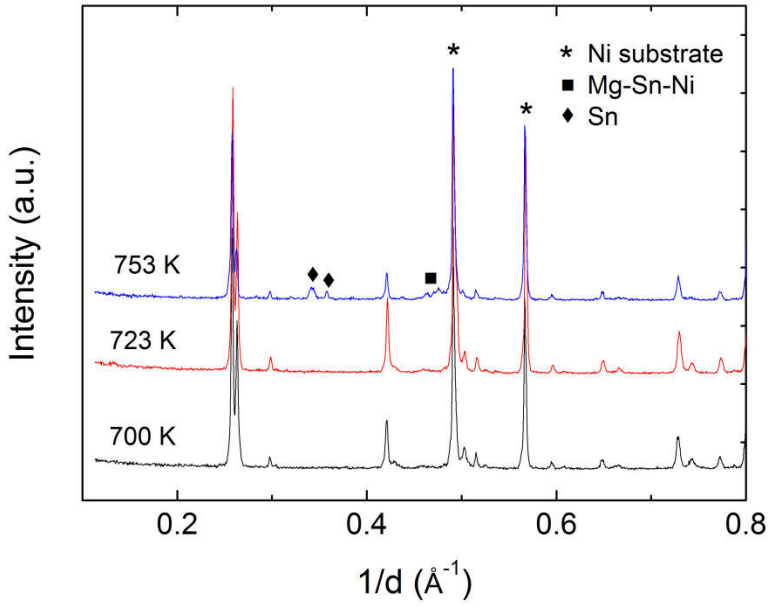

Figure 3.11. Diffraction patterns of $Mg_2(Si,Sn)$ thin film deposited at 463 K on Ni substrate after TT at various temperatures (700 K, 723 K, 753 K) for 40 h.

The results are presented in Figure 3.11 where the diffraction patterns of the film after each thermal treatment are shown. According to the FWHM of the peaks it is observed that the crystallinity of the film is improving along with the increase in temperature. On the other hand, at 753 K it becomes obvious that the ternary material is deteriorating with a phase of Sn being noticed, clearly showing the decomposition of the film. Also, peaks corresponding to a Mg-Sn-Ni phase are emerging,

suggestive of a reaction between the film and the substrate. It is thus implied at this point that the highest temperature at which the thermal stability of the $Mg_2(Si,Sn)$ solid solutions is no higher than 700 K for thermal treatments up to 40 h.

A question now arises even for the thermal treatments performed at lower temperatures where the material seemed to be stable and that is whether the time used for these processes (40 h) was enough to extinguish any doubt on the instability of the materials. This question becomes pertinent from a technological standpoint as well, considering that the lifetime of a TE module is expected to be quite high.

Therefore, further ageing tests have been carried out, consisting of thermal treatments extended over the length of 336 h. These have indeed proven that the ternary solid solution is just as unstable at lower temperatures as at higher temperatures if the material is subjected to realistic working conditions. This can be seen in Figure 3.12 where there is a pronounced reaction of the film with the substrate after TT at 700 K for 336 h, leading to the formation of Mg-Sn-Ni alloy. Also, a small trace of Sn is also visible, demonstrating the initiation of decomposition. This outcome highlights the significance of a prolonged TT during any tests on the thermal stability of the material for any chosen temperature.

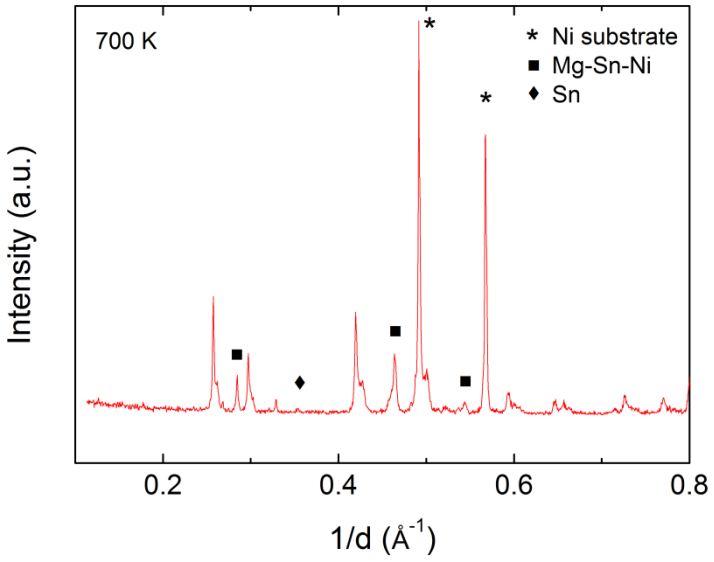

Figure 3.12. Diffraction patterns of $Mg_2(Si,Sn)$ thin film deposited at 463 K on Ni substrate before and after TT at 700 K for 336 h.

In light of the aforementioned results, the temperature of the thermal treatment was lowered to 653 K, with two such processes being used: one for 40 h and the second for 168 h. The length of the first thermal treatment was specifically chosen to emphasize the stabilizing phase transformation through which the original metastable phase goes, while the second one having solely the purpose of testing the stability of the resulting cubic phases. As it becomes obvious from Figure 3.13, the

temperature of 653 K seems to maintain the structure of the $Mg_2(Si,Sn)$ solid solutions intact and also no reaction of the film with the Ni substrate is discernable from the diffraction patterns.

However, although the solid solution is thermally stable at this temperature, if the reaction between the film and the Ni substrate occurs locally or is just incipient, it is not always possible to notice it through x-ray diffraction. To this aim, SEM images are more revealing if they are obtained by using the ESB detector, which gives information on the compositional contrast. Therefore, in Figure 3.14 is shown the cross-sectional ESB-SEM image of the interface between the film and the Ni substrate. Here, the brighter regions are contaminants from the polishing process, during which a slurry of diamond particles was used. Also, the cracks were most likely determined by the stress induced during polishing as was previously mentioned. More importantly however, the onset of the reaction between the film and the Ni substrate is observed at their interface. In terms of TE applications, this result enforces the necessity of using a diffusion barrier between the $Mg_2(Si,Sn)$ thin films and Ni to avoid their reaction.

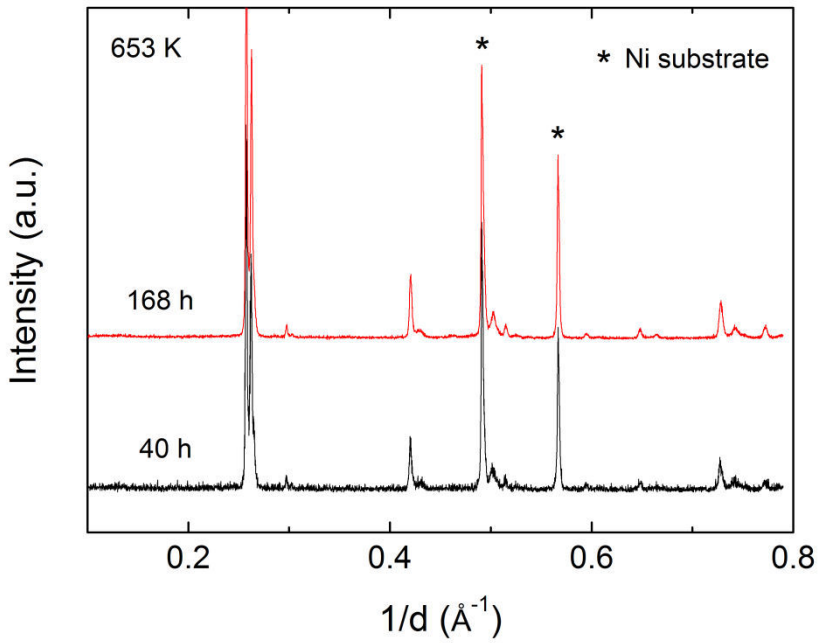

Figure 3.13. Diffraction patterns of $Mg_2(Si,Sn)$ thin film deposited at 463 K on Ni substrate as-deposited and after TT at 653 K for 40 h and 168 h.

Additionally, $Mg_2(Si,Sn)$ thin films were also grown on MgO substrates and then subjected to high temperature thermal treatments (even higher than 653 K) in order to ascertain their adherence and reactivity in relation with the substrate. The choice of the MgO was done not only with respect to its CTE, but also due to previous reports that have presented the low reactivity of Mg-based compounds with MgO substrates [19, 20].

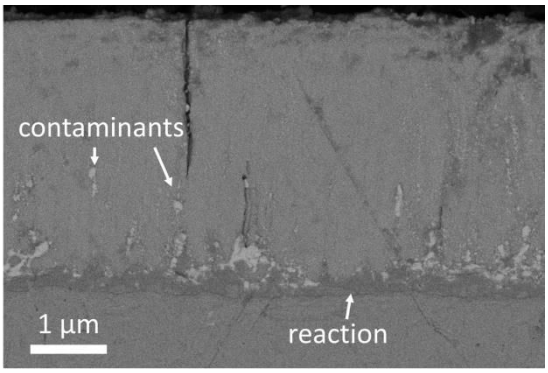

Figure 3.14. Cross-sectional ESB-SEM image of the interface between $Mg_2(Si,Sn)$ and Ni substrate after TT at 653 K for 168 h.

Despite the expected decomposition of the film after the thermal treatment at 700 K for 336 h, as it can be seen in Figure 3.15.a where a cross-sectional SEM image of the film is presented, the film did not delaminate from the MgO substrate and it shows no sign of fracturing as it was previously observed for the films deposited on SiO_2/Si substrates. Moreover, no reactivity with the MgO substrate is noticed, proving the stability of the substrate at high temperatures and its low diffusion in contact with the ternary film (the bright interface between the film and the substrate is due to unavoidable charging that arises during the measurement from the dielectric properties of the substrate and not a sign of reaction).

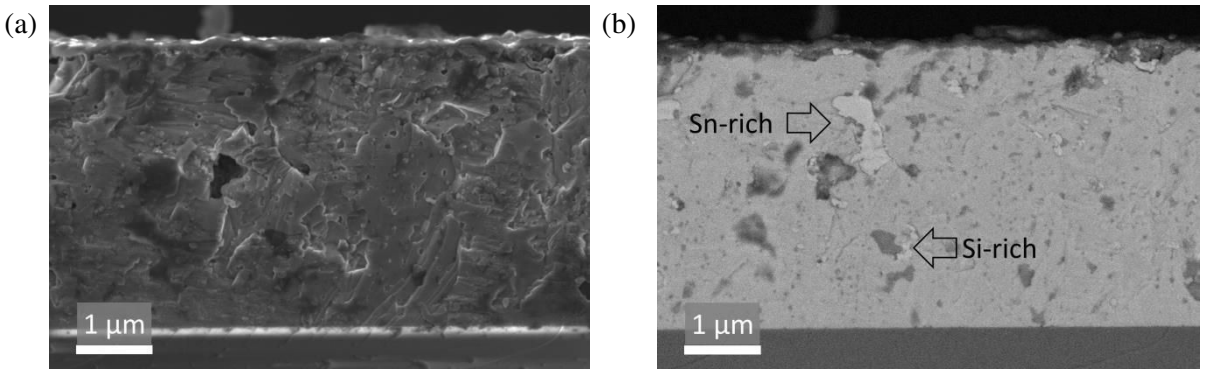

Figure 3.15. Cross-sectional SEM images of $Mg_2(Si,Sn)$ thin film deposited at 463 K on MgO substrate after TT at 700 K for 336 h: (a) InLens, (b) ESB.

This result favors the use of the MgO substrates in future depositions as a possible candidate for an insulator in the TE module.

One further observation that can be made is that the decomposition of the ternary solid solutions is obvious from the visible segregation of Sn-rich and Si-rich phases in the cross-section of the film by using the ESB detector (Figure 3.15.b).

(ii) Si content: 0.38.

$Mg_2(Si,Sn)$ thin films with a slightly lower Si content (0.38) have been grown on a borosilicate glass substrate in order to investigate the effect of the change in composition on the thermal behavior of the films at moderately high temperatures, but also to assess the reactivity and adherence to the substrate. For this purpose, the films were thermally treated at 653 K for 1 week (168 hours) in an Ar flow atmosphere.

As a result, in Figure 3.16 are shown that cross-sectional SEM images of the film before and after TT. The surface of the thermally-treated film is covered in a thin layer of oxide flakes, as a result of the unavoidable small amount of oxygen that is found in the furnace used during the thermal process. Also, the rough shape of the entire cross-section comes from cutting and breaking of the borosilicate glass substrate with a diamond tip. This leads to obvious changes compared to the cleaved SiO_2/Si substrates. However, there is no trace of detachment or fracture of the film, suggesting good thermo-mechanical properties at its interface with the borosilicate glass substrate.

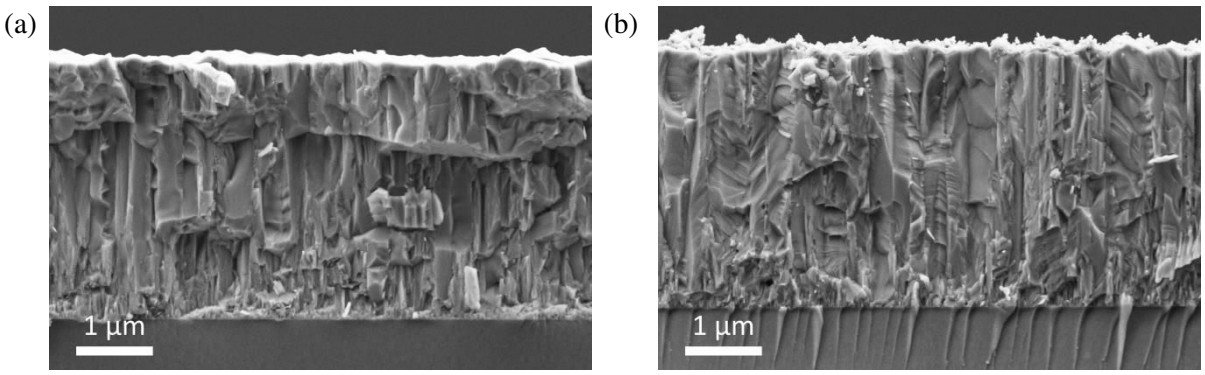

Figure 3.16. Cross-sectional SEM images of $Mg_2(Si,Sn)$ thin film deposited at 463 K on borosilicate glass substrate: (a) before and (b) after TT at 653 K for 168 h.

The lack of reactivity with the substrate was monitored by EDX mapping of the interface (shown in Figure 3.17). Here are included the compositional images of the predominating elements visible in the sample. As a mention, in the case of the image following the Si content, although the element seems to be present exclusively in the substrate, it can also be found in the film, but the film/substrate ratio content is very low and therefore the contrast is high, being difficult to distinguish the Si from the film over that in the substrate.

Overall however, this measurement does not lead to conclusive results due to difficulties in obtaining stark contrasts between the two materials, making it difficult to perform elemental investigation of the interface due to the spatial resolution which is at the scale of the thickness of the film. Moreover, unavoidable charging of the sample due to the insulating nature of the substrate reduces the scanning time of the measurement and hinders the obtaining of higher resolutions images.

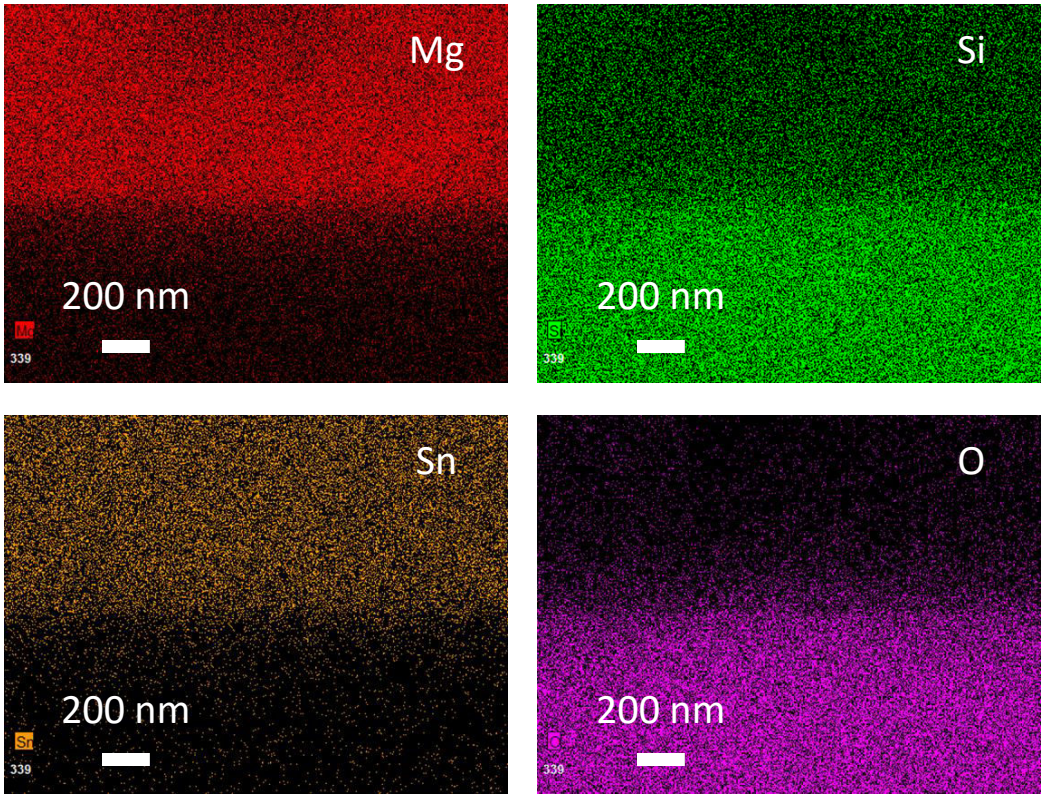

Figure 3.17. Elemental mapping at the microstructural level by EDX of the interface between the $Mg_2(Si,Sn)$ film and the borosilicate glass substrate after TT at 653 K for 168 h.

To settle the matter of reactivity, SEM is particularly helpful when the ESB detector is used, giving compositional contrast. Therefore, Figure 3.18 shows a very clear interface between the film and the borosilicate glass substrate after the thermal treatment (653 K, 168 h) and no reactivity between the two can be detected.

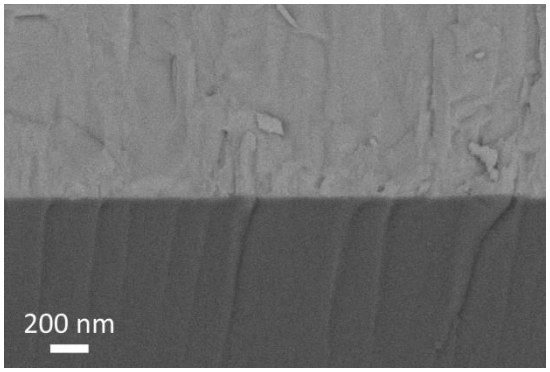

Figure 3.18. ESB-SEM cross-sectional image of the interface between the $Mg_2(Si,Sn)$ film and the borosilicate glass substrate after TT at 653 K for 168 h.

The same observation can be extracted from the diffraction patterns of the film (Figure 3.19) where no other peaks are noticed except those corresponding to the $Mg_2(Si,Sn)$ solid solution (the amorphous borosilicate glass substrate does not diffract). Here was the case where the as-deposited

film was in the cubic antifluorite phase even before annealing. However, more revealing, it becomes obvious that the thin film no longer goes through a phase separation during the thermal treatment. The shift of the peaks with respect to the original position from the diffraction pattern of as-deposited film is accounted by the stress relaxation.

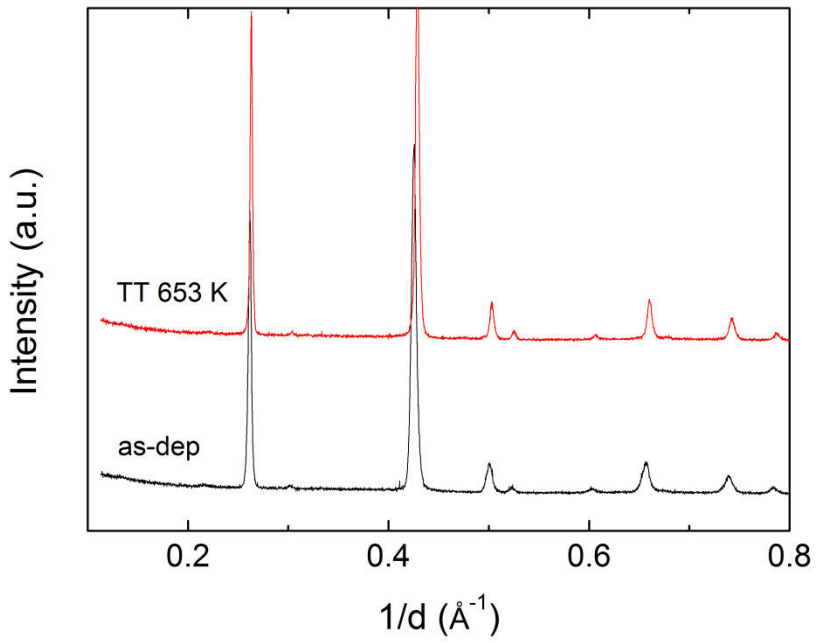

Figure 3.19. Diffraction patterns of $Mg_2(Si,Sn)$ thin film deposited at 463 K on borosilicate glass substrate: as-deposited and after TT at 653 K for 168 h.

What is obtained is a single-phased $Mg_2(Si,Sn)$ solid solution, raising the possibility of an initial composition outside the miscibility gap, despite the conflicting results that have been reported concerning its edges. What remains to be seen is whether the stability of the obtained solid solution, with a Si content lower than 0.40, translates into a higher working temperature than what was previously found in this work for samples with higher Si content (653 K).

3.4 Transport properties of $Mg_2(Si,Sn)$ thin films.

The electrical conductivity was measured by 4-point probe method, using a non-commercial setup, in a temperature range of 300-700 K with heating/cooling rate of 10 K/min. It was shown in a previous section that during the cooling of the films, the drop in the electrical conductivity was explained by the poor adherence of the film to the substrate. Once this was resolved by changing substrates, the measurement done for films deposited on borosilicate glass (Figure 3.20) shows that after the first thermal cycle, the following cycles are reproducible and the electrical conductivity follows the same dependence with temperature both during heating and cooling. The temperature dependence obtained for the electrical conductivity is specific to semiconductors and with values

(10^4 $\Omega^{-1}m^{-1}$) comparable to those reported for un-doped bulk materials [21]. The difference noticed between the first heating and cooling cycles can be translated by the microstructure changes and stress relaxation that occur during the first annealing.

Measurements of the Seebeck coefficient have been performed at ambient temperature on thermally treated $Mg_2(Si,Sn)$ thin films (single-phased and two-phased). The values obtained range between 110-170 µV/K, suggesting a p-type behavior of the film. This result is in stark contrast with most of what was reported on $Mg_2(Si,Sn)$ solid solutions as bulk materials [22], which is indicative of n-type materials. Moreover, by comparing the absolute values between the two, the Seebeck coefficient of the film seems to be much lower than for bulk materials (400-600 µV/K at RT). On account of the possible effect of Mg content on the transport properties of the material, the measurements were performed for both under-stoichiometric and over-stoichiometric thin films (with values of the Mg content between 66 and 67.5 at%). However, the Seebeck coefficient has remained the same in all cases, still suggestive of a p-type material. On the other hand, the results presented here are similar to those previously reported on $Mg_2(Si,Sn)$ thin films [3].

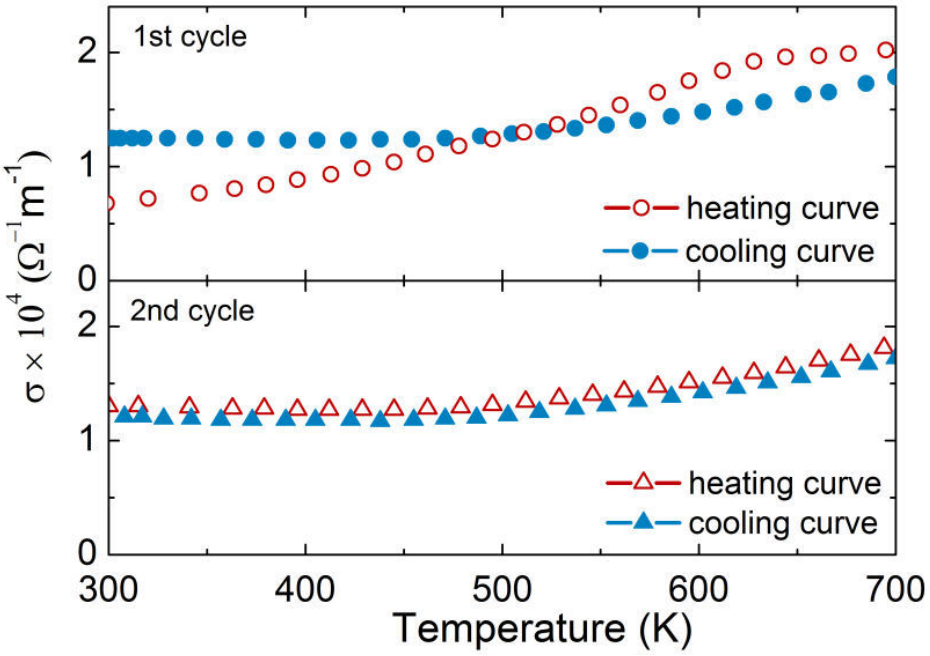

Figure 3.20. Electrical conductivity dependence with temperature of a $Mg_2(Si,Sn)$ thin film deposited at 463 K on borosilicate glass substrate: first and second heating/cooling cycles.

The results are summarized in Table 3.2 where the values of the electrical conductivity and Seebeck coefficient at room temperature are obtained for indicated depositions after TT. Further investigation, including microstructural characterization and theoretical modeling of the transport properties for thin films, is needed to establish how does a switch of majority carriers occurs, i.e. the change from an n-type to a p-type material.

Table 3.2. Transport properties measurements at RT of thin films with different compositions.

Composition	Si content $x_{Si}/(x_{Si}+x_{Sn})$	TT	No. cubic phases	σ (1/Ω·m)	α (μV/K)	Ref.
$Mg_{1.98}Si_{0.41}Sn_{0.61}$	0.40	573 K, 3 h, Ar	2	1.3×10^4	110	this work
$Mg_{2.01}Si_{0.43}Sn_{0.56}$	0.43	600 K, 9 h, He	2	0.7×10^4	130	
$Mg_{2.02}Si_{0.37}Sn_{0.61}$	0.38	653 K, 5 h, He	1	1.1×10^4	170	
$Mg_{2.01}Si_{0.40}Sn_{0.59}$	0.40	-	-	4.3×10^2	100	[3]

Overall, there appears to be no difference in electrical conductivity between single-phased and two-phased thin films, but a slight increase of the Seebeck coefficient (from 110 m V/K to 170 m V/K) was observed for the single-phased film. However, this may also be attributed to the composition closer to a Si content of 0.35, for which the overlapping of the two conduction bands (corresponding to Mg_2Si and Mg_2Sn) was previously reported [23] (see Figure 1.14). Therefore, the impact of the structure (single-phased or two-phased) on the thermoelectric properties (including thermal conductivity) still needs to be assessed in the future.

3.5 Investigation of Sb-doped Mg_2Si thin films

On account of the uncertainties connected to the use of $Mg_2(Si,Sn)$ solid solutions for moderately high temperature (850 K) applications, the attention was diverted towards the Mg_2Si compound which was shown to be efficient for intermediate temperature up to 850 K [24-26]. Furthermore, by doping Mg_2Si with Sb, the thermoelectric properties of the n-type material are enhanced for optimized compositions.

3.5.1 Deposition of Sb-doped Mg_2Si thin films

For the deposition of Mg_2Si thin films, the process has been adjusted to obtain stoichiometric Mg_2Si thin films by varying the bias applied to the Mg and Si targets (settled on 150 V for Mg and 600 V for Si), with the composition determined by EDX. For the deposition of the Sb, a target with a diameter of 50 mm placed in the center of the target holder was used.

According to literature, the solubility limit for Sb in Mg_2Si bulk materials is ~1 at%, while the optimum content was determined to be 0.5 at% based on the TE properties of the bulk materials [25]. In this work, a set of values was chosen for biasing the Sb target to determine the composition of the resulting films, as well as the structural and transport properties in order to establish the Sb content that leads to the best TE properties. Additionally, it was foreseen to also find the solubility limit, as a reference.

Table 3.3. Set of bias values applied to the targets to obtain un-doped and Sb-doped thin films with indicated composition

Bias Mg-Si-Sb (V)	Composition
150-600-0	$Mg_{2.03}Si_{0.97}$
150-600-12	$Mg_{2.017}Si_{0.974}Sb_{0.009}$
150-600-15	$Mg_{2.014}Si_{0.967}Sb_{0.019}$
150-600-18	$Mg_{2.030}Si_{0.944}Sb_{0.026}$
150-600-21	$Mg_{2.033}Si_{0.935}Sb_{0.032}$
150-600-24	$Mg_{2.046}Si_{0.911}Sb_{0.043}$
150-600-27	$Mg_{2.032}Si_{0.916}Sb_{0.052}$
150-600-30	$Mg_{1.994}Si_{0.938}Sb_{0.068}$
150-600-40	$Mg_{2.009}Si_{0.881}Sb_{0.109}$

The samples that have been deposited on SiO_2/Si substrates are presented in Table 3.3, where the bias applied to the targets and the corresponding composition of the resulting films are shown. The minimum Sb content which was obtained for a bias value of 12 V is 0.009. For a lower bias, no traces of Sb have been observed in the resulting thin film. The evolution of the Sb content with the bias applied to the target is shown in Figure 3.21.

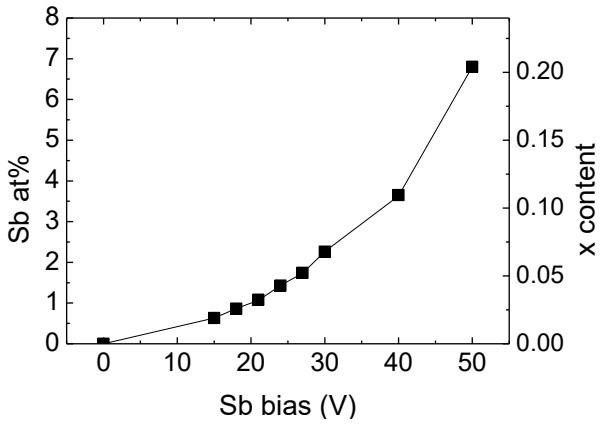

Figure 3.21. The dependence of Sb content in the Mg_2Si films with the bias applied to the Sb target

The structural characterization of the deposited thin films has been performed by XRD. This may also offer additional information on the structural effect of Sb on the Mg_2Si compound and perhaps even give an indication on the solubility limit. The diffraction patterns of the as-deposited films are shown in Figure 3.22.

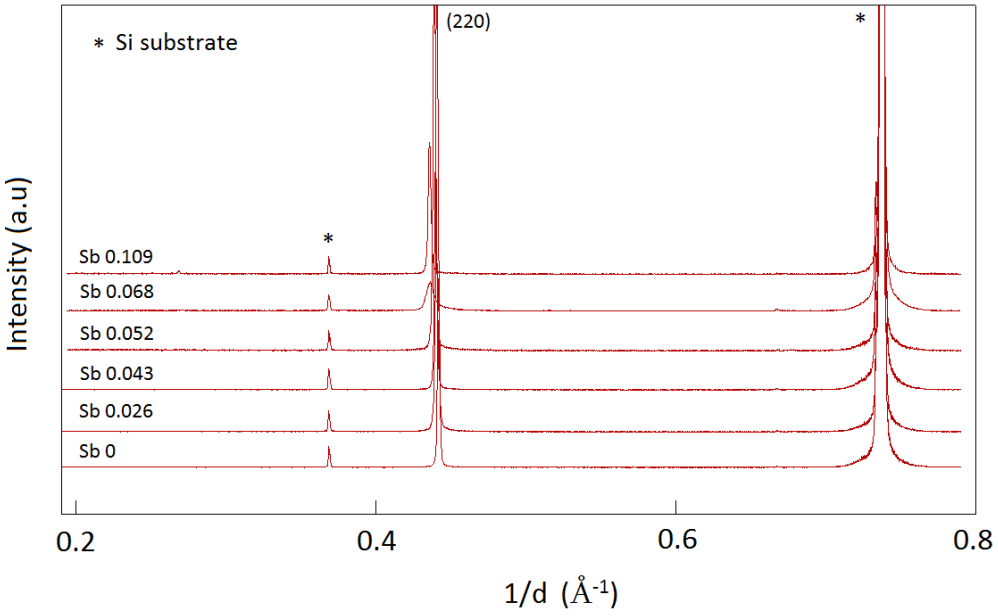

Figure 3.22. Diffraction patterns of un-doped and Sb-doped Mg_2Si thin films deposited on SiO_2/Si substrates at RT.

All Bragg peaks are accounted for, which correspond either to the $Mg_2Si(Sb)$ solid solution or to the Si substrate. The films are highly textured, due to the predominant presence of the Bragg peak corresponding to the (220) of the Mg_2Si phase, as it will later be discussed. However, despite the gradual increase of Sb content in the film, which reaches compositions exceeding the solubility limit reported in the literature, there is no indication of an additional Sb phase in the thin films. The lack of Sb segregation in the diffraction patterns can therefore be explained by the minute content of the Sb phase throughout the films, making it undetectable by XRD.

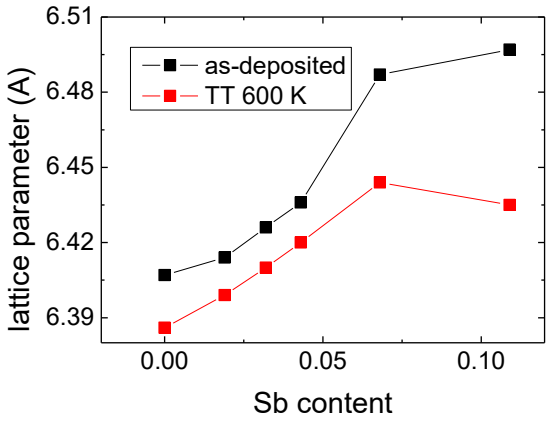

Figure 3.23. Dependence to the bias applied to the Sb target of the lattice parameter of un-doped and Sb-doped Mg_2Si thin films

Nevertheless, the presence of the Sb in the Mg_2Si lattice can be indicated by the evolution of the lattice parameter, extracted from the position of the (220) peak, which shifts with the addition of

Sb. In Figure 3.23 it is shown the increase of the lattice parameter with the Sb content, suggesting the replacement of the Si atoms with Sb atoms in the unit cell or the interstitial placement of the Sb atoms in the lattice. The values are obtained for both as-deposited samples and after their subsequent thermal treatment at 600 K in He atmosphere (performed during the measurement of the electrical conductivity). The tests were performed on SiO_2/Si substrates and therefore the upper temperature was appropriately chosen to avoid any adherence issues. The decrease of the lattice parameter after the thermal treatment suggests that the as-deposited films are characterized by intrinsic stress generated by the deposition process. This decrease of the lattice parameter is observed for all samples, but it becomes more pronounced for higher Sb content, which may suggest indirectly that the thermal treatment leads to the segregation of Sb outside the Mg_2Si phase.

3.5.2 Investigation of the texture

In the following, the effect of the deposition temperature on the crystalline structure of un-doped Mg_2Si thin films is assessed. For this, thin films grown at RT and HT (463 K) were used and their structural properties, namely the degree of texture and strain, were investigated through XRD measurements on Texture and Bragg Brentano goniometer, respectively. For texture characterization, three out-of-plane crystallographic planes were chosen, (220), (311) and (422), on account of them having the highest relative intensities.

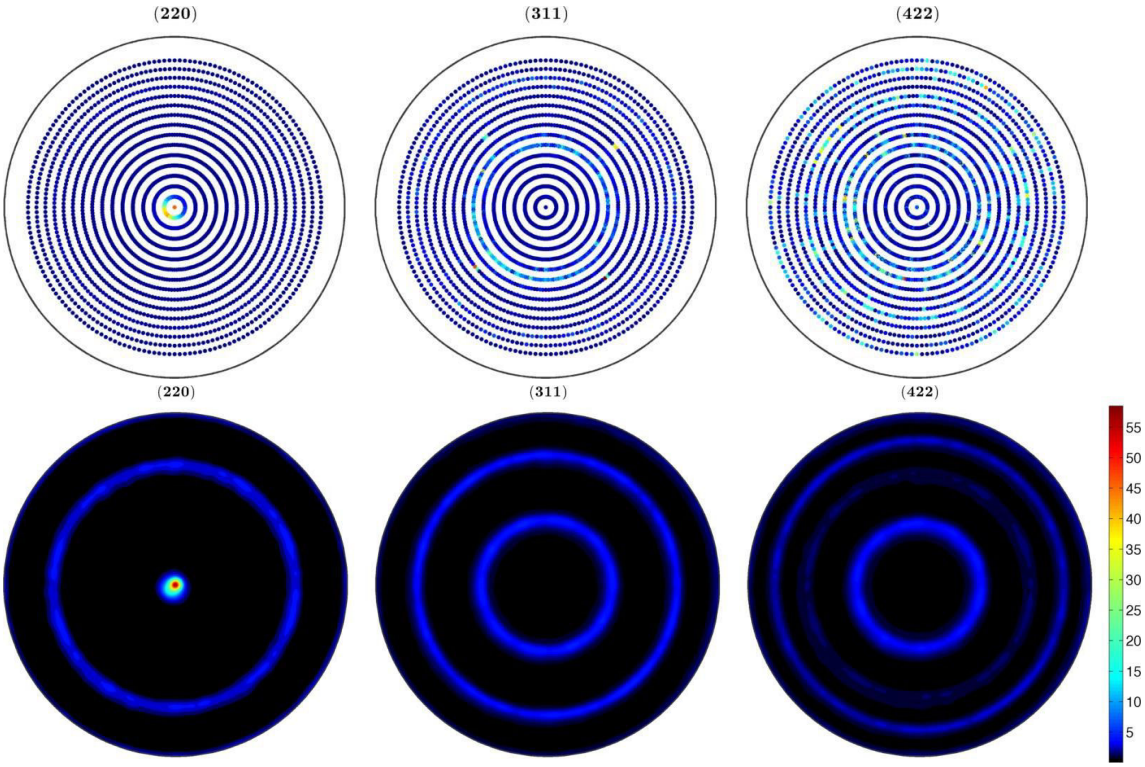

Figure 3.24. Pole figure measurements of un-doped Mg_2Si thin film deposited at RT: (above) experimental and (below) MTEX simulations.

In Figure 3.24 are shown the pole figures of the film deposited at RT, both experimental and simulated with MTEX software. The successful reconstruction of the pole figures with MTEX suggested a high degree of texturing. Due to the pole maximum at the center position of the 220 pole figure, it is shown that the thin film has a uniaxial orientation (or fiber texture) in the [220] direction. It was approximated that >99% of the crystallites are grown along this direction. Furthermore, the slightly off-position of the pole maximum indicates the presence of strains within the thin film.

In order to quantify the stress, the $\sin^2\Psi$ technique was used, presented in Chapter 2, which allows their calculation in any direction starting from the inter-planar distances measured at different tilt angles, Ψ. Accordingly, the stress was calculated in the [220] direction by first measuring the shift of the (220) Bragg peak with the variation of tilt angle. This shift is shown in Figure 3.25, where the linear dependence to $\sin^2\Psi$ in the negative quadrant is indicative of compressive stress. Once the slope was established after a linear fitting of the experimental data, the stress was determined using equation 2.4 to be -1.47 GPa.

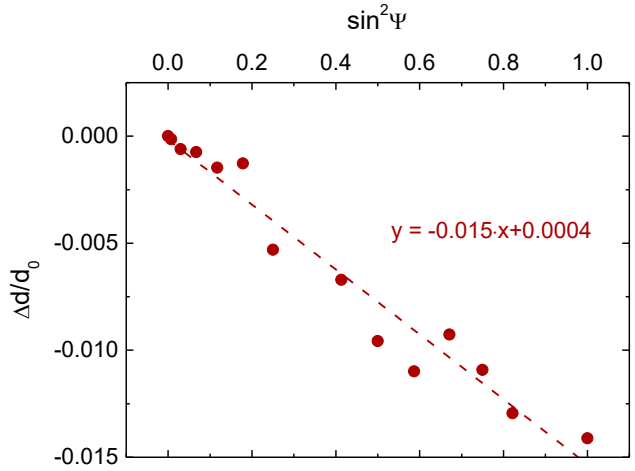

Figure 3.25. Dependence of $\Delta d/d_0$ with $\sin^2\Psi$ determined for stress calculation for un-doped Mg_2Si thin film deposited at RT.

By increasing the deposition temperature to HT (463 K), changes are noticed in the structure of the thin films. However, the pole figure measurements which were performed, as before in the three crystallographic directions, could not be easily simulated (shown in Figure 3.26). Nonetheless, in a first-order approximation, although the film still presents a certain degree of texture, it can be inferred that the crystals are less oriented in the [220] direction than the film deposited at RT.

To further investigate the structural properties of the Mg_2Si thin film deposited at HT, in-plane measurements were performed. The result is presented in Figure 3.27, where the diffraction patterns obtained for Ψ=0° and Ψ=90° are compared. The latter shows the Bragg peaks that correspond to all Bragg peaks, much as what is usually obtained during powder characterization, while the diffraction pattern at Ψ=0° shows the presence exclusively of the aforementioned two planes (220) and (311).

This means that the crystallites are more-or-less textured along the directions [220] and [311] which are normal to the sample surface, while in the plane of the film the crystallites are randomized confirming the fiber texture of the film.

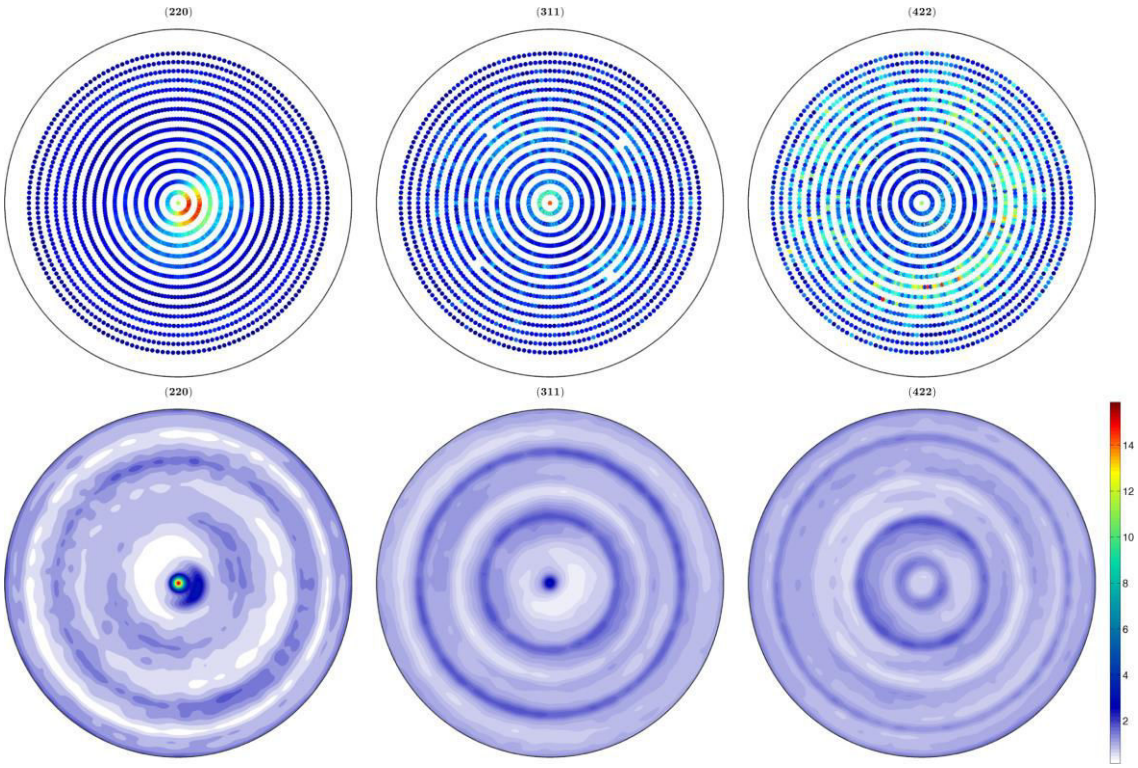

Figure 3.26. Pole figure measurements of un-doped Mg_2Si thin film deposited at HT (463 K): (above) experimental and (below) MTEX simulations.

Moreover, in the inset from Figure 3.27 is shown the comparison between the positions of (220) and (311) Bragg peaks at the two values of tilt angles. The relative position of the two peaks for $\Psi=90°$ corresponds, as expected, to a cubic structure. In the case of the diffraction pattern measured at $\Psi=0°$, the relative position of the two is shifted and no longer matches the condition of a cubic arrangement. The positions are more indicative of a cell deformation that may originate from the stress of the film. However, further investigations are in progress in order to elucidate these observations and also to determine if similar deformation can be found for the thin film deposited at RT.

In order to determine the stress within the film deposited at HT, the peak positions of the (220) Bragg peaks were once more measured while varying the tilt angle. The obtained result is shown in Figure 3.28. Unlike for the film deposited at RT, the dependence between the peak positions and $\sin^2\Psi$ is no longer entirely linear. The presence of the non-linear section suggests an inhomogeneous strain in the thin film or strain gradients along the direction normal to the surface of the film [27]. Nevertheless, the linear section was used to approximate the stress in this direction and to obtain a value of -1.07 GPa. This shows that, within a certain margin of error, the deposition at HT reduced not only the degree of texture in the resulting Mg_2Si thin film, but also the intrinsic stresses.

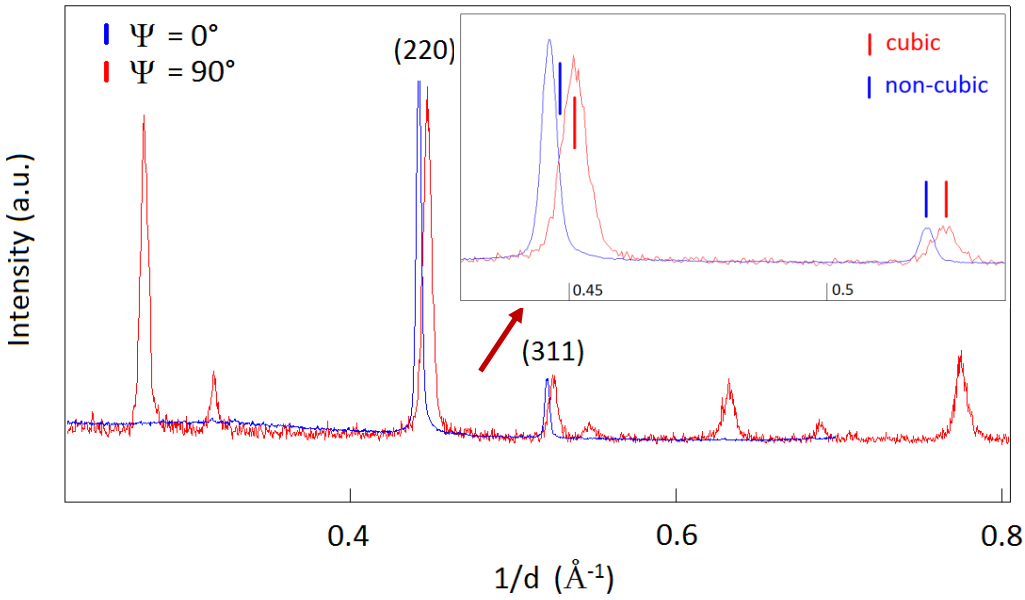

Figure 3.27. In-plane XRD measurements of un-doped Mg_2Si thin film deposited at HT (463 K) for tilt angles of 0° and 90°

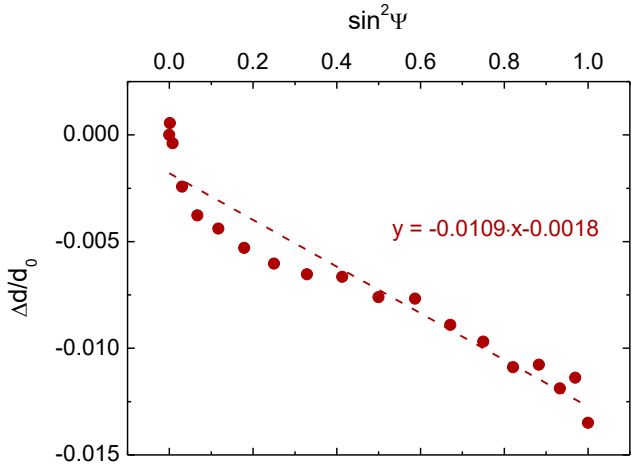

Figure 3.28. Dependence of $\Delta d/d_0$ with $\sin^2\Psi$ determined for stress calculation for un-doped Mg_2Si thin film deposited at HT (463 K).

3.5.3 Investigation of the physical properties

The electrical conductivity has also been investigated of the un-doped and Sb-doped Mg_2Si thin films deposited both at RT and HT, as a first step in their evaluation as TE materials. The measurements were performed in He atmosphere by the four-point probe method during three consecutive heating-cooling cycles between 300-600 K with a dwell time of 3 h at 600 K. The dependence of the electrical conductivity to the temperature within the mentioned range is indicated in Figure 3.29, where the cooling curves of the third cycles are represented. The choice of the third cycle

can be put on account of the crystalline relaxation that takes place after the first cycle, as was previously mentioned in the evolution of the lattice parameter.

The obtained values in electrical conductivity at 300 K for the un-doped Mg_2Si thin films are distinctly different than what was previously reported for un-doped bulk materials. The comparison between various studies is presented in Table 3.4. A rather large discrepancy is observed as well for the bulk materials, which can be put on account on the changes in their other transport properties. These may be determined by slight changes in composition or even impurities which can affect the resulting carrier concentration. For example, over-stoichiometric Mg content can lead to higher values in concentration as the extra Mg acts as a donor. Furthermore, the various methods employed for the synthesis of the bulk materials (SPS, solid state reaction) can have an impact on the microstructure and therefore on the carrier mobility. In fact, the difference in conductivity between that obtained for thin films in this work and the bulk materials, which can be up to two orders of magnitude, can be explained by the significant drop in mobility in the case of thin films. Given the reduction of the grain size to ~100 nm for thin films, the carrier scattering at the grain boundaries is increased, resulting in the decrease of the carrier mobility.

Table 3.4. Comparison between transport properties of un-doped Mg_2Si thin films deposited at HT (463 K) and of bulk Mg_2Si compounds previously reported.

Electrical conductivity (1/Ω·m)	Mobility ($cm^2/V{\cdot}s$)	Concentration ($1/cm^3$)	Ref.
37	6	1.6×10^{17}	this work
50	104	3.0×10^{16}	[28]
1400	204	4.3×10^{17}	[24]
5700	158.5	2.2×10^{18}	[29]

By following the dependence of the electrical conductivities on temperature for Sb-doped Mg_2Si thin films, the increase in electrical conductivity is by a factor of two, with the highest values found for a Sb content of 1.43 at% or, in other words, for x = 0.04. Therefore, the values obtained for the doped Mg_2Si thin films ($2\text{-}3\times10^3\ \Omega^{-1}m^{-1}$) are of the same order as some of the un-doped bulk Mg_2Si compounds [24, 29]. On the other hand, the values obtained for doped thin films and those reported for doped bulk materials ($2\text{-}3\times10^5\ \Omega^{-1}m^{-1}$ [29, 30]) are separated by two orders of magnitude.

Furthermore, a difference of about 30% between the results obtained for thin films deposited at RT and HT is observed, suggesting a positive impact on the electrical conductivity for films that have no distinct texture.

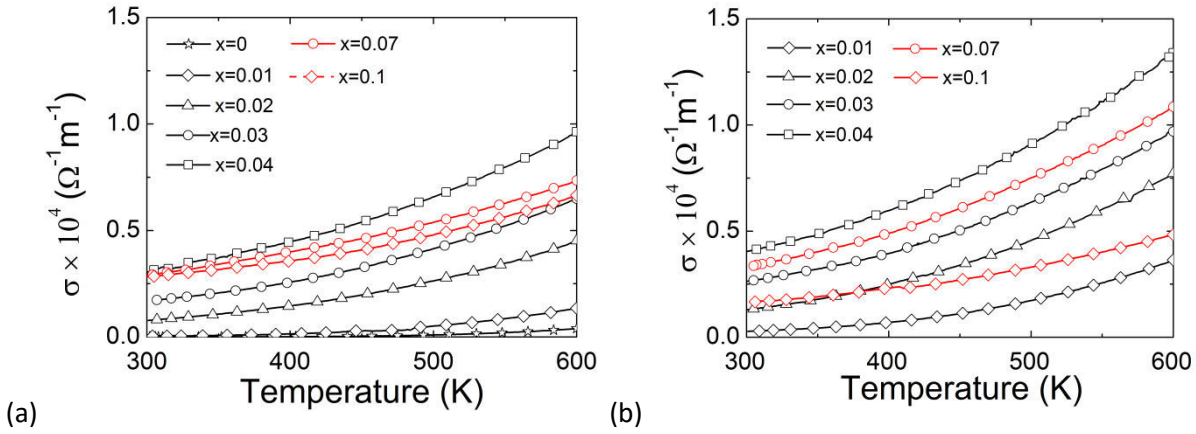

Figure 3.29. Dependence of electrical conductivity with temperature (third cooling cycle measurement) of un-doped and Sb-doped Mg_2Si thin films deposited at (a) RT and (b) HT (463 K).

Another observation that can be inferred from the electrical conductivity measurements is perhaps the solubility limit for Sb. It has been previously noticed for bulk $Mg_2Si_{0.4}Sn_{0.6}$ solid solutions that the carrier concentration and the electrical conductivity reach maximum values for a Sb content close to the solubility limit and then start to decrease due to the excess of Sb as a second phase [21]. Therefore, the evolution of the transport properties with Sb doping can be used as a tool in determining the Sb content for which segregation in a separate phase commences. Therefore, because a Sb phase has not been found in the diffraction patterns of any of the thin films in this work, looking for the change in the electrical conductivity may be useful for finding the solubility limit. Indeed, a drop in electrical conductivity is obvious in Figure 3.29, starting with the film having an Sb content of 0.04. Increasing the Sb content even more leads to a more significant drop in conductivity, implying that the effect of Sb on the transport properties of the film is more pronounced.

In Table 3.5 are presented the transport properties which were measured at RT for Mg_2Si thin films deposited at HT (463 K) and their evolution with the increase of Sb content. As was observed in the study of bulk $Mg_2Si_{0.4}Sn_{0.6}$ solid solutions [21], the carrier concentration reaches a maximum for the Sb content at 0.04 and then it decreases for further doping. The decrease of the carrier mobility is determined by the ion impurity scattering that increases with Sb content. However, although there was a difference in electrical conductivity between thin films and bulk materials due to the decrease of the carrier mobility, the resulting Seebeck coefficients measured for Sb-doped thin films (~110 μV/K) were similar to those obtained in the literature for bulk materials (95 μV/K [28]) or even higher (50 μV/K [29]) for the same Sb content. The Seebeck coefficient is to be determined for RT depositions as well in order to further assess the impact of the texturing on the TE effect.

Table 3.5. Transport properties of Sb-doped Mg_2Si thin films deposited at HT (463 K).

Sb content (x)	Sb content (at%)	Electrical conductivity (1/Ω·m)	Mobility ($cm^2/V·s$)	Concentration ($1/cm^3$)	α (μV/K)
0	0	37	6	1.6×10^{17}	-
0.02	0.6	1100	3	2.4×10^{19}	-
0.03	1	2800	2.5	6.8×10^{19}	-108
0.04	1.4	4800	2	1.5×10^{20}	-110
0.07	2.3	3340	4.2	9.0×10^{19}	-115
0.1	3.6	1300	2.5	3.2×10^{19}	-

Furthermore, preliminary cross-plane measurements of thermal conductivity were performed at room temperature with the 3-ω method as described in Chapter 2. To calculate the thermal conductivity of the Mg_2Si thin films deposited at RT and HT, equation (2.15) was used. For this, the delta parameter was measured as it can be seen in Figure 3.30. The parameter used in the calculation of the thermal conductivity was taken at low voltage frequencies, as in this range the parameter is frequency-independent.

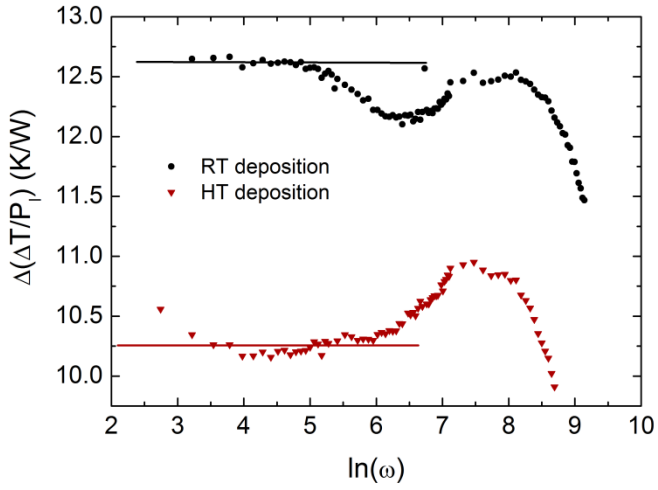

Figure 3.30. Dependence to frequency of the shift in temperature oscillation between thin films deposited at RT and HT with respect to the substrate signal

Accordingly, it was found that the thermal conductivity of the $Mg_{2.014}Si_{0.967}Sb_{0.019}$ thin film deposited at RT is 2.41 W/m·K, while for the film deposited at HT is 3 W/m·K. The values obtained are lower than what is generally obtained for bulk Sb-doped Mg_2Si materials (5-7 W/m·K [24, 28, 31]). One possible reason is the difference in grain size between that obtained in this work and that from indicated reports (although there were no mentions on the microstructure of the bulk materials). The grain size for the RT deposition was approximated to be 100-200 nm from SEM imaging of the

films surface, while the grain sizes for bulk materials may be in the range of µm. Also, it seems that the higher degree of texture in the [220] direction, found for the films deposited at RT, reduces even more the thermal conductivity compared to the film deposited at HT.

3.6 Conclusions

Besides the technological challenges related to the achievement of an integrated TE module based on thin films, the present carried work was useful to highlight several bottlenecks at the level of the materials. In particular, for $Mg_2(Si,Sn)$ thin films, the chemical stability is a critical aspect in regards to the aimed working temperature and, similarly to bulk-based module, the reactivity of the TE material with the insulating or metal substrates and the overall thermo-mechanical behavior of the system was investigated.

Thin films of $Mg_2(Si,Sn)$ solid solutions have been deposited on SiO_2/Si, borosilicate glass, MgO and Ni substrates at different temperatures by microwave plasma-assisted co-sputtering. The depositions resulted in films with an antifluorite and, possibly, a hexagonal crystal structure. Subsequent thermal treatments showed that the films are sensitive to the composition. If the Si content lies between 0.40-0.43, the films go through a structural stabilization process or phase transition, leading to the separation into two cubic phases, suggesting that the as-deposited films are grown in a metastable phase. If however, the Si content is lower, proven in this case for a value of 0.38, the films do not go through any phase separation, marking probably one edge of the miscibility gap in the phase diagram.

The use of multiple substrates during the depositions emphasized the significance of the CTE difference between the $Mg_2(Si,Sn)$ solid solutions and the substrates over the adherence properties of the films after thermal treatments at intermediate temperatures (700 K). However, the deposition temperature also proved to be effective in the amelioration of the film mechanical stability (adherence), relieving the stress inside the films during their growth. Extended heat treatments revealed the reactivity between the $Mg_2(Si,Sn)$ solid solutions and the Ni and SiO_2/Si substrates, which implies that their use in a miniaturized $Mg_2(Si,Sn)$-based TE device would necessitate an additional diffusion barrier. Conversely, borosilicate glass and MgO show both a high mechanical and chemical inertness up to the temperature where $Mg_2(Si,Sn)$ solid solutions show stability.

The electrical properties of the films were investigated, showing values of the electrical conductivities similar to that of undoped bulk materials. The Seebeck coefficient of the films has also been determined at room temperature. As opposed to previous reports on bulk materials, a lower value was found and suggestive of a p-type behavior, but is comparable to that obtained in a previous work on thin films.

The thermal stability of the presented $Mg_2(Si,Sn)$ thin films has been validated up to 653 K for a duration of 168 h. For the films which suffer phase separation, this temperature marks the highest value for which they maintain stability and do not start to decompose in phases of constituent elements. However, it still rests to further inquiry whether the single-phased thin films are more stable at higher temperatures and how their transport properties (Seebeck coefficient and thermal conductivity) evolve with temperature and in comparison with two-phased thin films.

The structural and thermoelectric properties of Sb-doped Mg_2Si thin films have been also investigated, in the search for an alternative to $Mg_2(Si,Sn)$ thin films due to the observed thermal instability of the latter. The deposition of the thin films was performed both at RT and HT. It was determined by XRD measurements that the deposition temperature leads to different structural properties. The films deposited at RT showed a high degree of texture along the [220] direction, while those deposited at HT are grown with crystallites which are more disoriented. As a result, during the characterization of the transport properties, it was determined that the films deposited at HT have slightly higher electrical conductivities (measured in-plane) than the films deposited at RT, suggesting that the degree of texture inside the film can have an effect on the electrical properties. It remains to be seen whether similar impact can be connected to the Seebeck coefficient and thermal conductivity.

The electrical conductivities of Sb-doped Mg_2Si thin film obtained in this work are lower than those obtained on bulk materials, possibly due to the decrease of the grain size, which ultimately leads to an increase carrier scattering at grain boundaries. However, this also leads to the decrease of thermal conductivity (measured cross-plane) to a value more than half than what is usually reported for bulk materials. As for the Seebeck coefficient, it was proved to be similar or even higher than previous results on bulk Sb-doped Mg_2Si compounds.

Furthermore, the solubility limit for the Sb dopant was extracted from the transport properties of the thin films, which showed a variation (decrease of electrical resistivity and carrier concentration) that has previously been observed adjacent to the segregation of Sb in a separate phase. The knowledge of the solubility limit is useful as it is usually the value that delimitates the Sb content for which the most favorable TE properties are obtained.

References

[1] Y. Yamamura and H. Tawara, Energy dependence of ion-induced sputtering yields from monoatomic solid at normal incidence, Atomic Data and Nuclear Data Tables, 62 (1996) 149.

[2] W. Eckstein and R. Preuss, New fit formulae for the sputtering yield, Journal of Nuclear Materials, 320 (2003) 209.

[3] H. Le-Quoc, S. Béchu, S. Populoh, A. Weidenkaff, and A. Lacoste, Thermoelectric properties of thin films of Sb doped $Mg_2Si_{1-x}Sn_x$ solid solutions, Journal of Alloys and Compounds, 546 (2013) 138.

[4] G. A. Roberts, E. J. Cairns, and J. A. Reimer, An electrochemical and XRD study of lithium insertion into mechanically alloyed magnesium stannide, Journal of the Electrochemical Society, 150 (2003) A912.

[5] G. Urretavizcaya and G. O. Meyer, Metastable hexagonal Mg_2Sn obtained by mechanical alloying, Journal of Alloys and Compounds, 339 (2002) 211.

[6] J. Hao, B. Zou, P. W. Zhu, C. X. Gao, Y. W. Li, D. Liu, K. Wang, W. W. Lei, Q. L. Cui, and G. T. Zou, In situ X-ray observation of phase transitions in Mg_2Si under high pressure, Solid State Communications, 149 (2009) 689.

[7] F. Zhu, X. Wu, S. Qin, and J. Liu, A re-investigation on pressure-induced phase transition of Mg2Si, Solid State Communications, 152 (2012) 2160.

[8] H. Le-Quoc, A. Lacoste, S. Miraglia, S. Béchu, A. Bès, and L. Laversenne, MgH_2 thin films deposited by one-step reactive plasma sputtering, International Journal of Hydrogen Energy, 39 (2014) 17718.

[9] Butterworths, http://books.google.com/books?id=Uu5UAAAAMAAJ

[10] L. Berger, Semiconductor materials, Taylor & Francis (1996).

[11] E. N. Nikitin, E. N. Tkalenko, V. K. Zaitsev, A. I. Zaslavskii, and A. K. Kuznetsov, A study of the phase diagram for the Mg_2Si-Mg_2Sn system and the properties of certain of its solid solutions, Journal of Inorganic Materials, 4 (1968) 1656.

[12] S. Muntyanu, E. B. Sokolov, and E. S. Makarov, Study of the Mg_2Sn-Mg_2Si system, Journal of Inorganic Materials, 2 (1966) 870.

[13] M. Sondergaard, M. Christensen, K. A. Borup, H. Yin, and B. B. Iversen, Thermal stability and thermoelectric properties of $Mg_2Si_{0.4}Sn_{0.6}$ and $Mg_2Si_{0.6}Sn_{0.4}$, Journal of Materials Science, 48 (2013) 2002.

[14] J. Bourgeois, J. Tobola, B. Wiendlocha, L. Chaput, P. Zwolenski, D. Berthebaud, F. Gascoin, Q. Recour, and H. Scherrer, Study of electron, phonon and crystal stability versus thermoelectric properties in Mg_2X (X = Si, Sn) compounds and their alloys, Functional Materials Letters, 06 (2013) 1340005.

[15] P. Bellanger, Etude de l'influence des paramètres nano et microstructuraux sur les propriétés thermoélectriques des siliciures de magnésium $Mg_2(Si,Sn)$ de type-n Bordeaux, Ph.D thesis (2014)

[16] A. Kozlov, J. Gröbner, and R. Schmid-Fetzer, Phase formation in Mg–Sn–Si and Mg–Sn–Si–Ca alloys, Journal of Alloys and Compounds, 509 (2011) 3326.

[17] I. H. Jung, D. H. Kang, W. J. Park, N. J. Kim, and S. Ahn, Thermodynamic modeling of the Mg-Si-Sn system, Calphad-Computer Coupling of Phase Diagrams and Thermochemistry, 31 (2007) 192.

[18] V. K. Zaitsev, M. I. Fedorov, E. A. Gurieva, I. S. Eremin, P. P. Konstantinov, A. Y. Samunin, and M. V. Vedernikov, Highly effective $Mg_2Si_{1-x}Sn_x$ thermoelectrics, Physical Review B, 74 (2006) 045207.

[19] T. He and R. J. Cava, Reactivity of MgB_2 with common substrate and electronic materials, Applied Physics Letters, 80 (2002) 291.

[20] Z. J. Liu, S. H. Zhou, X. X. Xi, and Z. K. Liu, Thermodynamic reactivity of the magnesium vapor with substrate materials during MgB2 deposition, Physica C: Superconductivity, 397 (2003) 87.
[21] W. Liu, X. F. Tang, and J. Sharp, Low-temperature solid state reaction synthesis and thermoelectric properties of high-performance and low-cost Sb-doped $Mg_2Si_{0.6}Sn_{0.4}$, Journal of Physics D: Applied Physics, 43 (2010) 085406.
[22] Q. Zhang, J. He, T. J. Zhu, S. N. Zhang, X. B. Zhao, and T. M. Tritt, High figures of merit and natural nanostructures in $Mg_2Si_{0.4}Sn_{0.6}$ based thermoelectric materials, Applied Physics Letters, 93 (2008) 102109.
[23] W. Liu, X. J. Tan, K. Yin, H. J. Liu, X. F. Tang, J. Shi, Q. J. Zhang, and C. Uher, Convergence of Conduction Bands as a Means of Enhancing Thermoelectric Performance of n-Type $Mg_2Si_{1-x}Sn_x$ Solid Solutions, Physical Review Letters, 108 (2012) 166601.
[24] J. Tani and H. Kido, Thermoelectric properties of Sb-doped Mg_2Si semiconductors, Intermetallics, 15 (2007) 1202.
[25] Y. Hayatsu, T. Iida, T. Sakamoto, S. Kurosaki, K. Nishio, Y. Kogo, and Y. Takanashi, Fabrication of large sintered pellets of Sb-doped n-type Mg_2Si using a plasma activated sintering method, Journal of Solid State Chemistry, 193 (2012) 161.
[26] W.-L. Wang, K.-T. Peng, H.-C. Kuo, M.-H. Yeh, H.-J. Chien, and T.-H. Ying, The contact resistance reduction of Cu interconnects by optimizing the crystal behavior of Ta/TaN diffusion barrier, Materials Science in Semiconductor Processing, 27 (2014) 860.
[27] I. C. Noyan, T. C. Huang, and B. R. York, Residual stress/strain analysis in thin films by X-ray diffraction, Critical Reviews in Solid State and Materials Sciences, 20 (1995) 125.
[28] J. Y. Jung, K. H. Park, and I. H. Kim, Thermoelectric Properties of Sb-doped Mg_2Si Prepared by Solid-State Synthesis, IOP Conference Series: Materials Science and Engineering, 18 (2011) 142006.
[29] M. Ioannou, G. Polymeris, E. Hatzikraniotis, A. U. Khan, K. M. Paraskevopoulos, and T. Kyratsi, Solid-State Synthesis and Thermoelectric Properties of Sb-Doped Mg_2Si Materials, Journal of Electronic Materials, 42 (2013) 1827.
[30] T. Nemoto, T. Iida, J. Sato, T. Sakamoto, N. Hirayama, T. Nakajima, and Y. Takanashi, Development of an Mg_2Si Unileg Thermoelectric Module Using Durable Sb-Doped Mg_2Si Legs, Journal of Electronic Materials, 42 (2013) 2192.
[31] L. M. Zhang, C. B. Wang, H. Y. Jiang, and Q. Shen, Thermoelectric properties of Sb-doped Mg_2Si by solid state reaction, Thermoelectrics, 2003 Twenty-Second International Conference on - ICT, (2003) 146.

Chapter 4. Diffusion barriers for bulk material based thermoelectric modules

In order to investigate their properties and potential as diffusion barrier, thin films have been deposited on TE legs. The chosen TE material is n-type Bi-doped $Mg_2Si_{0.4}Ge_{0.6}$ solid solution which is to be incorporated in a TE module for automotive applications. Brazing these Mg_2Si-based materials to metallic electrodes (Al or Ni) using a brazing joint of Al-Si alloy leads to good electrical and mechanical properties of the contacts, but it doesn't stop the onset of diffusion between the legs and the brazing joint which affects the TE properties. To counteract this issue, functional layers need to be deposited on the TE legs that must comply with three aims concerning the interface between the legs and the metallic electrodes:

- Reduce the electrical resistance of the contact, ideally to a value not higher than 10% of the initial resistance of the TE leg
- Have good mechanical properties, implying a good adherence of the deposited films to the TE leg, but also to the brazing joint
- Act as a diffusion barrier, impeding the chemical reaction between the TE leg and the brazing joint at brazing and working temperatures.

Therefore, the purpose of the work presented herein it to ascertain which materials are appropriate to be used, as thin films, in order to optimize the interface between the Mg_2Si-based TE legs and metallic electrodes while abiding to the aforementioned conditions. Two paths have been pursued to attain this objective. The first is based on the deposition of gradient layers that are meant to gradually inverse the composition from the Mg_2Si-based TE legs to a top layer of Ni that is used in the deposition of the potential diffusion barrier. The second path concerns the deposition of a M/Ni bi-layer on the TE legs, where M is a metallic layer (Ti, Ta, W or Cr). For testing their potential as diffusion barriers, the properties of the layers have been investigated after the brazing of the coated $Mg_2(Si,Ge)$ TE legs.

4.1 Deposition of functional layers on Bi-doped $Mg_2(Si,Ge)$ TE legs

The deposition of the films was done using the microwave plasma-assisted co-sputtering method. The substrate holder was placed at a distance of 12 cm from the targets during the deposition and kept either at room temperature (by water-cooling) or at 423 K (by compressed air). Electrically, the substrate holder was either kept at floating potential or at RF self-bias voltage of -20 V. The cleaning process for all surfaces prior to the deposition is described in Chapter 2.

The $Mg_2Si_{0.4}Ge_{0.6}Bi_{0.02}$ legs were supplied by Valeo, synthesized by spark plasma synthesis (SPS) in cuboid shapes with the dimensions of 6×6×4 mm^3. Before the deposition, these legs were polished on one side with the polishing machine Mecatech 334, from Presi, using silicon carbide abrasive grinding papers with grit sizes of P1200 and P4000, followed by polishing using diamond suspension slurry with diamond particles with average diameter of 1 µm.

The legs were then placed in a specially made holder, schematically drawn and shown in Figure 4.1. The leg holder was designed to ensure the deposition of 4 legs, which are to be used for brazing and characterization. To guarantee the thermal transfer and electrical contact between TE legs and the holder during deposition, the joining of the two were done through the lateral surfaces of the TE legs using graphite-based interface pad, Tgon™ 820, from Laird Technologies. The leg holder was then placed on the substrate holder and fastened in place with silver lacquer.

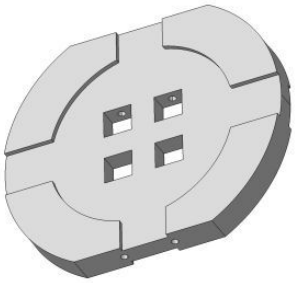

Figure 4.1. Representation in isometric projection of the TE leg holder.

Following the deposition, the n-type $Mg_2(Si,Ge)$ TE legs were brazed at Valeo using the NOCOLOK® flux technology described in Chapter 2. The brazing was done simultaneously on MnSi TE legs (p-type) coated with Ti and Ni layers by a partner of Valeo, in order to be used as a reference. The obtained TE couple is shown in Figure 4.2. After brazing, the electrical and mechanical properties, as well as the chemical stability of the interface between legs and brazing joint, were investigated.

In the following sections, the attempts in finding suitable diffusion barriers for the $Mg_2(Si,Ge)$ TE legs will be presented, which are split into categories according to the strategies employed for this objective. They involve either the deposition of gradient functional layers, where the transition from

the Mg_2-Si-based TE legs to a Ni layer is done gradually with respect to composition, or the deposition of a metallic intermediate layer between the two.

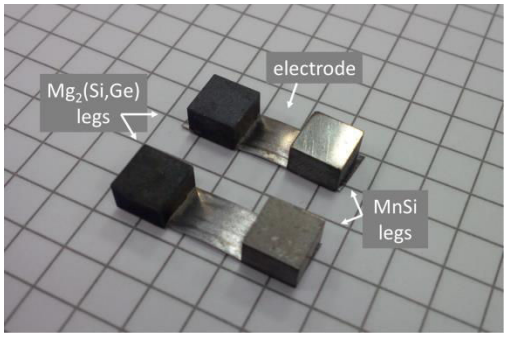

Figure 4.2. TE couple with Mg_2(Si,Ge) and MnSi TE legs after their brazing to metallic electrodes.

4.2 Characterization of (Mg,Si,Ni)/Ni gradient functional layers

The first path to be pursued in the search for proper diffusion barriers was the deposition of gradient functional layers, followed by the deposition of a Ni layer. In past research conducted by Valeo, Ni proved to be a promising candidate due to its reaction with the Al from the brazing joint and the formation of a stable Al-Ni alloy that ensures a good mechanical grip at their interface. Also, the choice of Ni is motivated by its ubiquitous use in the thermoelectric industry. However, it was observed that the resulting Al-Ni alloy does not constitute a good diffusion barrier, allowing the exchange between the legs and the brazing joint.

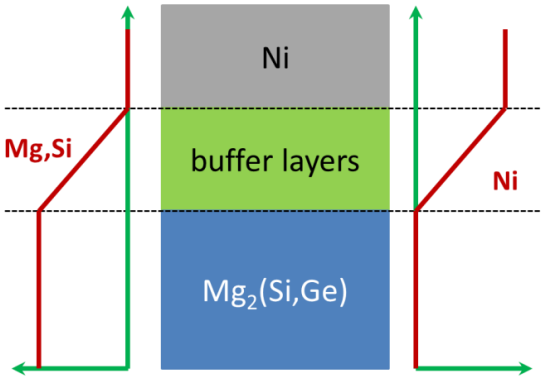

Figure 4.3. Composition profile of the buffer layer between the Mg_2(Si,Ge) TE legs and the Ni layer.

Therefore, to improve the diffusion barrier properties at the interface between Ni and TE legs, the two were separated with a series of layers (buffer layers) that was intended to form a compositional gradient, making a smooth transition from the TE material to Ni. To accomplish this, the co-deposition of Mg, Si and Ni was employed, with a control on the bias applied to the targets such that the ratio of their content is gradually reversing. This is better illustrated visually in Figure

4.3, where the decrease in composition of the Mg and Si content is mirrored by the increase of Ni, until the complete reversal is realized. However, the schematic is an idealization of the process, given that the processes which were attempted in this study implied a variation in composition not as continuous.

Using the basis of the gradient presented in Figure 4.3, multiple attempts have been made for the growth of the buffer layers, which are to be discussed thereafter.

4.2.1 Type 1 buffer layers: buffers made by a sequence of 3 layers

The first type of buffer layers involves three deposited thin films, as shown by the deposition process presented in Table 4.1. The first layer is a Mg_2Si film deposited directly on the $Mg_2(Si,Ge)$ TE leg, the second layer consists of a lower content of Mg and Si, with an increase of Ni and finally, the Ni layer was deposited on top. The intermediate layer between Mg_2Si and Ni was deposited by simply halving the initial voltage biases applied to the Mg and Si targets to ensure a lower content of each. The thickness of the Ni layer was also varied between depositions by doubling the deposition time, from 4 to 8 h, corresponding to a thickness of 1.5 µm and 3 µm, respectively. This was done with the purpose of testing the impact of the thickness on the overall behavior of the deposition after the brazing process. In studies conducted by Valeo, it was established that Ni layers with thicknesses of at least 3 µm were more stable after brazing due to partial reaction with Al from the brazing joint. However, in this study, lower thicknesses were also chosen, to test the possibility of reducing the required process time.

Table 4.1. Deposition process for type 1 buffer layers.

Layers	1	2	3
Mg target bias (V)	135	70	0
Si target bias (V)	600	300	0
Ni target bias (V)	0	600	600
Deposition time (h)	1	2	4 and 8

For easier visualization of the resulting depositions, the layers were grown simultaneously on SiO_2/Si substrates. However, the thicknesses determined from these depositions are approximate, on account of the position of the SiO_2/Si substrates during the deposition (shadow effect coming from proximity to the TE leg holder). The thickness of the Ni layers that are next to be discussed were determined from separate calibration depositions.

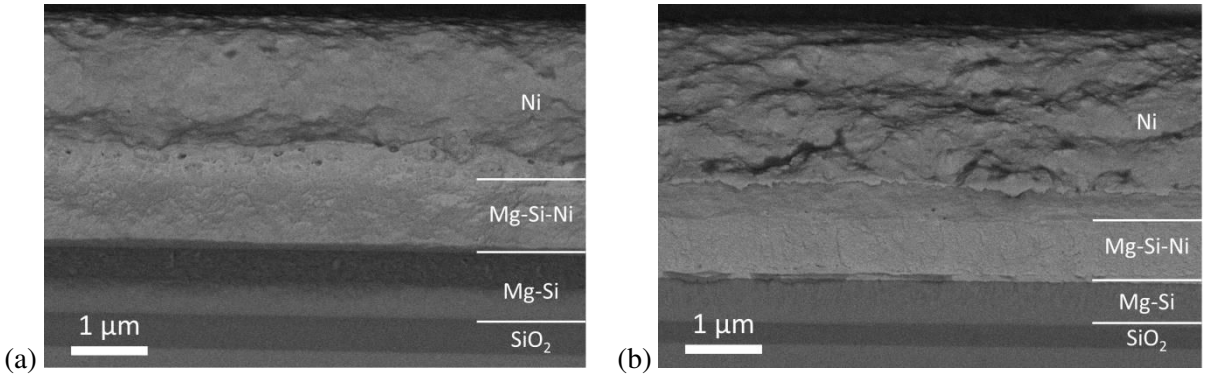

Figure 4.4. SEM cross-sectional images of type 1 buffer layers deposited on SiO_2/Si substrate with Ni layers of (a) 1.5 µm and (b) 3 µm in thickness.

The cross sections of the type 1 buffer layers are shown in Figure 4.4. The three layers are distinctly visible, despite the apparent splitting of the first layer (Mg-Si) into two with different brightness. The visual uncertainty comes from the cleaving of the substrate, which resulted in a less than perfect profile of the layers. Therefore, the rupture of the films perpendicular to the plane of the image resulted in regions with different contrast within the same layer.

The TE legs, deposited with type 1 buffer layers, were then brazed, polished and the interfaces were characterized by SEM and EDX.

For the buffer layers ending with a lower thickness of the Ni cap layer, the composition identification images obtained by EDX mapping after the brazing are shown Figure 4.5.

What becomes evident is that the buffer layers are no longer visible at the interface between the TE leg and the brazing joint, which can only mean that it was completely dissolved inside the brazing joint. This is confirmed by following the Ni content, which shows that the Ni layer lost its cohesion and diffused throughout the brazing joint. The poor qualities of the deposition as a diffusion barrier is also ascertained by the irregularity of the interface between the plot and the brazing joint, especially visible by the diffusion of Mg originating from the TE leg inside the brazing joint. In the Si compositional image, the material that diffuses from the TE leg and the Si corresponding to the Al-Si alloy-based brazing joint cannot be differentiated. For this reason, the Mg compositional images are a better indicator of the diffusion barrier characteristics of the deposited layers.

In the case of the buffer layers with a higher thickness of the Ni layer, the results after brazing are slightly better. Although the layers still lose their cohesion and diffuse inside the brazing joint in many places, the films no longer dissolve completely, as it can be seen in the compositional images from Figure 4.6. Also, as expected, the emergence of the Ni-Al alloy is noticed by comparing the Ni and Al compositional images, while part of the Ni layer still maintains its unity.

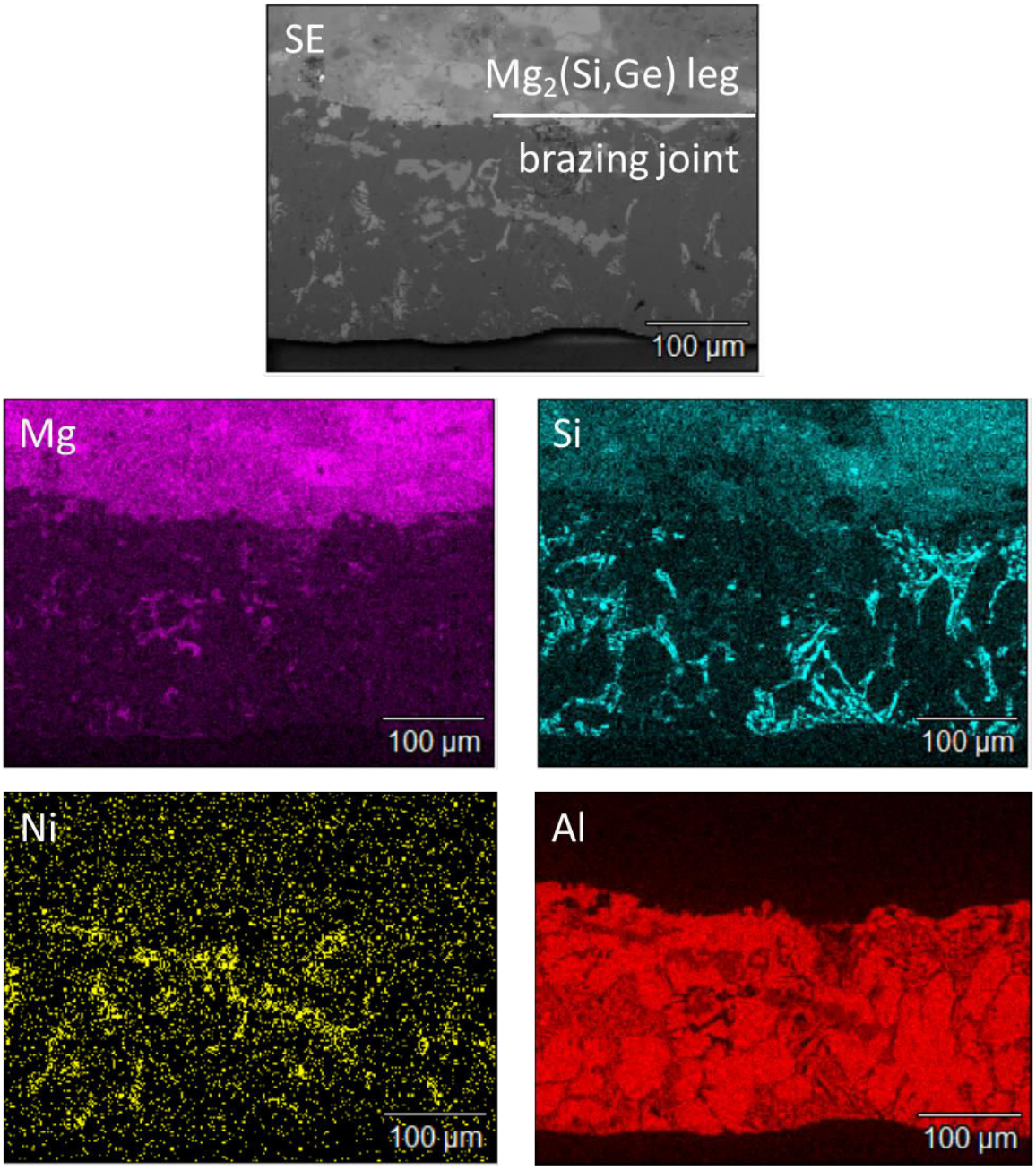

Figure 4.5. Compositional images by EDX mapping of the cross section of Mg_2Si-based TE legs coated with type 1 buffer layers (1.5 µm thick Ni layer), after brazing.

However, there is an additional fracture that spreads throughout the cross section of the sample, which has been determined to be predominantly placed at the interface between the TE leg and the Mg_2Si layer (although it is visible in some regions, as in Figure 4.6, inside the TE leg). Nevertheless, the obvious difference between the two samples deposited with type 1 buffer layers indicate the advantage of using a thicker Ni layer for improving the diffusion barrier properties of the deposition.

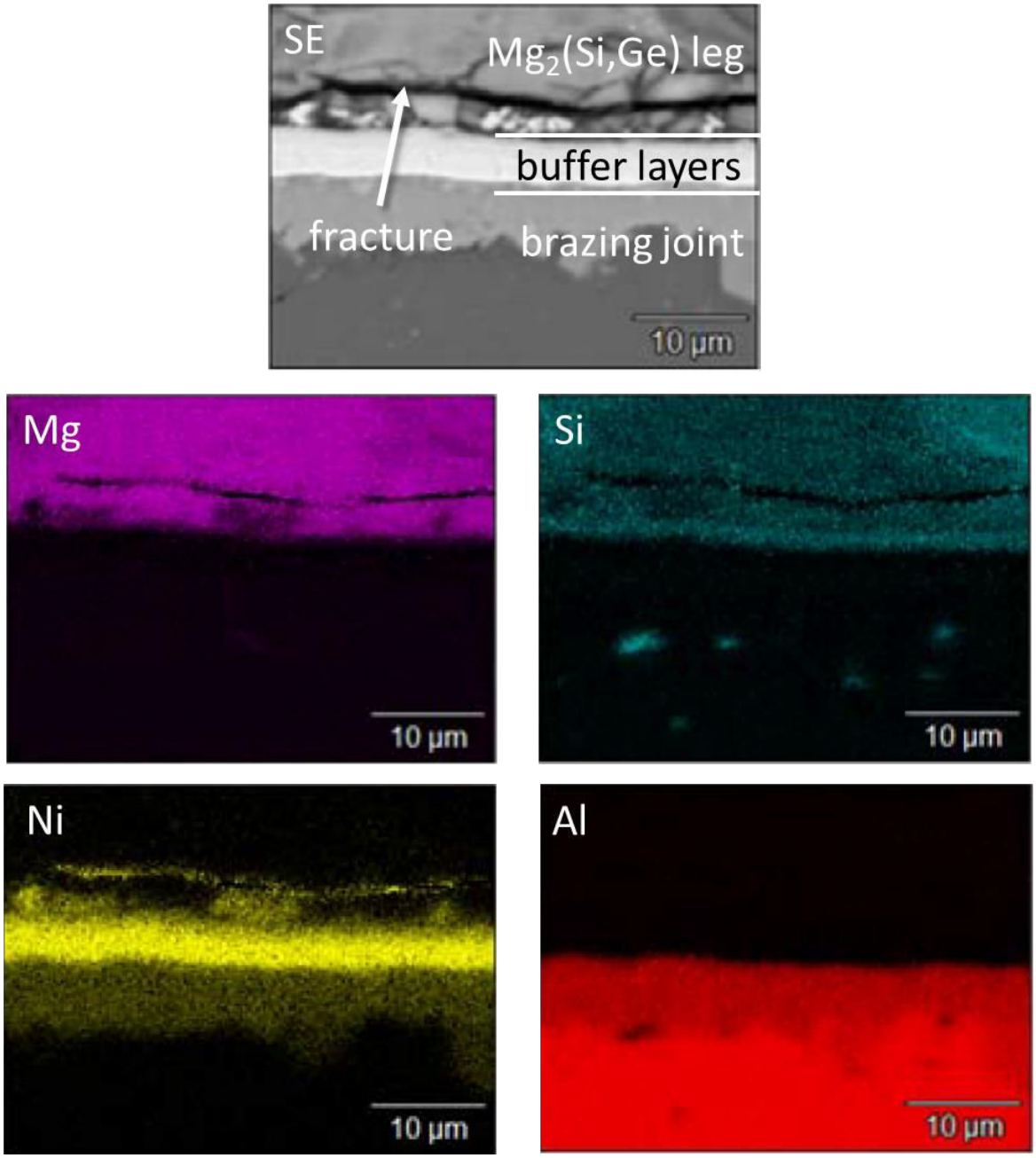

Figure 4.6. Compositional images by EDX mapping of the cross section of Mg_2Si-based TE legs coated with type 1 buffer layers (3 µm thick Ni layer), after brazing.

4.2.2 Type 2 buffer layers: buffers made by a sequence of 8 layers

The poor adherence of the type 1 buffer layers show that type 1 buffer layers do not form a sufficiently gradual transition in composition which is hoped to be more efficient. As a result, a second type of buffer layers was tested, which involves the coating of the $Mg_2(Si,Ge)$ leg with 8 intermediate layers whose compositions are dictated by the bias applied to each set of targets in order to obtain a finer gradient. This was once again accomplished by decreasing the bias applied to Mg and Si targets while increasing the bias applied to the Ni targets, according to the process described in Table 4.2.

Table 4.2. Deposition process for type 2 buffer layers.

Layers	1	2	3	4	5	6	7	8
Mg target bias (V)	100	100	100	100	100	100	50	0
Si target bias (V)	600	600	500	400	300	200	100	0
Ni target bias (V)	0	50	50	100	150	200	300	600
Deposition time (h)	1	0.5	0.5	0.5	0.5	0.5	0.5	4 and 8

To determine the properties of the buffer layers between the TE legs and the brazing joint after the brazing process, two type 2 buffer layers depositions were performed, by varying once again the thickness of the Ni layer from 1.5 µm to 3 µm.

In Figure 4.7 are shown the resulting layers deposited on SiO_2/Si substrate. The cleaving of the substrate leads at times to unpredictable fracturing of the deposited layers, highlighted in Figure 4.7.a by the inhomogeneous cut of the Ni layer compared to Figure 4.7.b). Also, although the buffer layers are clearly distinguished, their number does not seem to add up to 8 layers. This is caused by the subtle changes in the bias values during the deposition of the first layers.

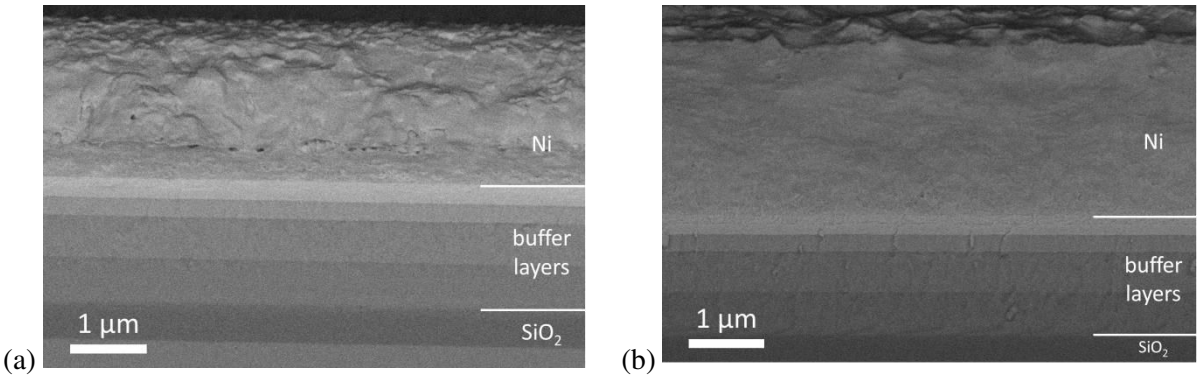

Figure 4.7. SEM cross-sectional images of type 2 buffer layers deposited on SiO_2/Si substrate with Ni layers of (a) 1.5 µm and (b) 3 µm in thickness.

After the TE legs were brazed and polished, the properties of the buffer layers as diffusion barriers were characterized, as before, by EDX mapping of their cross section. For the sample with lower Ni thickness, the same result has been obtained as for type 1 buffer layers, namely the films have diffused in their entirety in the brazing joint just as it was observed in Figure 4.5. This result enforces the poor diffusion barrier properties (at least to withstand the current brazing process) for the layers with insufficient thickness of the Ni layer.

On the other hand, type 2 buffer layers with a 3 µm-thick Ni layer showed promising results, as can be observed in Figure 4.8. Here it is noticed that the buffer layers did not dissolve in the brazing joint during the high temperature process and the Ni layer has only partially reacted with the joint in the formation of the protective and stable unidentified Ni-Al alloy.

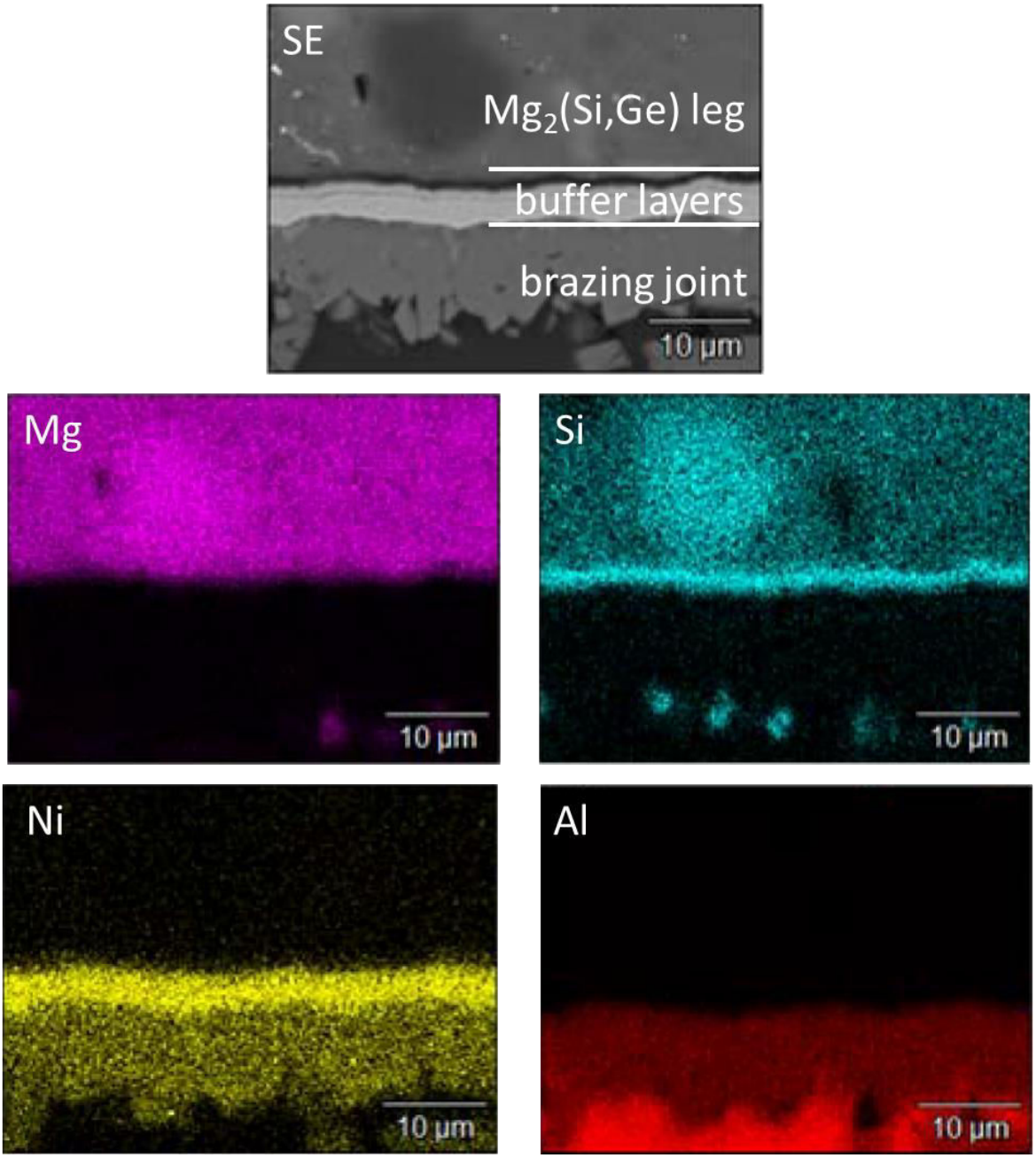

Figure 4.8. Compositional images by EDX mapping of the cross section of Mg_2Si-based TE legs coated with type 2 buffer layers (3 µm thick Ni layer), after brazing.

The dark layer which is observed in the SE image does not represent a fracture or a case of delamination, but it is solely due to the compositional contrast between the TE leg and the deposited films. This is reflected in the Si compositional image, where the Si abundant deposited layers overlap with the dark layer in the previous image.

Nevertheless, there have been indeed some regions along the cross section where a distinct fracture is visible inside the buffer layers. This is depicted in Figure 4.9, an SE-SEM image of a

section with such description. This causes the detachment of the layers in some places, which naturally leads to local diffusion between the TE legs and the brazing joint.

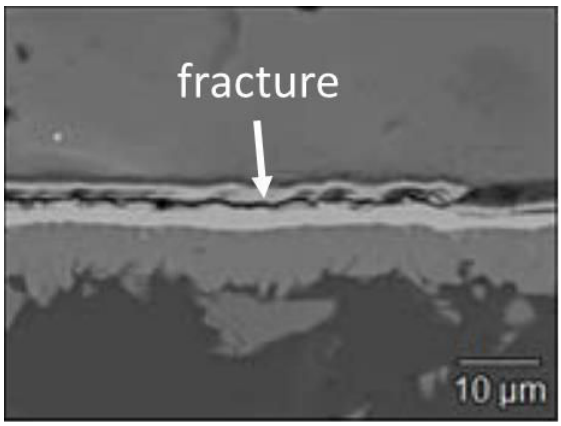

Figure 4.9. SE-SEM cross-sectional image of type 2 buffer layers deposited on Mg_2Si-based TE legs with Ni layer of 3 µm in thickness, after brazing process.

The most likely explanation is the sudden transition from high to low Mg and Si content during the deposition process, which could have deteriorated the mechanical properties of the interface. In Figure 4.10 is shown a close-up of the cross section of the type 2 buffer layers deposited on SiO_2/Si substrate. By comparing the fracture noticed after brazing with the cross section of the film as-deposited, it becomes discernible that the placement of the fracture coincides with that of the layer where the bias applied to the Mg and Si targets are lowest (the demarcation line visible in Figure 4.10).

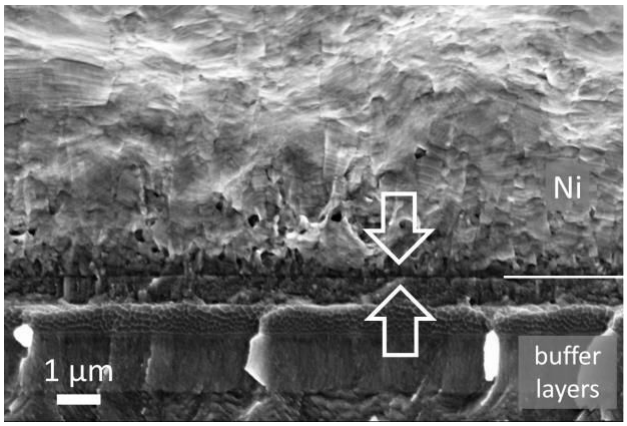

Figure 4.10. SEM cross-sectional image of type 2 buffer layers deposited on SiO_2/Si substrate with Ni layer of 3 µm in thickness.

Overall, it was seen that the increase in thickness of the Ni layer has enhanced the properties of the interface as a diffusion barrier between the TE legs and the brazing joint. Also, between the two

types of buffer layers, the most promising is type 2, which is the more stable and may require just a slight improvement of the mechanical properties by changing the deposition process.

4.2.3 Types 3-4 buffer layers: buffers made by a sequence of 5 or 6 layers

In the attempt to improve the properties of the presented buffer layers, the deposition process was changed in order to obtain a more gradual transition between the last layers. As a result, the deposition processes shown in Table 4.3 were used, where the composition of each layer is also indicated. It is worth mentioning that some changes brought to the deposition setup led to the increase of the deposition rate of Ni, translating into the deposition of a 3 µm-thick Ni layer in 5 h instead of 8 h, as was previously shown.

Table 4.3. Deposition process for types 3 and 4 buffer layers.

	Layers	Mg_2Si	1	2	3	4	Ni
Type 3 buffer layers	Mg target bias (V)	135	250	350	250	-	0
	Si target bias (V)	600	600	500	300	-	0
	Ni target bias (V)	0	100	200	200	-	600
	Deposition time (h)	1	0.5	0.5	0.5	-	5
Type 4 buffer layers	Mg target bias (V)	135	250	350	250	100	0
	Si target bias (V)	600	600	500	300	200	0
	Ni target bias (V)	0	100	200	300	400	600
	Deposition time (h)	1	0.5	0.5	0.5	0.5	5
	Mg (at%)	66.6	69	69.6	53.5	0.2	0
	Si (at%)	33.4	23	15.2	12.7	17.2	0
	Ni (at%)	0	8	15.2	33.8	82.6	100

In Figure 4.11 we can see the cross sectional ESB-SEM images of the resulting films deposited on SiO_2/Si substrate with the buffer layers being clearly distinguished. However, the type 3 buffer layers present an abrupt transition from the intermediate layers and to the Ni layer. In order to overcome this issue, an additional layer was added in the deposition of type 4 buffer layers. Indeed, from the standpoints of composition and microstructure, the resulting film seems to offer a smoother transition (Figure 4.11.b) than what was previously obtained.

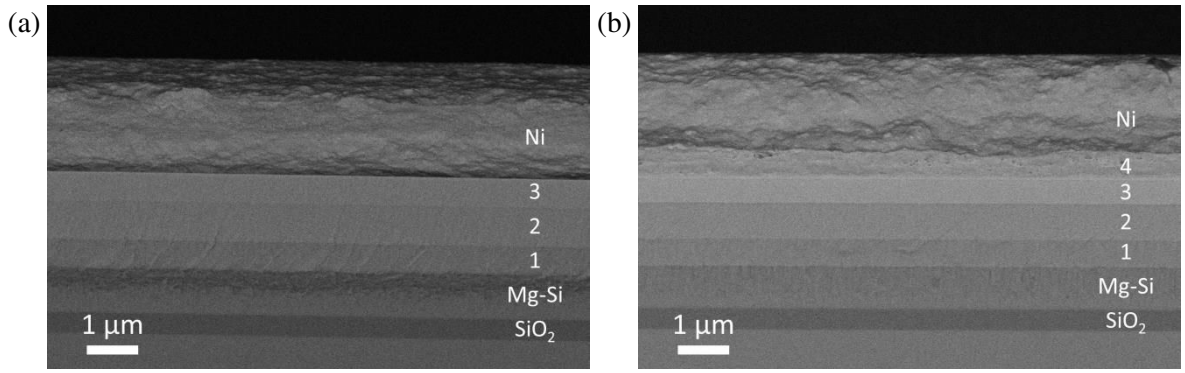

Figure 4.11. ESB-SEM cross-sectional images of (a) type 3 and (b) type 4 buffer layers deposited on SiO_2/Si substrate.

Before brazing, the films showed good adherence to the TE legs. However, despite the expectations, both type 3 and type 4 buffer layers led to the same results after brazing, which entailed the complete dissolution of the buffer layers in the brazing joint. This clearly indicates that the previous attempts have not been improved by the steps taken in this test, enforcing the necessity to improve the properties of the interface by new means.

4.2.4 Type 4 buffer layers with Ti layer

Taking into account the smoother transition in composition brought by type 4 buffer layers, attempts were made to improve the likelihood for it to work as a diffusion barrier. For this reason, due to the efficiency of Ti as a diffusion barrier, previously recognized through the results obtained after brazing MnSi plots coated with layers of Ti and Ni (tested and confirmed by Valeo), it has been decided to incorporate it in the deposition of the buffer layers on the $Mg_2(Si,Ge)$ TE legs. This was done with the hope that it will stop the dissolution of the buffer layers in the brazing joint and perhaps improve the mechanical properties of the contact.

The deposition process that was employed can be found in Table 4.4, where the Ti layer was placed in the middle of the top Ni layer.

Table 4.4. Deposition process for type 4 buffer with Ti layer.

Layers	Mg_2Si	1	2	3	4	Ni	Ti	Ni
Mg target bias (V)	135	250	350	250	100	0	0	0
Si target bias (V)	600	600	500	300	200			0
Ni target bias (V)	0	100	200	300	4000	600	0	600
Ti target bias (V)	0	0	0	0	0	0	600	0
Deposition time (h)	1 h	0.5	0.5	0.5	0.5	2.5	3	2.5

The deposition of Ti (~600 nm) was done by biasing a target, with a diameter of 50 mm, placed in the center of the target holder (description found in Chapter 2).

The cross-section of the film is shown in Figure 4.12. The placement of the Ti layer inside the Ni layer was done with the thought that the three top layers (Ni/Ti/Ni) might together increase the probability for them to act as a diffusion barrier.

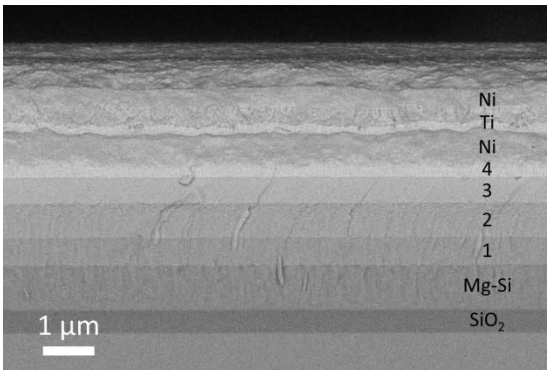

Figure 4.12. Cross-sectional SEM images of type 4 buffer layers with Ti layer deposited on SiO_2/Si substrate.

However, after the brazing of the coated TE leg, the buffer layers once again went through a complete dissolution inside the brazing joint.

The failure of the Ti layer as a diffusion barrier might be explained by the diffusion of Ni in Ti. This can be seen in Figure 4.13, where we have the cross-section of the buffer layers deposited on a TE leg after it was subjected through the same thermal treatment as the one employed at Valeo during the brazing process. The Ti layer appears to be irregular, with some inclusions where it seems that diffusion between Ni and Ti might have taken place.

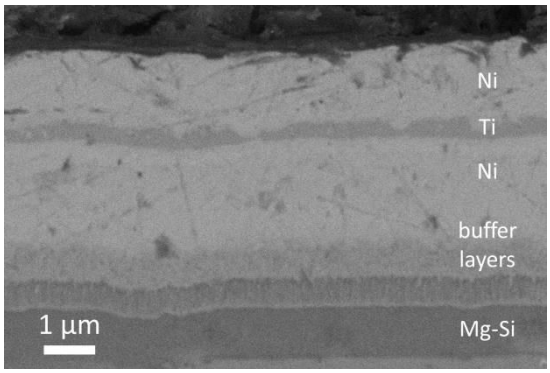

Figure 4.13. ESB-SEM cross-sectional image of type 4 buffer layers with Ti layer deposited on Mg_2Si-based TE legs, after TT.

In literature it was reported that for Ni-Ti multilayers, there are two diffusion regimes: slow, up to 493 K, and fast, at higher temperatures [1]. However, this issue has not been observed in the case

of Ti/Ni layers deposited on MnSi plots, which show, after brazing, an intact Ti layer. An example of this effectiveness can be seen in Figure 4.14, where the compositional images of the coated MnSi TE legs are shown after the same brazing process. The deposition on the MnSi was done by dc magnetron sputtering with a result of two layers with thicknesses of 1 µm (Ti) and 5 µm (Ni). Therefore, the use of Ti and Ni might still prove to be an option as the diffusion barrier in the right deposition conditions.

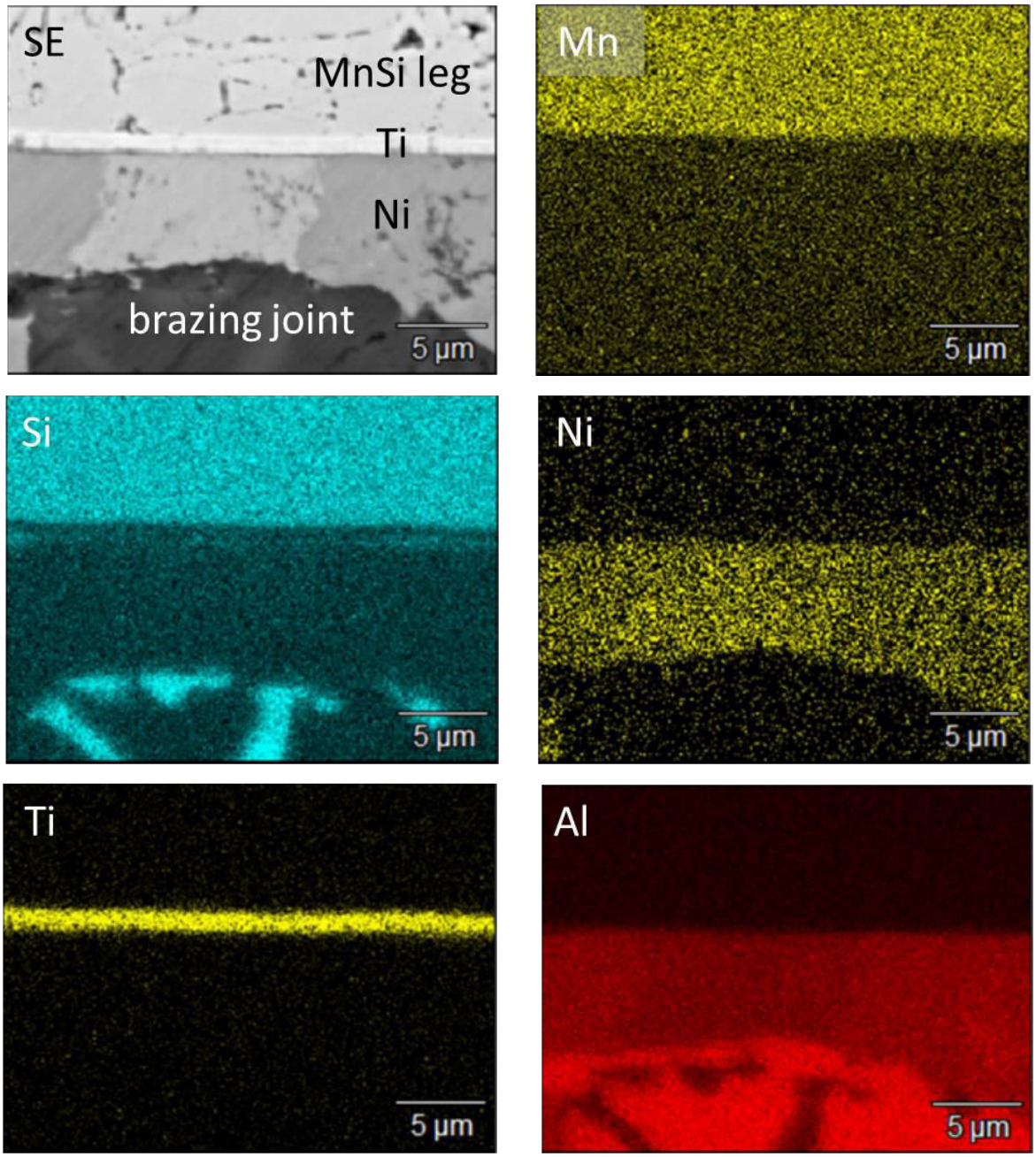

Figure 4.14. Compositional images by EDX mapping of the cross section of MnSi TE legs coated with Ti (1 µm) and Ni (5 µm) layers (supplied by Valeo), after brazing.

As a follow-up, another attempt has been pursued, with the Ti layer preceding the Ni film, instead of being placed between two Ni layers (deposition process described in Table 4.5).

Table 4.5. Deposition process for type 4 buffer with Ti layer (II).

Layers	Mg_2Si	1	2	3	4	Ti	Ni
Mg target bias (V)	135	250	350	250	100	0	0
Si target bias (V)	600	600	500	300	200		0
Ti target bias (V)	0	100	200	300	400	600	0
Ni target bias (V)	0	0	0	0	0	0	600
Deposition time (h)	1	0.5	0.5	0.5	0.5	3	5

This was done assuming that the thicker Ni film separating the Ti layer and the brazing joint (3 µm instead of 1.5 µm) might improve the interface, with the partial alloying between Al and Ni in the top layer.

However, the subsequent brazing of the deposited legs led once again to the partial dissolution of the buffer layers inside the brazing joint.

Moreover, the integrity of the buffer layers is further worsened by the appearance of gas bubbles, which at the time were unexplainable. The bubbles seem to have grown only during the brazing and according to their position noticed in the cross section of the interface, they appeared at the surface of the legs under the deposition. This led eventually to the conclusion that the surface of the leg was contaminated prior the deposition, suggesting insufficient cleaning of the legs, although the regular process was used for all samples (sonic bath for 10 minutes in acetone and then ethanol; followed by in-situ cleaning via ion bombardment in plasma for 10 minutes with the substrate RF biased at -30 V). The most probable cause of the unwanted contamination is either the resin used for fixing the TE legs during their polishing or remnants from the slurry of diamond particles used during the same polishing process (or a combination of both).

Measures have been taken on all subsequent samples to avoid the presence of the contaminants by making the cleaning process more thorough. For example, the sonic baths were not only prolonged from 5 to 20 minutes, but also repeated in fresh acetone and ethanol with a total of 3 cycles. The ionic bombardment of the substrate was also prolonged from 10 to 30 minutes.

Overall, it was seen that the deposition of presented buffer layers, although promising in some cases in which the Ni layer has a sufficiently high thickness (3 µm), did not lead to the aimed diffusion barrier properties at the interface between the $Mg_2(Si,Ge)$ TE legs and the brazing joint.

4.3 Characterization of two-layered diffusion barriers (Ti/Ni, Ta/Ni, W/Ni, Cr/Ni)

In light of the obtained results, presented in the previous section, a second path was pursued in finding better diffusion barrier characteristics at the TE leg-brazing joint interface. This path involves the deposition of an additional layer between the TE legs and the Ni layer directly on the $Mg_2(Si,Ge)$ TE legs, based on materials that have been known to be effective as diffusion barriers in the integrated circuit technology.

4.3.1 Type 1 functional layers: Ti/Ni

What was next tried is the deposition of Ti and Ni layers directly on the TE legs. This was not previously attempted on account of the CTE difference between Ti (8.6×10^{-6} 1/K) and the underlying TE leg (15×10^{-6} 1/K). However, recent depositions performed by magnetron sputtering on $Mg_2(Si,Ge)$ TE legs within another project in partnership with Valeo showed promise. Although their layers still showed local disruption due to the diffusion between the leg and the brazing joint, the results (good adhesion and diffusion barrier characteristics) were encouraging. To this effect, the deposition process presented in Table 4.6 was employed directly on the TE legs.

Table 4.6. Deposition process of type 1 functional layers (Ti/Ni).

Layers	Ti	Ni
Ti target bias (V)	600	0
Ni target bias (V)	0	600
Deposition time (h)	3 and 5	5 and 8

However, as it can be seen in Figure 4.15, the current deposition did not perform as expected. The Ni has dispersed throughout the brazing joint, showing poor adherence, and the Ti layer, despite apparent conservation of its cohesion, did not stop the diffusion between the leg and the brazing joint. This diffusion is clearly attested by the irregularity of the interface, the Al 'pockets' inside the TE leg and the spread of Mg in the brazing joint.

Two more depositions were prepared involving the Ti/Ni bi-layer, while changing the deposition process in order to either have a more energetic film growth or conditions closer to those found in magnetron sputtering. The former deposition was performed with the substrate temperature lowered from 423 K to RT, but with a RF self-bias of -20 V applied to the substrate instead of being kept at floating potential. This was done to increase the surface energy, for enhancing the adatoms surface diffusion and perhaps result to denser films and also to a better adhesion. The second deposition was also performed at RT, but also by increasing the Ar pressure from 1 mTorr to 4 mTorr and decreasing the distance between the targets and the substrate from 12 cm to 8 cm. This was done

with the aim for replicating, more or less, the conditions found in dc magnetron sputtering where the energy of the sputtered atoms is lower than that found during the regular deposition process used in this project at 1 mTorr. Therefore, the increase of the Ar pressure during deposition leads to an increase in particle thermalization, reducing the energy of the deposited atoms.

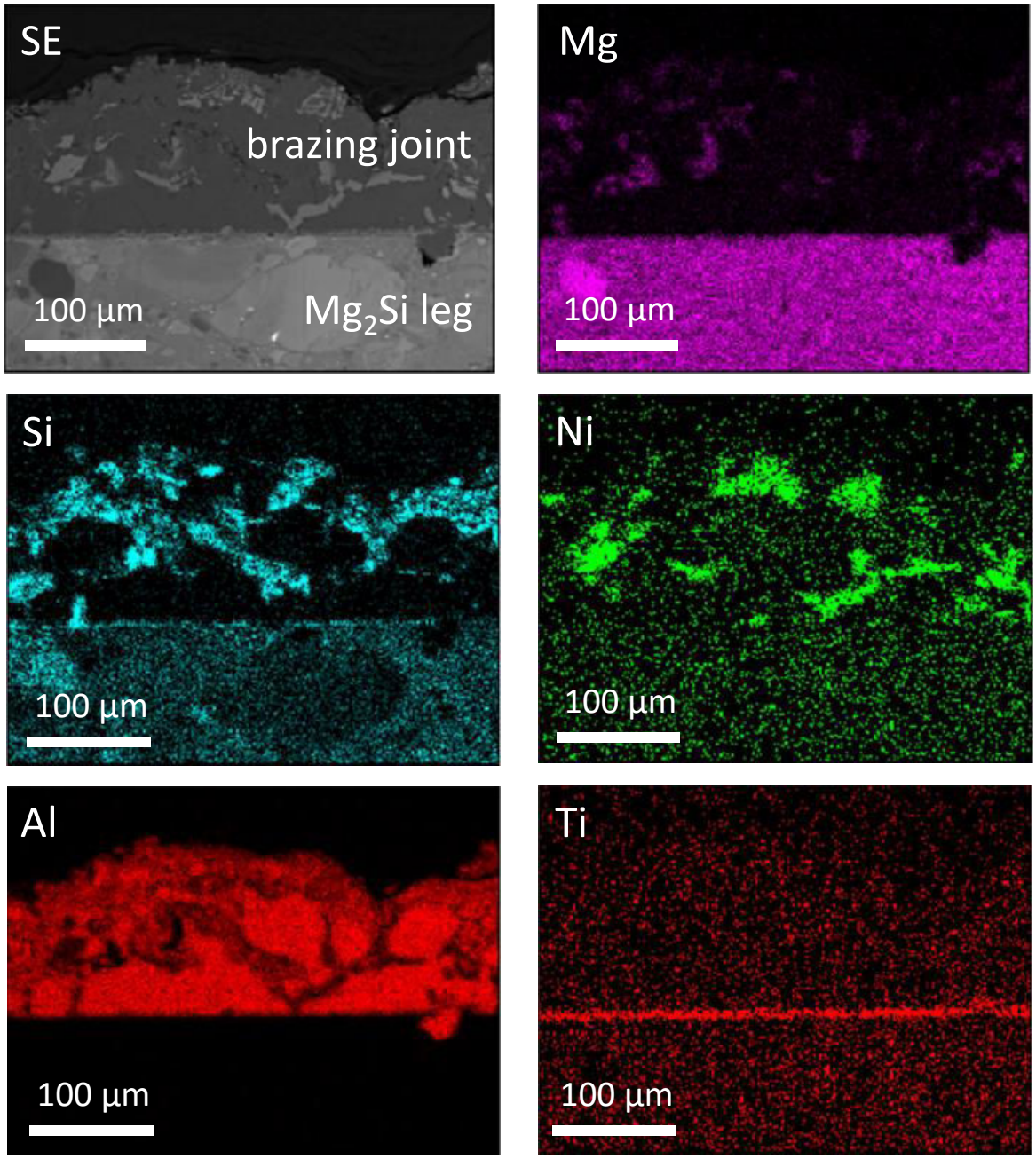

Figure 4.15. Compositional images by EDX mapping of the cross section of Mg_2Si-based TE legs coated with type 1 functional layers Ti/Ni, after brazing.

The deposition time of the two layers was additionally increased in order to obtain higher thicknesses (1 µm-thick Ti layer and 4.5 µm-thick Ni layer).

The results obtained after brazing are exemplified in Figure 4.16 for the deposition at higher Ar pressure. The Ti and Ni layers are still intact, with the exception of very few areas where the leg-

joint diffusion has broken through the films. Furthermore, the two layers show good diffusion barrier properties, proven by the lack of reaction between the brazing joint the TE leg. However, the adherence of the Ti/Ni layers to the TE leg is poor, with a fracture that separates them being noticed throughout the cross section. This leads to the conclusion that the results obtained for the films deposited by dc magnetron sputtering were not reproduced and the residual stresses at the interface (along with thermal stresses on account of CTE difference) lead to the detachment between the films and the TE leg.

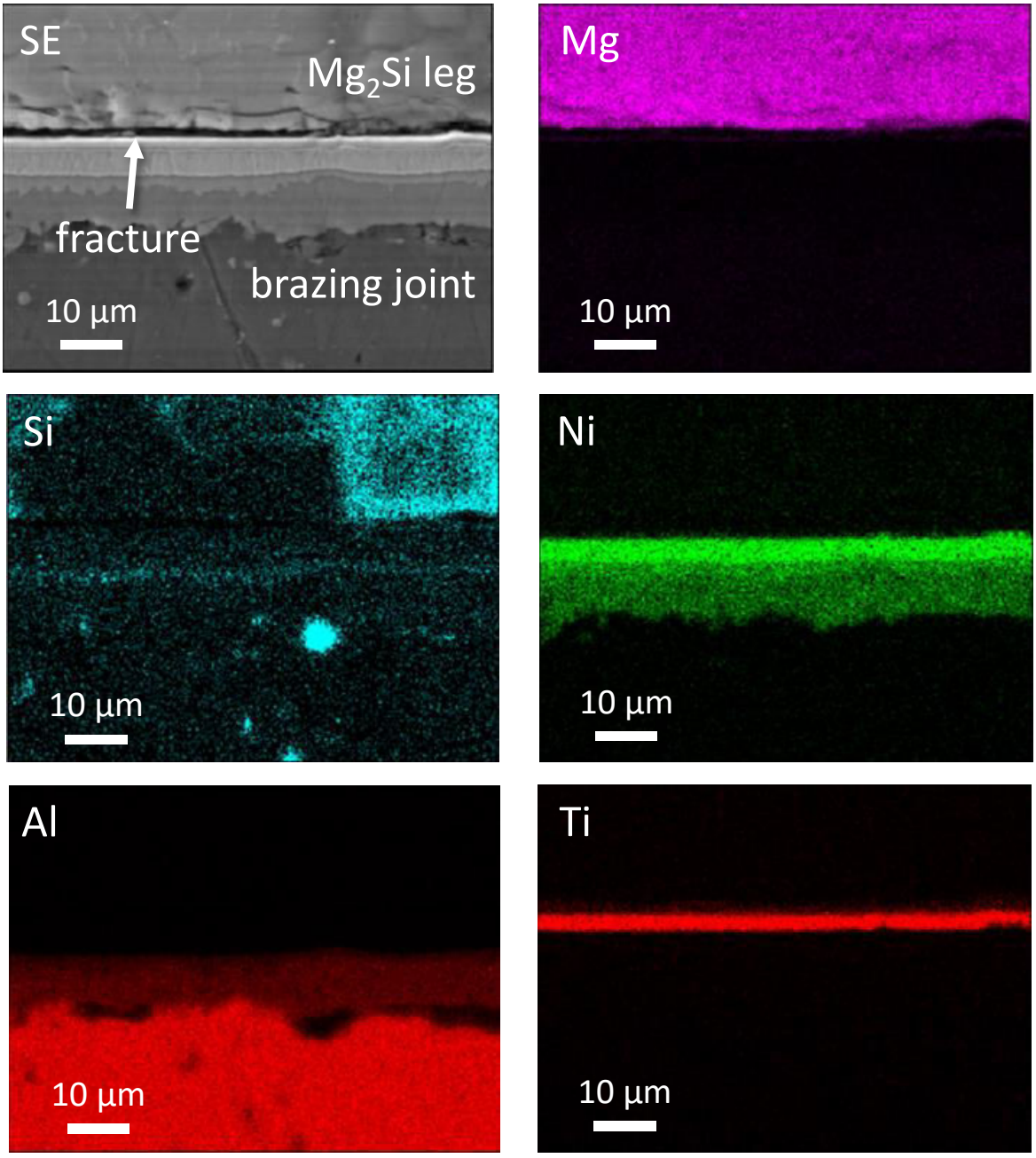

Figure 4.16. Compositional images by EDX mapping of the cross section of Mg_2Si-based TE legs coated with type 1 functional layers (Ti/Ni), Ar pressure at 4 mTorr, after brazing.

4.3.2 Type 2 functional layers: Ta/Ni

In the search of new materials suitable for tuning the interface properties between the TE leg and the brazing joint, Ta stands out as an auspicious candidate, based on previous work done in finding diffusion barriers against Cu metallization [2-4]. For this reason, it was selected in current work to test its potential as diffusion barrier for the aimed purposes. The deposition process is shown in Table 4.7.

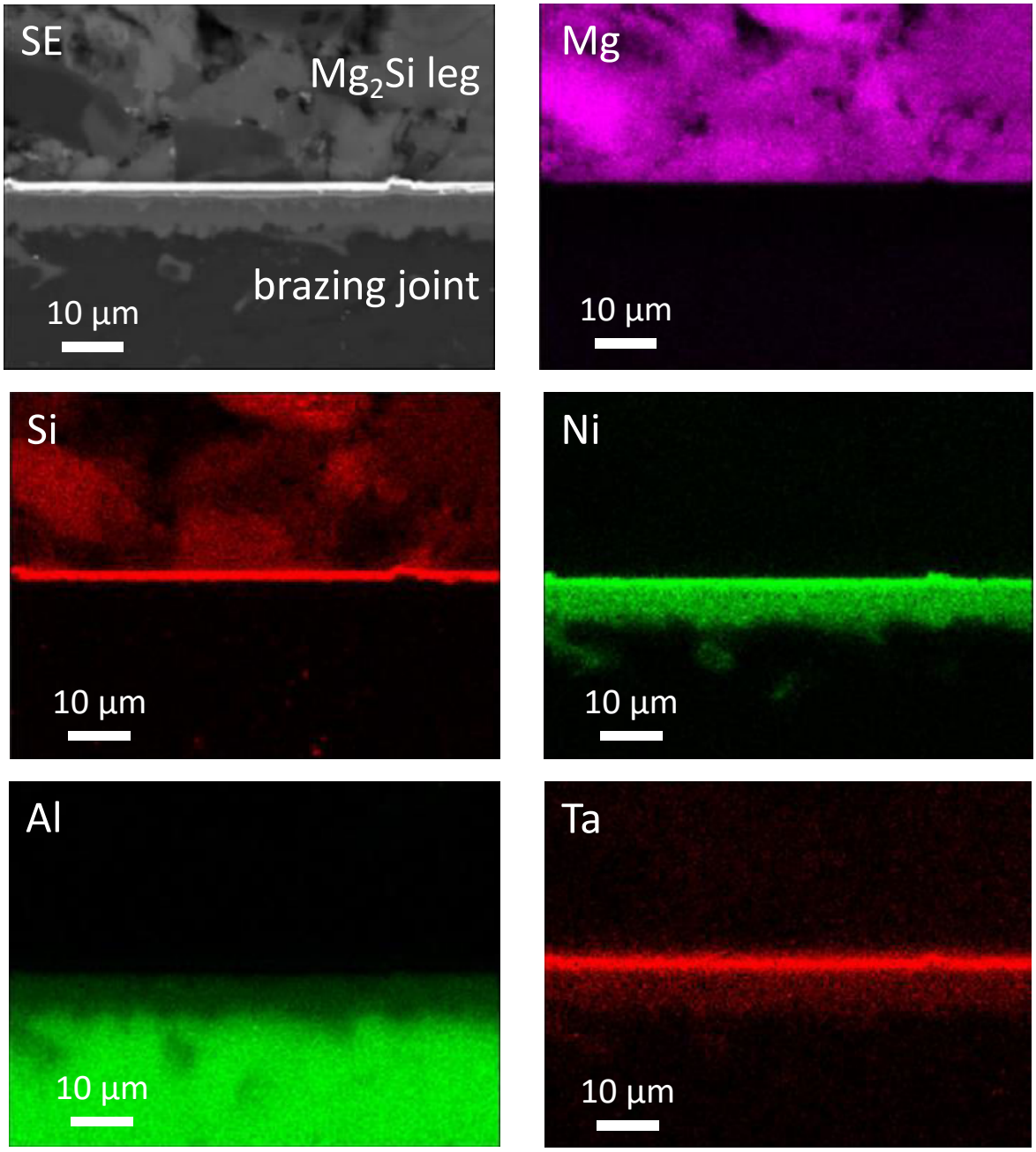

Figure 4.17. Compositional images by EDX mapping of the cross section of Mg_2Si-based TE legs coated with type 2 functional layers (Ta/Ni), after brazing.

Table 4.7. Deposition process for type 2 functional layers (Ta/Ni).

Layers	Ta	Ni
Ta target bias (V)	600	0
Ni target bias (V)	0	600
Deposition time (h)	5	8

The results after the brazing process are also shown in Figure 4.17. All the compositional images suggest both a good adherence of the Ta/Ni layers to the leg and very good diffusion barrier characteristics, making it the most promising deposition as of yet. One unknown extracted from these images is the reason behind the formation, via diffusion, of the thin layer of Si at the surface of the TE leg. It suggests the possible formation of a Ta-Si alloy that may assist to the mechanical and chemical stability of the interface. For this reason, further investigations are necessary to explain the segregation of Si at the surface of the leg and to clarify the means through which Ta seems to be adequate for reaching the objectives of this project.

These results have been reproduced in subsequent deposition and brazing processes. Despite the lack of electrical resistance measurements at the moment, the Ta/Ni layers may be considered a viable contender as a diffusion barrier for $Mg_2Si_{0.6}Ge_{0.4}Bi_{0.02}$ legs against the brazing joint in a TE module.

4.3.3 Type 3 functional layers: W/Ni

Still, despite finding the material as a good diffusion barrier, Ta is considered as expensive, which has an impact on its general use in practical (and industrial) applications. Therefore, on cost grounds, other options were investigated based on materials that have proved to be efficient for integrated circuit technology. Thus, the choice of W was made, based on its use as a constituent element in various diffusion barriers [5] and due to its lower costs in acquisition. Initially, in order to replicate the same deposition process as the one used for Ta, 1 µm-thick W layer was deposited, followed by the deposition of the Ni layer (4.5 µm).

Table 4.8. Deposition process of type 3 functional layers (W/Ni).

Layers	W	Ni
W target bias (V)	600	0
Ni target bias (V)	0	600
Deposition time (h)	1	8

However, this has led to the complete delamination of the layers even during the deposition. This can be put on account of the high compressive stress determined by the atomic peening

mechanism that may occur for a deposition pressure as low as 1 mTorr [6]. To avert this issue, a thinner W film (0.2 µm) was deposited instead, according to the deposition process from Table 4.8.

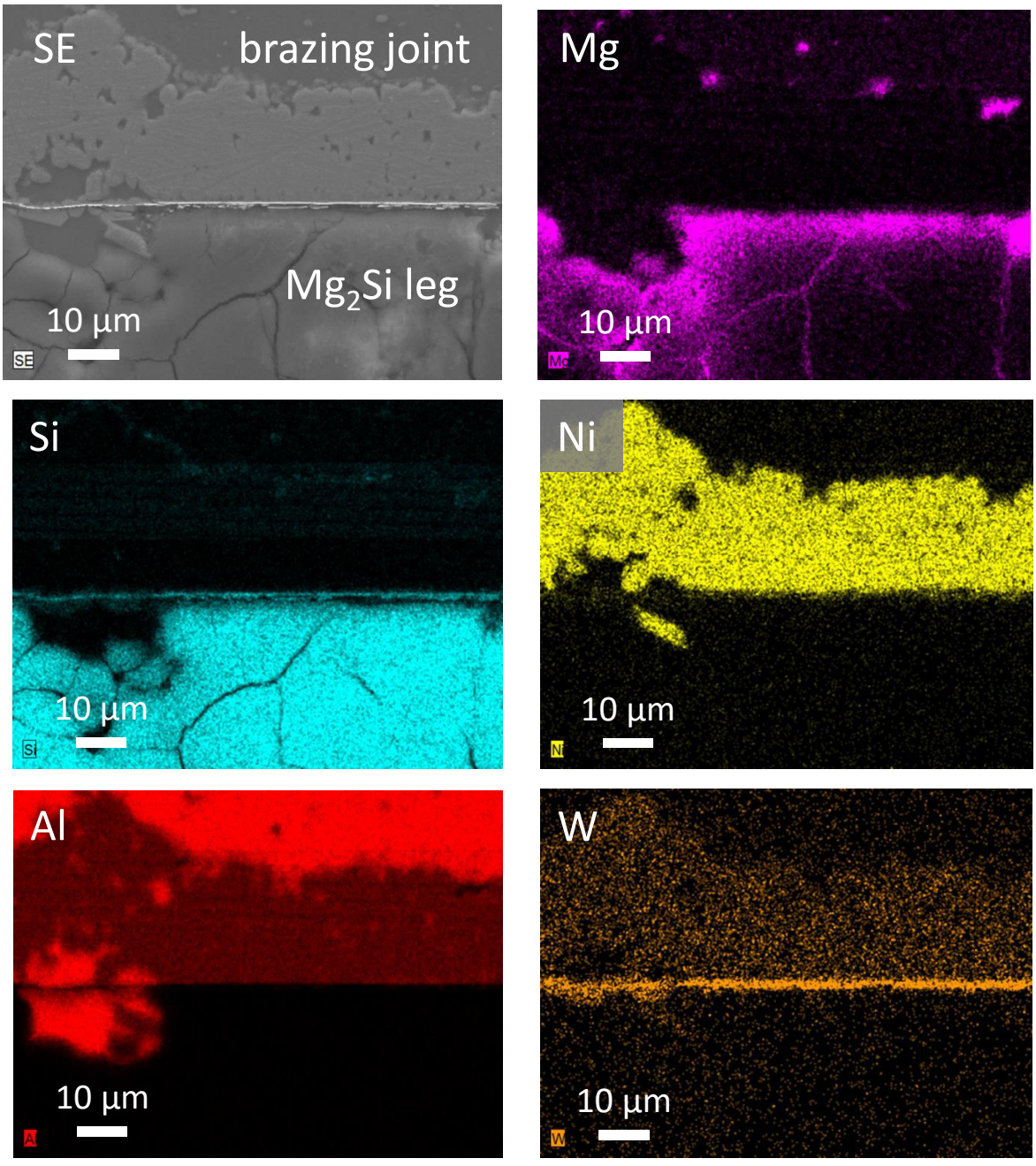

Figure 4.18. Compositional images by EDX mapping of the cross section of Mg_2Si-based TE legs coated with type 3 functional layers (W/Ni), after brazing.

Although overall, the W/Ni bi-layer proves to make a good diffusion barrier, there are regions where the barrier is broken through and the diffusion of Al inside the TE leg is noticed, as shown in Figure 4.18. Despite that these regions are not numerous, their existence, nonetheless, indicate that the W layer of 200 nm is not sufficient to stop the diffusion in a definitive manner. However, as was seen

before, increasing the thickness is not an option, unless methods are employed for reducing the stress during the deposition, e.g. increasing the deposition pressure to reduce the kinetic energy of the sputtered atoms.

4.3.4 Type 4 functional layers: Cr/Ni

One last attempt in finding a more cost effective material to be used as a diffusion barrier is by the deposition of a Cr thin film between the TE leg and the Ni layer. The choice was based as well on the use of Cr in the synthesis of a $CrSi_2$-based diffusion barrier that was specifically tested for Mg_2Si TE legs [7], as was mentioned in Chapter 1.

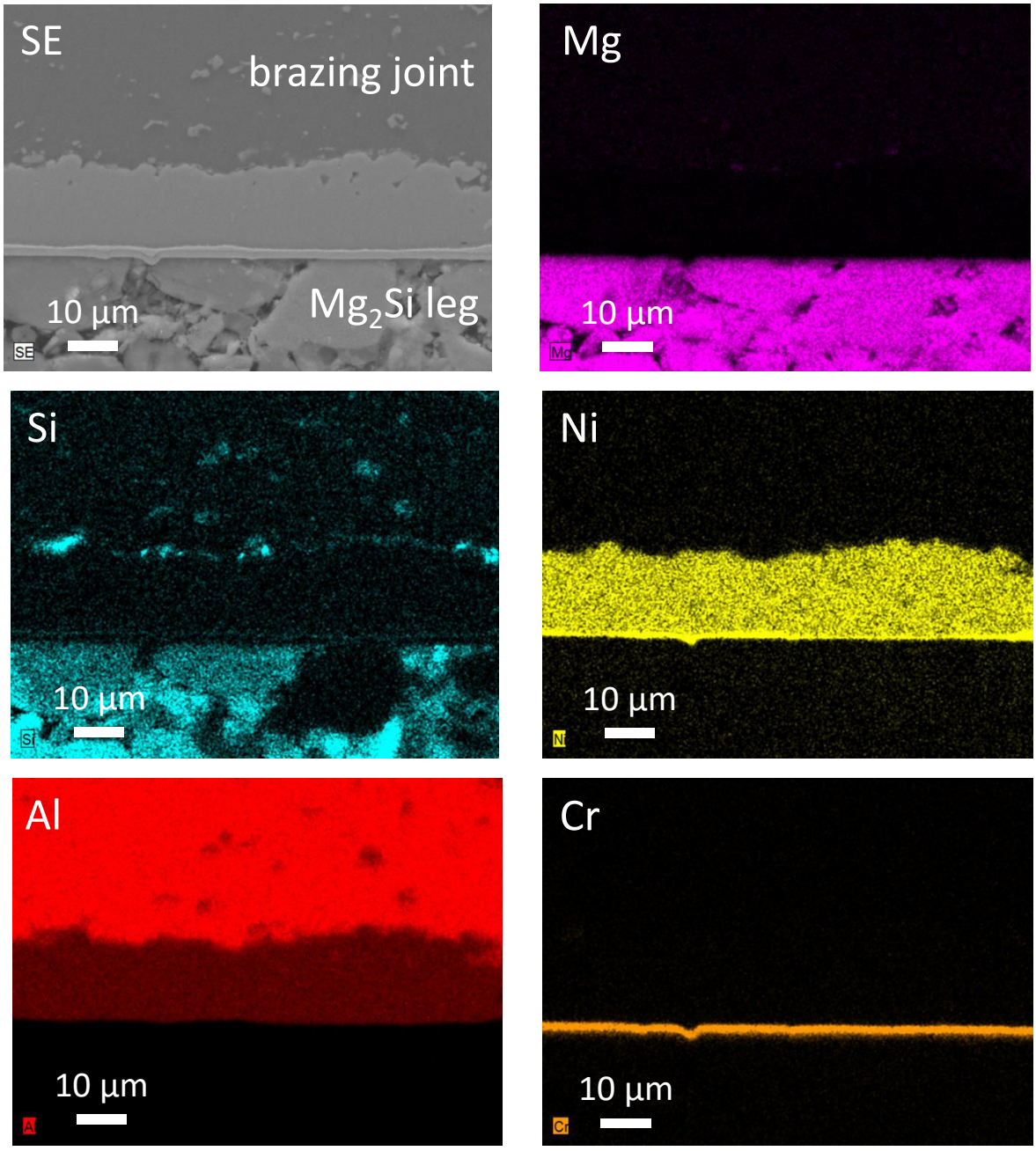

Figure 4.19. Compositional images by EDX mapping of the cross section of Mg_2Si-based TE legs coated with type 4 functional layers (Cr/Ni), after brazing.

The deposition process used for the growth of the Ta/Ni bi-layer, shown in Table 4.7, was reproduced to obtain the Cr/Ni bi-layer. Because of the similar sputtering rate between Ta and Cr, the same deposition time led to the growth of a 1 µm-thick Cr layer.

The deposition of the Cr/Ni bi-layer on the $Mg_2(Si,Ge)$ TE leg led generally to a very poor adherence to the TE leg, accounted by the complete delamination of the coating at various stages (after deposition, during brazing or after brazing). This delamination has been observed multiple times, with only a few cases when the bi-layer adhered to the TE leg. The brazing process which was performed on one of the latter instances led to results which are presented in Figure 4.19. As shown, the Cr/Ni bi-layer did not dissolve in the brazing joint and the Ni reacted with the joint and formed the Ni-Al alloy that is an indicator of the stability at the interface. Also, the clear-cut interface between the brazing joint and the underlying layers show the good diffusion barrier properties of the functional layers. However, despite these apparently advantageous properties of the Cr/Ni bi-layer obtained on a singular coating, the much more often delamination from the underlying TE leg eliminates Cr as a candidate for diffusion barriers.

Overall, the results obtained on the thin films deposited in this work are presented in Table 4.9 where they are rated qualitatively based on their adherence to the TE legs and potential as diffusion barriers. As it is shown, the most promising material that can be used as a diffusion barrier between $Mg_2(Si,Ge)$ TE legs and Al-Si alloy-based brazing joint is Ta in the formation of a Ta/Ni bi-layer.

Table 4.9. Qualitative rating of performance of all coatings in terms of adherence and diffusion barrier characteristics.

		Adherence	Diffusion barrier characteristics
Buffer layers	3 layers	--	-
	8 layers	-	+
	5-6 layers	-	-
	6 layers + Ti layer	-	-
Functional layers	Ti/Ni	-	+
	Ta/Ni	++	++
	W/Ni	+	+
	Cr/Ni	--	+

4.4 Conclusions

Eight different types of functional layers have been deposited on Bi-doped $Mg_2(Si,Ge)$ TE legs with the purpose of finding an efficient diffusion barrier between the TE legs and the joint used during their brazing to a metallic electrode. The deposition of all layers was followed by the coating with a Ni layer, which has proved to be efficient in the generation of a stable Ni-Al alloy after its reaction with the brazing joint when the interface does not lose cohesion. The functional layers have been classified into two categories. The first consists of a gradual reversal of Mg-Si and Ni content throughout multiple distinct layers (buffer layers) between the TE leg and Ni film. The basis of this endeavor lies on the expectation to improve the adherence of the Ni layer to the TE leg, as well as to acquire good chemical stability and low electrical resistance. The second category involves the deposition of a single layer between the two, based on various materials, with the same objective. The potential of the layers has been assessed after the brazing of the coated $Mg_2(Si,Ge)$ TE legs at Valeo by EDX mapping of the cross sections.

The deposition of the buffer layers was pursued in multiple instances, by varying their number between the TE leg and the Ni film, in order to obtain a finer transition in composition between the two. Also the thickness of the Ni layer was varied from 1.5 µm to 3 µm to test the impact it has on the diffusion barrier properties of the resulting coating. It was concluded that despite some promising results which indicated a diffusion barrier behavior, the consistent results revealing either the fracturing of the buffer layers or their dissolution in the brazing joint show that this first strategy does not lead to the attainment of the aforementioned goals. However, it was shown that a Ni layer with a thickness of at least 3 µm enhances the possibility of maintaining the cohesion of the deposited layers.

The deposition of functional layers based on a single metallic intermediate layer involved the use of Ti, Ta, W and Cr, which were chosen based on previous work concerned with finding diffusion barriers in the integrated circuit technology and thermoelectrics. Also the thickness of Ni was further increased to 4.5 µm. Out of the four materials, only one has presented very promising results, namely Ta. After brazing, this functional layer proved to hinder the diffusion between the TE leg and the brazing joint, as well as maintaining a good adherence. The diffusion barrier characteristics of Ta may be determined by the formation of a Ta-Si alloy inside the functional layer. Further investigation of the interface by TEM characterization is to be performed for testing this assumption. However, due to economic reasons, the costs involved in the diffusion barrier are to be minimized and Ta, although it proved to be efficient as a diffusion barrier, it is not the preferred candidate from this perspective. Therefore, further inquiries are necessary for finding other functional layers to be deposited on $Mg_2(Si,Ge)$ TE legs as diffusion barriers.

References

[1] M. Maaza, C. Sella, J. P. Ambroise, M. Kaabouchi, M. Miloche, F. Wehling, and M. Groos, Determination of diffusion coefficient D and activation energy Qa of nickel into titanium in Ni-Ti multilayers by grazing-angle neutron reflectometry, Journal of Applied Crystallography, 26 (1993) 334.

[2] Q. Xie, X.-P. Qu, J.-J. Tan, Y.-L. Jiang, M. Zhou, T. Chen, and G.-P. Ru, Superior thermal stability of Ta/TaN bi-layer structure for copper metallization, Applied Surface Science, 253 (2006) 1666.

[3] D. Bernoulli, U. Müller, M. Schwarzenberger, R. Hauert, and R. Spolenak, Magnetron sputter deposited tantalum and tantalum nitride thin films: An analysis of phase, hardness and composition, Thin Solid Films, 548 (2013) 157.

[4] W.-L. Wang, K.-T. Peng, H.-C. Kuo, M.-H. Yeh, H.-J. Chien, and T.-H. Ying, The contact resistance reduction of Cu interconnects by optimizing the crystal behavior of Ta/TaN diffusion barrier, Materials Science in Semiconductor Processing, 27 (2014) 860.

[5] H. P. Kattelus, E. Kolawa, K. Affolter, and M. A. Nicolet, Sputtered W–N diffusion barriers, Journal of Vacuum Science & Technology A, 3 (1985) 2246.

[6] P. Waters, Stress analysis and mechanical characterization of thin films for microelectronics and MEMS applications, Ph.D. (2008)

[7] T. Sakamoto, T. Iida, Y. Honda, M. Tada, T. Sekiguchi, K. Nishio, Y. Kogo, and Y. Takanashi, The Use of Transition-Metal Silicides to Reduce the Contact Resistance Between the Electrode and Sintered n-Type Mg_2Si, Journal of Electronic Materials, 41 (2012) 1805.

General conclusions

The objectives of the work presented herein, as discussed in Chapter 1, are connected to the development of miniaturized and bulk thermoelectric modules. The first objective entails the investigation of $Mg_2(Si,Sn)$ and Sb-doped Mg_2Si thin films in order to determine the feasibility of their integration in a thermoelectric device. Specifically, the chemical stability is a critical aspect in regards to the aimed working temperature of the device, as well as the reactivity of the thermoelectric material with the insulating or metal substrates and the overall thermo-mechanical behavior of the system. The second objective concerns the assessment of the potential of certain coatings to improve the electrical contacts between specific thermoelectric legs and electrodes used in an industrial thermoelectric module, namely to minimize the electrical resistance of the contact, to have a good adherence to the neighboring surfaces and to act as a diffusion barrier between the two.

In the section dedicated to the thermoelectric thin films, $Mg_2(Si,Sn)$ solid solutions have been deposited at different temperatures by microwave plasma-assisted co-sputtering on various substrates: SiO_2/Si, borosilicate glass, MgO and Ni. The resulting thin films presented either an antifluorite or, possibly, a hexagonal crystal structure. Subsequent thermal treatments showed that the films are sensitive to the composition. If the Si content lies between 0.40-0.43, the films go through a structural stabilization process or phase transition, leading to the separation into two cubic phases, suggesting that the as-deposited films are grown in a metastable phase. If however, the Si content is lower, proven in this case for a value of 0.38, the films do not go through any phase separation, marking probably one edge of the miscibility gap in the phase diagram, whose range is already highly disputed in the literature.

Extended heat treatments at an intermediate temperature (653 K) revealed the reactivity between the $Mg_2(Si,Sn)$ solid solutions and the Ni and SiO_2/Si substrates, which implies that their use in a miniaturized $Mg_2(Si,Sn)$-based TE device would necessitate an additional diffusion barrier. Conversely, borosilicate glass and MgO show both a high mechanical and chemical inertness up to the temperature where $Mg_2(Si,Sn)$ solid solutions show stability. Overall, the thermal stability of the presented thin films has been validated up to indicated temperature for a thermal treatment of 168 h. For the films which suffer phase separation, this temperature marks the highest value for which they maintain stability and do not start to decompose in phases of constituent elements.

The electrical properties of the films were also measured, showing values of the electrical conductivities similar to that of undoped bulk materials. The Seebeck coefficient of the films was determined at room temperature, showing a lower value than what was previously reported for bulk materials and suggestive of a p-type behavior instead of n-type.

However, due to the concerns regarding the noticed thermal instability of the $Mg_2(Si,Sn)$ thin films at moderately high temperatures, it was concluded they may not be suitable to be used in a thin film-based thermoelectric device. Therefore, an alternative was chosen investigating the properties of Sb-doped Mg_2Si thin films. Their deposition was performed both at room temperature and 463 K. It was determined by XRD measurements that the deposition temperature leads to different structural properties. The films deposited at room temperature showed a high degree of texture along the [220] direction, while those deposited at 463 K are grown with more disoriented crystallites. As a result, during the characterization of the transport properties, it was determined that the films deposited at 463 K have slightly higher electrical conductivities than the films deposited at room temperature, suggesting that the degree of texture inside the film can have an effect on the electrical properties.

The electrical conductivities of Sb-doped Mg_2Si thin film obtained in this work are lower than those obtained on bulk materials, possibly due to the decrease of the grain size, which ultimately leads to an increase carrier scattering at grain boundaries. However, this also leads to the decrease of thermal conductivity (measured cross-plane) to a value more than half than what is usually reported for bulk materials. As for the Seebeck coefficient, it was proved to be similar or even higher than previous results on bulk Sb-doped Mg_2Si compounds.

In the second part of the work, eight different types of functional layers have been deposited on Bi-doped $Mg_2(Si,Ge)$ TE legs with the purpose of finding an efficient diffusion barrier between the TE legs and the joint used during their brazing to a metallic electrode. The deposition of all layers was followed by the coating with a Ni layer, which has proved to be efficient in the generation of a stable Ni-Al alloy after its reaction with the brazing joint when the interface does not lose cohesion. The functional layers have been classified into two categories. The first consists of a gradual reversal of Mg-Si and Ni content throughout multiple distinct layers (buffer layers) between the TE leg and Ni film. The second endeavor involves the deposition of a single layer between the two, based on various materials (Ti, Ta, W and Cr), with the same objective. The potential of the layers has been assessed after the brazing of the coated $Mg_2(Si,Ge)$ TE legs at Valeo by EDX mapping of the cross sections. Eventually, only the second path proved to be encouraging, with the finding of Ta as a good diffusion barrier. Its effectiveness may be put on account of the formation of a Ta-Si alloy at the interface, which lead to the necessary properties of the functional layer.

Perspectives

Although it was noticed that the $Mg_2(Si,Sn)$ thin films suffer decomposition and thermal instability at relatively high temperatures, this was confirmed only for compositions with a Si content higher than 0.4, which originally showed chemical instability the phase separation into two phases. With lower Si content, it was noticed that the resulting solid solution does not face this chemical instability and therefore, it is necessary to evaluate its thermal stability as well at higher temperatures than 653 K. Moreover, the p-type behavior of the thin films, compared to the usual n-type characteristics of $Mg_2(Si,Sn)$ reported in the literature, requires additional explanations which may be extracted from a better understanding of the carrier transport due to microstructure or the presence of vacancies in the lattice that can act as acceptor levels in the band structure of the material. As for the Sb-doped Mg_2Si thin films, their thermal stability is to be evaluated, in order to assess the use of the thin films at working temperatures (up to 850 K). Additionally, in-plane measurements of the thermal conductivity are needed in order to determine the extent at which the transport properties of the charge carriers are changed by the degree of texture with respect to the plane of measurement.

Concerning the diffusion barriers, further investigations are needed to explain the reason why the Ta/Ni bi-layer showed auspicious characteristics as a functional layer for the Bi-doped $Mg_2(Si,Ge)$ thermoelectric material, including TEM characterization of the interface to test the assumption of Ta-Si alloy formation. Furthermore, the electrical resistance of the contacts after brazing to the electrode will be measured and then the reproducibility of the beneficial results given by Ta will be tested at a larger scale by the deposition on multiple thermoelectric legs. Nevertheless, due to economic reasons, the costs involved in the diffusion barrier need to be reduced and Ta, although it proved to be efficient as a diffusion barrier, it is not the preferred candidate from this perspective. Therefore, further materials are to be investigated in the search for alternatives.

Appendix. Sputtering yield calculations using the models of Yakamura and Eckstein

The two models proposed by Yamamura [1] and Eckstein [2] for determining the sputtering yield Y as a function of incident ion energy are based on semi-empirical formulas which are given for normal incidence and for any ion-target pair.

- Yamamura offered the following formula for the sputtering yield (with each parameter explained afterwards):

$$Y = 0.042 \frac{Q \cdot \alpha^*}{U_s} \frac{s_n(E)}{1 + \Gamma k_e \varepsilon^{0.3}} \left[1 - \sqrt{\frac{E_{th}}{E_i}}\right]^s \qquad (A.1)$$

- Q is a coefficient describing the target that is calculated with:

$$Q = r^{-3}\left[0.0202 \cdot \left\{exp\left[-\frac{(M_T - 19)^2}{2 \cdot 14.6^2}\right]\right\} + 0.0166\left\{1 - exp\left[-\frac{(M_T - 5)^2}{50^2}\right]\right\}\right] \qquad (A.2)$$

- r is the average interatomic spacing determined by:

$$r = \frac{10^{24} \cdot M_T}{\rho \cdot N_A}(nm^3) \qquad (A.3)$$

- M_T and ρ are the atomic mass and density of the target
- N_A is Avogadro's number
- U_s is the surface binding energy of the target expressed in eV
- E_i is the ion energy
- α^* is a coefficient determined by:

$$\alpha^* = 0.249\left(\frac{M_T}{M_i}\right)^{0.56} + 0.0035\left(\frac{M_T}{M_i}\right)^{1.5} \quad \text{if } M_i < M_T \qquad (A.4.a)$$

$$\alpha^* = 0.0875\left(\frac{M_T}{M_i}\right)^{-0.15} + 0.165\left(\frac{M_2}{M_i}\right)^{1.5} \quad \text{if } M_i > M_T \qquad (A.4.b)$$

- M_i is the atomic number of the ion
- $S_n(E)$ is the nuclear stopping cross-section determined by:

$$S_n(E) = \frac{84.78 \cdot Z_i Z_T}{\sqrt{Z_i^{2/3} + Z_T^{2/3}}} \cdot \frac{M_i}{M_i + M_T} \cdot s_n^{TF}(\varepsilon) \qquad (A.5)$$

- Z_i and Z_T are the atomic number of the ion and target, respectively
- s_n^{TF} is the nuclear stopping power determined by:

$$s_{n(\varepsilon)}^{TF} = \frac{3.441\sqrt{\varepsilon}\cdot \ln(\varepsilon + 2.718)}{1 + 6.355\cdot\sqrt{\varepsilon} + \varepsilon\left(6.882\sqrt{\varepsilon} - 1.708\right)} \quad (A.6)$$

- ε is the reduced energy, equal to:

$$\varepsilon = E_i \cdot \frac{M_T}{M_i + M_T} \cdot \frac{\alpha_L}{Z_i Z_T \cdot e^2} \quad (A.7)$$

- e is the elementary charge
- α_L is the Lindhard screening length:

$$\alpha_L = 0.4685\left(Z_i^{2/3} + Z_T^{2/3}\right)^{-0.5}\ \text{Å} \quad (A.8)$$

- Γ is a coefficient calculated with:

$$\Gamma = \frac{W(\mathrm{T})}{1 + \left(\frac{M_i}{7}\right)^3} \quad (A.9)$$

- W(T) is another coefficient which describes the target and extracted from empirical data tables (as well as the coefficient s)
- k_e is the electronic stopping coefficient:

$$k_e = 0.079 \cdot \frac{(M_i + M_T)^{3/2}}{M_i^{3/2}\cdot M_T^{1/2}} \cdot \frac{Z_i^{2/3}\cdot Z_T^{1/2}}{\left(Z_i^{2/3} + Z_T^{2/3}\right)^{3/4}} \quad (A.10)$$

- E_{th} is the threshold energy expressed in eV and given by:

$$E_{th} = \frac{6.7}{\gamma}\cdot U_s \qquad \text{if } M_i > M_T \quad (A.11.a)$$

$$E_{th} = \frac{1 + 5.7}{\gamma}\cdot\frac{M_i}{M_T}\cdot U_s \qquad \text{if } M_i < M_T \quad (A.11.b)$$

- Γ is the energy transfer factor:

$$\gamma = \frac{4M_iM_T}{(M_i + M_T)^2} \quad (A.12)$$

➢ The formula expressed by Eckstein for determining the sputtering yield is:

$$Y = qS_n^{Krc}(\varepsilon)\cdot\frac{(E_i\ /\ E_{th} - 1)^{\mu}}{\lambda + (E_i\ /\ E_{th} - 1)^{\mu}} \quad (A.13)$$

- S_n^{KrC} is the nuclear stopping power with the new expression:

$$s_n^{KrC} = \frac{0.5 \cdot ln(1 + 1.2288 \cdot \varepsilon)}{\varepsilon + 0.1728 \cdot \sqrt{\varepsilon} + 0.008 \cdot \varepsilon^{0.1504}} \quad \text{(A.14)}$$

- ε is the reduced energy, with another new expression:

$$= E_i \cdot \frac{M_T}{M_i + M_T} \cdot \frac{0.03255}{Z_i Z_T \cdot \left[Z_i^{2/3} + Z_T^{2/3}\right]^{1/2}} \quad \text{(A.15)}$$

- q, λ and μ are miscellaneous parameters which are found in empirical data tables

References

[1] Y. Yamamura and H. Tawara, Energy dependence of ion-induced sputtering yields from monoatomic solid at normal incidence, Atomic Data and Nuclear Data Tables, 62 (1996) 149.

[2] W. Eckstein and R. Preuss, New fit formulae for the sputtering yield, Journal of Nuclear Materials, 320 (2003) 209.

Résumé en français

Cette thèse concerne le dépôt de couches minces par la méthode de co-pulvérisation assistée par plasma micro-onde dans le contexte de leurs applications potentielles pour la thermoélectricité. Deux volets principaux ont été développés au cours de ce travail: la synthèse et l'étude des propriétés de couches minces à base de Mg_2Si et $Mg_2(Si,Sn)$ pour une mise en œuvre au sein de modules thermoélectriques miniaturisés, et l'étude de matériaux susceptibles d'agir comme barrières de diffusion entre un thermoélément à base de Mg_2Si et les joints de brasage utilisés pour connecter les contacts électriques. Dans la première partie de l'ouvrage, des couches minces de solutions solides de $Mg_2(Si,Sn)$, avec une stœchiométrie proche de $Mg_2S_{i0.4}Sn_{0.6}$, ont été déposées sur différents substrats. Les propriétés thermomécaniques de ces couches ont été étudiées en fonction du processus de dépôt et de la nature du substrat, tandis que la stabilité thermique et la réactivité avec les substrats ont été examinées, ont fonction de la composition, dans le domaine de températures intermédiaires. En outre, les propriétés de transport des couches minces de Mg_2Si dopé au Sb ont été caractérisées, en s'intéressant, en particulier, à l'effet de la texturation de la couche mince sur les propriétés thermoélectriques (coefficient Seebeck, conductivité électrique et thermique). La deuxième partie de cette thèse est dédiée au dépôt de couches barrières sur des échantillons massifs de $Mg_2(Si,Ge)$ dopés Bi afin de limiter la diffusion et la réactivité entre le thermoélément et le joint de brasage à base d'alliage Al-Si dans le but d'obtenir un contact électrique chimiquement stable et de faible résistance. Deux options ont été étudiées : l'une est basée sur des couches à gradient destinées à ajuster progressivement la composition entre celle du thermoélément et une couche supérieure de Ni qui constitue la barrière de diffusion. L'autre option concerne les bi-couches M/Ni, où M est un métal (Ti, Ta, W ou Cr). Globalement, le travail présenté ici offre un aperçu du potentiel des couches minces à base de Mg_2Si et $Mg_2(Si,Sn)$ dans la réalisation d'un module thermoélectrique miniaturisé et l'étude de faisabilité de différents matériaux comme barrières de diffusion dans des modules conventionnels.